Crystal Structures and Optical Properties of Group 14 Chalcogenides

by

Luke T. Menezes

A thesis

presented to the University of Waterloo

in fulfillment of the

thesis requirement for the degree of

Master of Science

in

Chemistry

Waterloo, Ontario, Canada, 2019

Author's declaration

I hereby declare that I am the sole author of this thesis. This is a true copy of the thesis,

including any required final versions, as accepted by my final examiners.

I understand that my thesis may be made electronically available to the public.

Abstract

The crystal structures and physical properties of several new tetrel and chalcogenide compounds have been investigated in this thesis. The crystal structures, syntheses, and electronic structures of the three centrosymmetric compounds $Ba_7Ge_2Se_{17}$ (*Pnma*, a = 12.6518(1) Å, b = 20.0692(2) Å, c =12.3067(9) Å), $Ba_6Ge_2Se_{12}$ (*P2₁/c*, a = 10.0903(2) Å, b = 9.3640(2) Å, c = 25.7643(5) Å, and β = 90.303(1) °), and $Ba_8Sn_4Se_{17}$ (*C2/c*, a = 47.2887(2) Å, b = 12.6224(5) Å, c = 25.7173(1) Å, and β = 104.729(1) º) have been reported. The experimentally determined band gaps of these semiconductors are 1.51 eV, 1.75 eV, and 1.92 eV.

The non-centrosymmetric compounds (NCS) γ-Sr_2GeSe_4 and α-Pb_2GeSe_4 have already been reported, but the new substitution variants $Sr_{1.31}Pb_{0.69}GeSe_4$ (*Ama2*, a = 10.31220(1) Å, b = 10.39320(1) Å, c = 7.42140(1) Å) and $Sr_{0.21}Pb_{1.79}GeSe_4$ (*I$\bar{4}$3d*, a = 14.6177(3) Å) have been introduced here for the first time. The experimental band gaps of γ-Sr_2GeSe_4, $Sr_{1.3}Pb_{0.7}GeSe_4$, $Sr_{0.25}Pb_{1.75}GeSe_4$, and α-Pb_2GeSe_4 are 2.00 eV, 1.65 eV, 1.45 eV and 1.42 eV. The nonlinear optical (NLO) properties of the orthorhombic compounds γ-Sr_2GeSe_4, and $Sr_{1.3}Pb_{0.7}GeSe_4$ (approximated as the supercell "$Sr_{1.5}Pb_{0.5}GeSe_4$"), were studied both theoretically using first-principle calculations and experimentally. The theoretical calculation found the effective NLO susceptability, d_{eff}, of γ-Sr_2GeSe_4 and "$Sr_{1.5}Pb_{0.5}GeSe_4$" to be 10.8 pm V^{-1} and 8.8 pm V^{-1} respectively at the static limit. The experimental d_{eff}'s of γ-Sr_2GeSe_4, $Sr_{1.3}Pb_{0.7}GeSe_4$, $Sr_{0.25}Pb_{1.75}GeSe_4$, and α-Pb_2GeSe_4 are 2.6 pm V^{-1}, 2.3 pm V^{-1}, 0.68 pm V^{-1}, and 0.79 pm V^{-1}.

The final non-centrosymmetric compound discussed in this thesis is $BaCuSiTe_3$ (*Pc*, a = 7.5824(1) Å, b = 8.8440(1) Å, c = 13.1289(2) Å, and β = 122.022(1) °,) which contains $[Si_2Te_6]^{6-}$ polyhedra. The theoretical d_{eff} of $BaCuSiTe_3$ was calculated to be 3.4 pm V^{-1} at the static limit and experimentally found to be 0.52 pm V^{-1}.

Acknowledgements

I would like to thank Professor Holger Kleinke for patience and guidance over the course of this Master's thesis. I would also like to thank all the other members of the committee, Professor Linda Nazar and Assistant Professor Rodney Smith for their time and guidance over the past two years.

I would also like to thank Dr. Weiguo Zhang and Professor Shiv Halasyamani at the University of Houston for their assistance in performing the experimental SHG measurements.

Finally, I would also like to extend thanks to Dr. Abdeljalil Assoud and the Kleinke group members Dr. Abdeljalil Assoud, Dr. Leilane Macario, Parisa Jafarzadeh, Yixuan Shi, Cheryl Sturm, Daniel Ramirez, Darren Herweyer, Natalie Boccalon, and Yanran Zheng.

Table of Contents

List of Figures

List of Tables

List of Abbreviations

NLO: Nonlinear optic

SHG: Second harmonic generation

SFG: Sum frequency generation

DFG: Difference frequency generation

NCS: Non-centrosymmetric

AGS: $AgGaS_2$

AGSe: $AgGaSe_2$

MP: Melting point

BP: Boiling point

XRD: X-ray diffraction

PMT: Photomultiplier Tube

UV: Ultraviolet

IR: Infrared

ESU: Electrostatic unit

SI: International system of units

SOS: Sum-over-states

DFT: Density functional theory

PBE-GGA: Perdew, Burke, Ernzerhof – generalized gradient approximation

mBJ: Modified Becke Johnson

DOS: Density of states

PM: Phase-matching

NPM; Non-phase-matching

1 Introduction

The demand for intense light at various frequencies exceeds the number of light sources on the market. One approach to solve this problem has been to use media that can modulate the frequencies of light to get through either up-conversion or down-conversion to create shorter or longer wavelengths respectively to get better coverage of the electromagnetic spectrum. Nonlinear optics (NLO) is the study of a branch of physics which studies these phenomena. One example of nonlinear optics is the second harmonic generation (SHG) or frequency doubling of a Nd:YAG laser from 1064 nm to 532 nm through an NLO material such as a $LiNbO_3$ crystal.[1] This is an example of SHG, but higher-order frequency generation is possible such as third-harmonic generation. NLO crystals have found uses in remote sensing,[2] environmental monitoring,[3] communication systems,[4] tissue imaging,[5] and minimally invasive surgeries.[6,7]

1.1 Linear Optics

A physical description of linear optics is given by.[8]

$$P(t) = \varepsilon_0 \chi^{(1)} E(t) \tag{1.1.1}$$

where $P(t)$ is the dipole moment per unit volume or polarization, ε_0 is the permittivity of free space, $\chi^{(1)}$ is a proportionality constant known as the linear susceptibility, and $E(t)$ is the optical field strength. Linear optics is the subdiscipline which is used to describe lenses, mirrors, and diffraction gratings. In terms of material science, linear optics is also responsible for the refractive index of a material. The refractive index of a medium, n, is the ratio of the speed of light in a vacuum, c, and the speed of light travelling through the medium, v.

$$\mathrm{n} = \frac{c}{v} \tag{1.1.2}$$

Due to crystallographic symmetry, the speed of light through the media may not be equal in all crystallographic directions. Therefore, the material will have the same number of refractive indices as unique axes. The refractive indices may be determined from the diagonalized dielectric tensor of material since the refractive indices, n_{xx}, n_{yy}, and n_{zz} are related to the dielectric constants, ε_{xx}, ε_{yy}, and ε_{zz} via equation (1.1.3) where x, y, and z correspond to their respective crystallographic axes.[9] Birefringence, Δn, is defined as the difference between refractive indices between the crystallographic axes.

$$\sqrt{\varepsilon_{ii}} = n_{ii} \qquad (1.1.3)$$

Table 1. Relationship between the number of unique crystallographic axes and the corresponding dielectric tensor. Isotropic materials include those without long-range ordering such as gases, liquids, and amorphous solids.

Birefringence	Crystal Class	Dielectric Tensor
Biaxial Birefringence	Triclinic, Monoclinic, Orthorhombic	$\begin{bmatrix} \varepsilon_{xx} & 0 & 0 \\ 0 & \varepsilon_{yy} & 0 \\ 0 & 0 & \varepsilon_{zz} \end{bmatrix}$
Uniaxial Birefringence	Tetragonal, Trigonal, Hexagonal	$\begin{bmatrix} \varepsilon_{xx} & 0 & 0 \\ 0 & \varepsilon_{xx} & 0 \\ 0 & 0 & \varepsilon_{zz} \end{bmatrix}$
No Birefringence	Cubic, Isotropic	$\begin{bmatrix} \varepsilon_{xx} & 0 & 0 \\ 0 & \varepsilon_{xx} & 0 \\ 0 & 0 & \varepsilon_{xx} \end{bmatrix}$

1.2   Nonlinear Optics

Correction terms may be added to equation (1.1.1) to create an infinite Taylor series.

$$P(t) = P^{(1)}(t) + P^{(2)}(t) + P^{(3)}(t) \dots \qquad (1.2.1)$$

$$P(t) = \varepsilon_0 \big[\chi^{(1)} E(t) + \chi^{(2)} E^2(t) + \chi^{(3)} E^3(t) \dots \big] \qquad (1.2.2)$$

The second and third terms are associated with second and third harmonics, respectively. Several phenomena are associated with the second-order nonlinear optical susceptibility such as second harmonic generation (SHG), sum frequency generation (SFG), and difference frequency generation (DFG). Figure 1 is a visualization of the physical phenomena governed by the second-order nonlinear optical susceptibility term. SHG occurs when two photons of equal frequency are destroyed and a photon equal to two times the frequency of the original photons is emitted. Third harmonic generation is the analogous process where three photons are destroyed and a photon equal to three times the original frequency is emitted. SFG involves two photons of different frequencies being destroyed and producing a single photon that has the total energy of the starting two photons. DFG involves breaking up a high energy photon into two lower-energy photons.
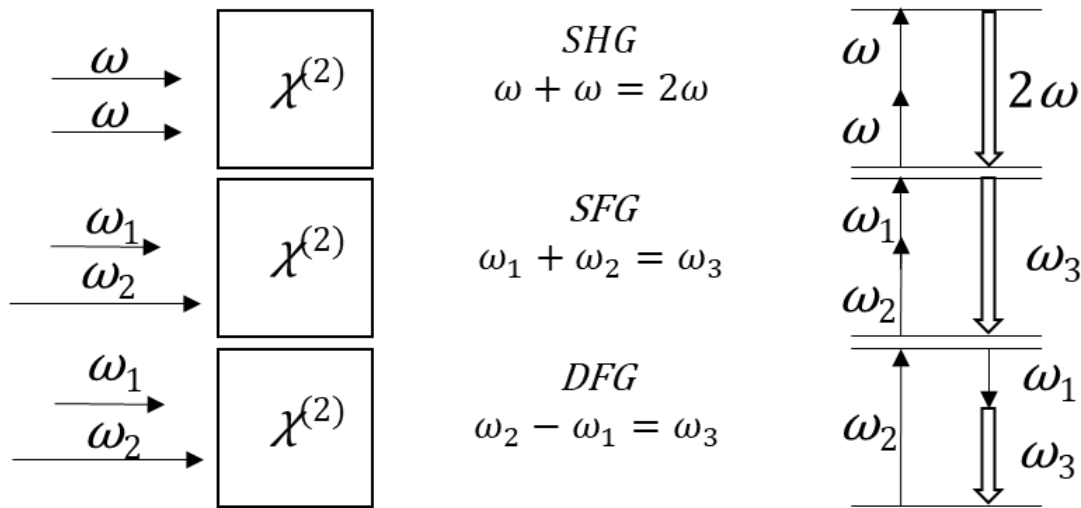
Figure 1. Geometric representations and energy level diagrams of SHG (top), SFG (middle), and DFG (bottom).

A prerequisite for SHG is for the material to belong to one of the 21 non-centrosymmetric (NCS) crystal classes. NCS crystal classes do not have an inversion center and

therefore the dipole moments of the atoms may not cancel each other leading to polar crystal classes. Note that all polar crystal classes are NCS but not all NCS crystal classes are polar. Using a molecular example with tetrahedral symmetry such as CH_4, this becomes obvious. The consequence of having inversion symmetry is that the even powered terms in the polarization power series vanish completely since the positive and negative polarizations with respect to time sum to zero.

$$P^{(2)}(t) = \chi^{(2)}E^2(t) \tag{1.2.3}$$

Changing the sign of the applied electric field must also change the sign of the polarization in a centrosymmetric medium.

$$-P^{(2)}(t) = \chi^{(2)}[-E(t)]^2 \tag{1.2.4}$$

$$-P^{(2)}(t) = \chi^{(2)}E^2(t) \tag{1.2.5}$$

$$\therefore \chi^{(2)} = 0 \tag{1.2.6}$$

Therefore, $P^{(2)}(t) = -P^{(2)}(t)$ which can only be the case if $\chi^{(2)}$ is zero. Since the second-order linear susceptibility vanishes to zero, NLO phenomena such as SHG are not possible within materials with centrosymmetric crystal classes.

An intuitive explanation of nonlinear susceptibility comes from considering the motion of an electron. Using the Lorentz model of an atom, the electron may be thought of as a particle within a parabola with increasing potential as it moves away from the center. An applied electric field will force the electron one direction and a restoring force resists the electric field. In the Lorentz model as well as in centrosymmetric media, the restoring force is symmetric in either direction. The actual potential of an atom does not perfectly display a linear response of polarizability with respect to the electric field due to the ionization potential of the electron. In

NCS mediums, the restoring force is never symmetric is all directions. This leads to a nonlinear response in polarization and the waveform does not sum to zero over time.

Table 2. The 32 crystallographic point groups. Centrosymmetric are written in blue, point groups with only rotation axes are said to be enantiomorphic and are labelled in red, polar point groups are listed in **bold**. All the point groups which are not written in blue are capable of SHG.

Crystal System	32 Crystallographic Point Groups						
Triclinic	1	$\bar{1}$					
Monoclinic	**2**	***m***	2/*m*				
Orthorhombic	222	***mm*2**	*mmm*				
Tetragonal	**4**	$\bar{4}$	4/*m*	422	**4*mm***	$\bar{4}2m$	4/*mmm*
Trigonal	**3**	$\bar{3}$	32	**3*m***	$\bar{3}m$		
Hexagonal	**6**	$\bar{6}$	6/*m*	622	**6*mm***	$\bar{6}2m$	6/*mmm*
Cubic	23	$m\bar{3}$	432	$\bar{4}3m$	$m\bar{3}m$		

Although the lack of inversion symmetry is crucial for SHG the specific NCS point group adds additional restrictions upon the second-order nonlinear optical susceptibility coefficient. Therefore, it is no longer enough to describe $\chi^{(2)}$ as a scalar value. $\chi^{(2)}$ can now be written rather as a third-order tensor to encapsulate the symmetries of the crystal system along its three crystallographic axes x, y, and z which are denoted as 1, 2, and 3 respectively as the subscripts for $\chi^{(2)}$.

$$\begin{bmatrix} P_x^{\omega 1+\omega 2} \\ P_y^{\omega 1+\omega 2} \\ P_z^{\omega 1+\omega 2} \end{bmatrix} = \varepsilon_0 \begin{bmatrix} \chi_{111}^{(2)} & \chi_{122}^{(2)} & \chi_{133}^{(2)} & \chi_{123}^{(2)} & \chi_{113}^{(2)} & \chi_{112}^{(2)} \\ \chi_{211}^{(2)} & \chi_{222}^{(2)} & \chi_{233}^{(2)} & \chi_{223}^{(2)} & \chi_{213}^{(2)} & \chi_{212}^{(2)} \\ \chi_{311}^{(2)} & \chi_{322}^{(2)} & \chi_{333}^{(2)} & \chi_{323}^{(2)} & \chi_{313}^{(2)} & \chi_{312}^{(2)} \end{bmatrix} \begin{bmatrix} E_x^{\omega 1} E_x^{\omega 2} \\ E_y^{\omega 1} E_y^{\omega 2} \\ E_z^{\omega 1} E_z^{\omega 2} \\ E_y^{\omega 1} E_z^{\omega 2} + E_y^{\omega 2} E_z^{\omega 1} \\ E_z^{\omega 1} E_x^{\omega 2} + E_z^{\omega 2} E_x^{\omega 1} \\ E_x^{\omega 1} E_y^{\omega 2} + E_x^{\omega 2} E_y^{\omega 1} \end{bmatrix} \quad (1.2.7)$$

In equation (1.2.7), P and E are now written in terms of their crystallographic directions x, y, and z as well as with respect to the individual contributions of the applied optical field with a frequency equal to ω_1 and the frequency of the generated optical field ω_2.

To simplify the equation (1.2.7) a contracted notation is used to denote the 18 tensor elements. The last two digits are replaced to denote the tensor element's position in the matrix. 11, 22, 33, 23, 13, and 12, are replaced by 1, 2, 3, 4, 5, and 6 respectively. By convention a new variable, d, is introduced to represent second-order nonlinear optical susceptibility where:

$$2d_{ijk} = \chi_{ijk}^{(2)} \tag{1.2.8}$$

Factoring out the 2 from the definition of d gives the new expression for second-order polarizability with the contracted notation:

$$
\begin{bmatrix} P_x^{\omega1+\omega2} \\ P_y^{\omega1+\omega2} \\ P_z^{\omega1+\omega2} \end{bmatrix} = 2\varepsilon_0 \begin{bmatrix} d_{11} & d_{12} & d_{13} & d_{14} & d_{15} & d_{16} \\ d_{21} & d_{22} & d_{23} & d_{24} & d_{25} & d_{26} \\ d_{31} & d_{32} & d_{33} & d_{34} & d_{35} & d_{36} \end{bmatrix} \begin{bmatrix} E_x^{\omega1} E_x^{\omega2} \\ E_y^{\omega1} E_y^{\omega2} \\ E_z^{\omega1} E_z^{\omega2} \\ E_y^{\omega1} E_z^{\omega2} + E_y^{\omega2} E_z^{\omega1} \\ E_z^{\omega1} E_x^{\omega2} + E_z^{\omega2} E_x^{\omega1} \\ E_x^{\omega1} E_y^{\omega2} + E_x^{\omega2} E_y^{\omega1} \end{bmatrix} \tag{1.2.9}
$$

The expression for the second-order nonlinear optical susceptibility tensor in equation (1.2.9) may be simplified by means of Kleinman symmetry which states that nonlinear optical susceptibility tensor elements are independent of frequency.[10] This assumption is true at low frequencies since the frequencies participating in SHG are much smaller than the resonant frequency of the material. In practical terms, this means that crystallographic directions of the tensor elements commute and can, therefore, be permutated freely. Through these permutations of crystallographic directions, several tensor elements become equivalent under Kleinman symmetry. For example:

$$d_{12} \equiv d_{122} = d_{212} \equiv d_{26} \qquad (1.2.10)$$

As a result of these, the degeneracies under Kleinman symmetry the d-tensor reduces from 18

unique elements to 10 unique elements.

$$\begin{bmatrix} d_{11} & d_{12} & d_{13} & d_{14} & d_{31} & d_{21} \\ d_{21} & d_{22} & d_{23} & d_{32} & d_{14} & d_{12} \\ d_{31} & d_{32} & d_{33} & d_{23} & d_{13} & d_{14} \end{bmatrix} \qquad (1.2.11)$$

Equation (1.2.11) represents the d–tensor for the triclinic 1 point group under Kleinman

symmetry. For higher symmetry NCS point groups there can be fewer than 10 unique elements.

When there are more operations several tensor elements vanish completely. Research into NLO

materials is based around discovering compounds with high d_{ij} values. High d_{ij} values

correspond to efficient SHG and in practice, a high-quality crystal would be oriented along the

crystallographic with the largest d_{ij} value.

1.3   The Effective NLO Susceptibility Element, d_{eff}

For exploratory research into NLO materials, it is not necessary to grow high-quality single

crystals of the compound. The SHG signal can be measured on NCS powdered samples and a

signal corresponding to a combination of all non-zero d_{ij}, known as d_{eff}.[11]

$$\langle (d_{eff})^2 \rangle = \frac{19}{105} \sum_i (d_{iii})^2 + \frac{13}{105} \sum_{i \neq j} d_{iii} d_{ijj} + \frac{44}{105} \sum_{i \neq j} (d_{iij})^2$$
$$+ \frac{13}{105} \sum_{ijk,cyclic} d_{iij} d_{jkk} + \frac{5}{7} (d_{ijk})^2 \qquad (1.3.1)$$

The SHG intensity of the sample is compared to the SHG intensity of a standard with known d_{ij}

values such as AgGaS$_2$ (AGS), or AgGaSe$_2$ (AGSe).

1.4   Phase-matching Conditions

To have efficient SHG energy and momentum must be conserved, this is known as phase-matching. The intensity of the SHG signal drops rapidly when phase-matching conditions are not met. Conservation of energy is described in terms of the frequencies of the source (ω_1) and generated photons (ω_2).

$$\omega_1 + \omega_1 = \omega_2 \tag{1.4.1}$$

Conservation of momentum is described by the wavevectors of the source and generated photons, k_1, and k_2 respectively.

$$k_1 + k_1 = k_2 \tag{1.4.2}$$

$$k = \frac{\omega}{v} \tag{1.4.3}$$

Substituting equations (1.1.2) and (1.4.3) into (1.4.2) the relationship between refractive index and conservation of momentum becomes clear.

$$\frac{\omega_1 n_1}{c} + \frac{\omega_1 n_1}{c} = \frac{\omega_2 n_2}{c} \tag{1.4.4}$$

For phase-matching conditions to be perfectly met the refractive index of the medium at ω_1 must be the same as the refractive index at ω_2. This condition is not possible to meet without birefringence due to the frequency dependence of the refractive index. Refractive index increases with increasing frequency. In a material which displays birefringence, it is possible to cross over to a different refractive index curve to keep the refractive index the same at the new frequency thus conserving momentum. In practice to achieve phase-matching using the inherent birefringence of the crystal the source light is polarized along the crystallographic direction corresponding to the lower refractive index, n_1. If these two source photons must be polarized parallel to each other this is known as "type I" phase-matching and if the source photons must be

orthogonal to each other than this is known as "type II" phase-matching. The lack of

birefringence ends up limiting SHG intensity of many cubic materials with large nonlinear

susceptibility values such as GaAs which adopts the zincblende structure with the point group

$\bar{4}3m$.[12] The intensity of SHG as it relates to conservation of momentum is described by

equations (1.4.4) and (1.4.5).

$$\Delta k = k_2 - 2k_1 \tag{1.4.4}$$

$$I = I_{max}\left[\frac{\sin\left(\frac{\Delta kL}{2}\right)}{\frac{\Delta kL}{2}}\right]^2 \tag{1.4.5}$$

Where I, is the intensity of SHG and L is the pathlength for the laser through the crystal. For

maximum SHG intensity to be achieved Δk must be zero otherwise intensity drops dramatically.

To determine whether a crystal will be capable of phase-matching it is useful to

determine its birefringence at the desired wavelength. Kurtz and Perry at Bell Labs found that a

compound's phase-matching ability could be tested on powdered samples.[11] It is assumed that

the particles are oriented randomly in powder and that the SHG intensity adds cumulatively as it

passes through more particles. The laser passes through L/r particles in the powdered sample

where L is the path length through the powdered sample and r is the average size of a particle in

the powdered sample. In type I phase-matching there is not an angular dependence between the

particles so the SHG intensity for smaller particles is weak due to the increased amount of

scattering from the greater number of particles. Eventually, the SHG intensity plateaus once the

particles are large enough. When the compound does not type I phase to match the SHG intensity

reaches a maximum before decreasing with increasing particle size. This is because there is a

small range of angles which the incident light must hit the particle for SHG to occur. For larger

particle sizes the incident beam passes through a fewer number of particles meaning there will be fewer in the correct orientation to perform SHG.

An experimental d_{eff} may be calculated by comparing the SHG intensity of a new sample with the SHG intensity of a standard.[13] If the new sample exhibits phase-matching it must be compared using a phase-matching (PM) standard like $LiNbO_3$. Alternatively, if the new sample does not phase match a non-phase-matching (NPM) standard like α-SiO_2. Equations (1.4.6) and (1.4.7) give d_{eff} in SI units (pm V^{-1}). Due to the particle size dependence of SHG intensity, it is crucial to compare standards and samples that have been sieved to the same particle size ranges.

$$\langle d_{eff} \rangle_{PM} = \left[\frac{I^{2\omega}(A)}{I^{2\omega}(LiNbO_3)} \times 798 \right]^{1/2} \tag{1.4.6}$$

$$\langle d_{eff} \rangle_{NPM} = \left[\frac{I^{2\omega}(A)}{I^{2\omega}(\alpha - SiO_2)} \times 0.3048 \right]^{1/2} \tag{1.4.7}$$

1.5 Calculating Optical Properties from First Principles.

When NLO compounds are being explored optical properties are calculated from density functional theory (DFT) since growing high-quality large crystals is time-consuming and not worth the effort if the NLO properties are predicted to be poor. The second-order susceptibilities may be calculated following the convergence of the self-consistent cycle criteria. Second-order susceptibilities may be calculated by several different DFT software such as Abinit,[14] Elk,[15] VASP,[16] and CASTEP.[17,18] The two commonly used approaches for calculating nonlinear susceptibilities are known as the "sum-over-states" (SOS) and the "length-gauge" formalisms developed by Sharma and Sipe respectively.[19–21] Depending on which software is used for DFT

calculations either approach may be implemented. The SOS formalism will be focussed on since it is the method used in the Elk code.

The SOS formalism involves determining the total number of excitations occurring within valence and conduction bands as well as between bands for a given photon energy/frequency. Excitations within the same band are always present and are known as the intraband component of nonlinear susceptibility. Above half the band gap energy of the material excitations from the conduction band dominates second-order nonlinear optical susceptibility, this is the interband component. Half the band gap energy is critical since photons with 2ω that are created by SHG have enough energy to excite charge carriers between bands. Finally, the interband and intraband components are added to get the total susceptibility. Since excitations within the band structure are being calculated it is necessary to have a dense k-point mesh when initializing your DFT calculation. Optical properties require large numbers of k-points to reach convergence.[22] Additionally, an accurate experimental band gap energy is crucial to determining optical properties since interband terms depend on this energy value. Since DFT calculations often underestimate the band gap energy the optical band gap is often obtained experimentally and used to correct the calculated band gap *post hoc* using a scissor operator. The scissor operator raises conduction bands to match the experimental band gap.

1.6   Designing NLO Compounds

To satisfy the demand for laser sources with a wider range of wavelengths there has been active research into discovering new nonlinear active compounds in the infrared (IR), visible, and ultraviolet (UV) regions. To achieve overall excellent performance the NLO compound must combine practical crystal growth and good physical properties for NLO applications. The criteria for excellent NLO performance include a large NLO coefficient, a wide transparency

range, a high laser damage threshold (LDT), and to melt congruently for the purposes of crystal growth.[23]

Since NLO phenomena are inherently weaker than linear optical behaviour there has been great interest in finding materials which are increasingly efficient at SHG. This is done by finding new compounds with large $\chi^{(2)}$. A wide transparency range is desirable particularly for down-conversion in the IR region where photons are converted to long wavelengths on the order of $8 - 12$ μm. Obviously, it would be undesirable for the compound's vibrational modes to absorb the SHG photons which it had just produced. A large LDT is desirable to increase the longevity of the NLO crystal. This is achieved by having wide band gap energies, therefore, limiting the number of photons the crystal absorbs. For this reason, oxides and chalcogenides are often used as the electronegative elements in these compounds. Chalcogenides are preferred over oxides for NLO applications in the IR region due to their much larger NLO susceptibilities. This is because S and Se are larger atoms and therefore more polarizable than O. This trend has been coined "anionic group theory" by Chen et al. to describe the increasing NLO susceptibilities of the anions as one descends a group.[24] Anionic group theory was originally created to describe the extremely large NLO susceptibilities in planar π – conjugated borates such as $[B_3O_6]^{3-}$ and $[BO_3]^{3-}$ relative to the tetrahedral $[BO_4]^{5-}$ anion.[25] In terms of the SOS formalism, the narrower band gaps of chalcogenides relative to oxides makes excitation between the valance bands and the conduction bands easier at lower energies thus increasing the interband component of $\chi^{(2)}$. By choosing to use compounds with narrower band gaps the SHG efficiency can be improved but at the cost of lowering the LDT. Ideally, the narrower band gap relative to oxides is still wide enough to not absorb a significant amount of light from the IR laser or the SHG light. The Bridgman-Stockbarger technique is the preferred method for NLO researchers to prepare large-

high-quality crystals. This requires the compound to melt congruently. Metal flux synthesis is avoided for incongruently melting compounds since the electronegative chalcogenides they contain form stable binaries with the metal flux.[26]

All the above criteria for discovering new NLO compounds is meaningless unless researchers can discover compounds which have NCS crystal structures. Strategies to design NCS compounds include using cations which undergo second-order Jahn-Teller (SOJT) distortions, using cations which contain a non-bonding lone pair of electrons, and incorporating NCS building blocks such as tetrahedrally coordinated polyatomic anions.[27] All of these factors are meant to decrease the local symmetry around a coordinated cation. SOJT distortions commonly occur in d^0 cations such as Ti^{4+}, V^{5+}, and W^{6+} with non-degenerate ground-states and low-lying excited states. Cations such as Tl^+, Pb^{2+}, Bi^{3+}, and Te^{4+} distort neighbouring atoms with a non-bonding lone pair of electrons.[28–31] NCS building blocks such as tetrahedral and trigonal planar polyatomic anions are useful since they are NCS themselves which makes the overall crystal structure more likely to be NCS. Finally, the most likely approach to reveal new NCS compounds is to begin with a known structure type such as the chalcopyrite structure (double zincblende) and begin substituting elements.[24,32–35] The majority of commercial IR NLO materials adopt the chalcopyrite structure but suffer from having low laser damage thresholds.[23]

1.7   Infrared NLO Compounds

As mentioned previously, there is ongoing research to discover new NLO compounds for use in the UV, visible, and IR regions. NLO compounds for the UV region contain extremely electronegative and electropositive elements to create compounds with wide band gaps such as $Ba_4B_{11}O_{20}F$[36] and $Sr_3Be_{11.9}B_{5.1}O_{12.1}F_{0.9}$.[37] Alternatively, by using chalcogens and phosphorus as the anion in a compound new IR NLO materials can be discovered.[23,38] The field of IR NLOs has

exploded in the last decade leading to the discovery of several new NLO compounds which outperform the state of art NLO compounds such as $Ba_{23}Ga_8Sb_2S_{38}$ whose SHG is 22 times more intense than the state-of-the-art IR NLO, $AgGaS_2$ ($d_{36} = 13$ pm V^{-1}).[39] One quickly realizes upon reading the relevant literature on IR NLOs that it is not too difficult to find a compound which has greater SHG intensity than $AgGaS_2$.[34,40–44] Many of these end up being overlooked, however, in favour of compounds which melt congruently and can be practically grown into large crystals.[45–47]

Table 3. Recently discovered IR NLO materials with tetrel and chalcogenide motifs.

Compound	Space Group	Experimental Band Gap (eV)	SHG Intensity
$LiNbO_3$	$R3c$	4.0 eV	$d_{11} = -30$ pm V^{-1}, $d_{31} = -5.9$ pm V^{-1}
$AgGaS_2$	$I\bar{4}2d$	2.64 eV	$d_{36} = 13$ pm V^{-1}
$AgGaSe_2$	$I\bar{4}2d$	1.8 eV	$d_{36} = 33$ pm V^{-1}
$LiGaGe_2Se_6$[47]	$Fdd2$	2.64 eV	$0.5 \times$ AGSe
$Ba_6Ag_{2.67}Sn_{4.33}S_{16}$[48]	$I\bar{4}3d$	1.58 eV	$1.2 \times$ AGSe
β-$K_2Hg_3Ge_2S_8$[49]	$C2$	2.70 eV	$10 \times LiNbO_3$
$Ba_7Sn_5S_{15}$[50]	$P6_3cm$	2.29 eV	$2 \times$ AGSe
$Ba_6Sn_6Se_{13}$[51]	$P2_12_12_1$	1.52 eV	$0.13 \times$ AGSe
$Ba_{23}GaSb_2S_{38}$[39]	$Cmc2_1$	2.84 eV	$22 \times$ AGS
$BaCdSnSe_4$[41]	$Fdd2$	1.79 eV	$1.3 \times$ AGS
$PbGa_2GeSe_6$[40,52]	$Fdd2$	1.96 eV	$12 \times$ AGS

1.8 Motivations

Tetrels and the chalcogenides have interested researchers for their structural diversity as well as for their attractive semiconducting properties in the fields of nonlinear optics,[49] ferroelectrics,[53,54] and as thermoelectric materials.[55] The preference for Ge to be tetravalent, as well as its ability to adopt a 3+ oxidation state by forming Ge – Ge bonds allows germanium to form several different chalco-germanate structural motifs such as $[GeQ_4]^{4-}$ (Q = S, Se), $[GeQ_5]^{4-}$,

$[Ge_2Q_5]^{4-}$, $[Ge_2Q_7]^{6-}$, $[Ge_2Q_6]^{6-}$, and $[Ge_4Q_{10}]^{8-}$.[56,57] Likewise, Se is able to form various

polyselenide anions such as Se_2^{2-}, Se_3^{2-}, and Se_5^{4-}.[35,58] The bond between Ge and Se is extremely

polarizable which leads to favourable NLO susceptibilities.

To explore the structural diversity of tetrels and identify candidates for future NLO

applications several new phases were identified. Unfortunately, most of the new phases

discovered by previous group members were centrosymmetric. $Ba_6Ge_2Se_{12}$ ($P2_1/c$), $Ba_7Ge_2Se_{17}$

(*Pnma*), and $Ba_8Sn_4Se_{17}$ (*C2/c*), all contain inversion symmetry and are therefore not capable of

SHG.[59] Explorations into Pb compounds revealed the NCS phase $Sr_{19-x}Pb_xGe_{11}Se_{44}$ ($P6_3$).[60] The

non-bonding lone-pair of electrons on the Pb^{2+} likely promoted crystallizing in a NCS space

group by distorting the local coordination of the Pb/Sr sites. While trying to identify the crystal

structure of $Sr_{19-x}Pb_xGe_{11}Se_{44}$ single crystals for $Sr_{1.31}Pb_{0.69}GeSe_4$ and β-Pb_2GeSe_4 were picked

leading to the identification of two more new phases. $Sr_{1.31}Pb_{0.69}GeSe_4$ adopts the same crystal

structure as γ–Sr_2GeSe_4 first identified by Johrendt et al.[53] γ–Sr_2GeSe_4 crystallizes in the NCS

space group *Ama*2 and belongs to the family of compounds with the general formula A_2TQ_4

where *A* is a divalent cation (alkaline Earth metals, Pb^{2+}, Zn^{2+}, Cd^{2+}, Hg^{2+}, Eu^{2+}), *T* is a group 14

tetravalent cation (Si^{4+}, Ge^{4+}, Sn^{4+}), and *Q* is a chalcogenide (S^{2-}, Se^{2-}, and Te^{2-}). This family of

compounds arise from the combination of the binaries *AQ* and TQ_2 in a simple 2:1 ratio:

$$2\ AQ + TQ_2 \rightarrow A_2TQ_4 \qquad\qquad (1.8.1)$$

Within this family of compounds, there is a variety of crystal structures. β-Pb_2GeSe_4 is

isostructural to β-Pb_2GeS_4 and adopts the centrosymmetric space group $P2_1/c$.[61] Since NLO

measurements were not performed on γ–Sr_2GeSe_4 when it was originally published and our

group possessed crystal structures for $Sr_{1.31}Pb_{0.69}GeSe_4$ and β-Pb_2GeSe_4 our goal became to

determine the what effect substituting Pb^{2+} onto the Sr^{2+} sites would have on the NLO properties

and at what stoichiometry the structure changed from the *Ama*2 space group to *P*2$_1$/*c*. Originally, our hypothesis was that by substituting Sr^{2+} with Pb^{2+} the NLO susceptibility should increase for three reasons: the distortions created by the lone pair of electrons on Pb^{2+}, the greater polarizability of the larger Pb^{2+} cation, and the decreased band gap arising from the substitution of a less electropositive element. This would be analogous to the strategy described by "anionic group theory" where instead of substituting more polarizable anions we are targeting the cation. All these compounds range in colour from orange to black indicating that their optical band gaps are less than 2.5 eV. This would limit these compound's uses in NLO applications to the IR region.

Recently, our group discovered $BaCuSiTe_3$, another NCS compound containing ethane-like $[Si_2Te_6]^{6-}$. $BaCuSiTe_3$ adopts the *Pc* space group and has dark red crystals meaning it would also have to be used in IR NLO applications to prevent absorption of the laser light. $[Si_2Te_6]^{6-}$ is a large anionic group and despite it not containing π – conjugated electrons, may be extremely polarizable leading to a large NLO susceptibility.

Beginning with the centrosymmetric compounds, the objective is to optimize the synthesis conditions of these compounds to perform physical property measurements on them. Unfortunately, even though our group is well equipped to measure thermoelectric properties the wide band gaps of these compounds indicated that these compounds would be poor candidates for thermoelectric applications. Due to this the primary focus for the centrosymmetric compounds was to obtain an experimental band gap, perform theoretical calculations, and refine the problematic crystal structure of $Ba_7Ge_2Se_7$. For the NCS compounds, their band gaps will be determined experimentally in order to use this value in theoretical NLO calculations of d_{eff} which will be compared to the experimental d_{eff} value.

2   Experimental Procedures

All the compounds above were prepared by high-temperature solid-state synthesis in evacuated and flame sealed silica tubes. Other synthesis methods such as molten flux growth were also explored for the purposes of growing single crystals. Fortunately, the procedures to synthesize the NCS compounds γ–Sr_2GeSe_4 and α–Pb_2GeSe_4 have already been reported including a phase diagram for the latter.[53,62,63] The synthesis procedures for the centrosymmetric compounds and $BaCuSiTe_3$ were developed by other group members.[64] Due to the air sensitivity of Ba and Sr, all weighing was performed inside an Ar filled glovebox. Each of these compounds will be talked about in more detail in the following section as well as methods to characterize materials and measure their physical and optical properties.

Table 4. List of the elements used and their purities.

Element	Form	Purity	Manufacturer
Strontium	Granules	99%	Alfa Aesar
Barium	Pieces	99.7%	Strem Chemicals
Copper	Powder	99.5%	Alfa Aesar
Silicon	Powder	99.9%	Alfa Aesar
Germanium	Chunk	99.999%	American Element
Tin	Granules	99.99%	Alfa Aesar
Lead	Granules	99.99%	Sigma Aldrich
Selenium	Pellets	99.99%	Sigma Aldrich
Tellurium	Broken Ingot	99.99%	Strem Chemicals

2.1 $Ba_7Ge_2Se_{17}$ and $Ba_6Ge_2Se_{12}$

$Ba_7Ge_2Se_{17}$ and $Ba_6Ge_2Se_{12}$ were synthesized by a direct reaction between constituent elements in glassy carbon crucibles sealed in silica tubes. Stoichiometric amounts of Ba, Ge, and Se were loaded into a glassy carbon crucible and placed inside a silica tube. Without the use of the glassy carbon crucible, elemental Ba reacts with the silica tube at high temperatures. The

samples must be homogenized and annealed a second time since it is common for the yellow Ba_2GeSe_4 to be visible after the first heating. This side product along with the binaries $BaSe_3$ in the case of $Ba_7Ge_2Se_{17}$ and $BaSe_2$ in the case of $Ba_6Ge_2Se_{12}$ are greatly reduced by annealing. $Ba_7Ge_2Se_{17}$ and $Ba_6Ge_2Se_{12}$ are black and brown respectively.

2.2 $Ba_8Sn_4Se_{17}$

$Ba_8Sn_4Se_{17}$ was synthesized similarly to $Ba_7Ge_2Se_{17}$ and $Ba_6Ge_2Se_{12}$ replacing Ge with Sn where necessary. Stoichiometric amounts of Ba, Sn, and Se were loaded into glassy carbon crucibles, placed inside evacuated silica tubes, and flame sealed.

The initial heating for these two compounds is the same as with $Ba_7Ge_2Se_{17}$ and $Ba_6Ge_2Se_{12}$, however, the samples mostly comprised the yellow Ba_2SnSe_4 at this point. As explained previously, Ba_2SnSe_4 has a similar stoichiometry as the target compound. The sample was homogenized and annealed at 773 K for a month to allow the elements to diffuse and become homogenous. After this long annealing time, the $Ba_8Sn_4Se_{17}$ was obtained, as indicated by the desired orange colour.

2.3 γ–Sr_2GeSe_4 (x = 0)

Sr_2GeSe_4 has three structural variants. Fortunately, this is discussed in Tampier's Ph.D. dissertation from 2002, which simplified the synthesis of the γ–Sr_2GeSe_4 target.[65] When Sr_2GeSe_4 is synthesized directly from the elements, the yellow α-Sr_2GeSe_4 forms. The α polymorph undergoes a reversible phase change to the β-Sr_2GeSe_4 polymorph at 600 K. The α and β structures were never reported outside the dissertation. The dissertation claims that γ–Sr_2GeSe_4 could only be prepared by first making the binary Sr_2Ge and combining it with a

stoichiometric amount of Se. Stoichiometric amounts of Sr and Ge were added to a glassy carbon crucible and sealed inside a silica tube.

$$\text{Sr}_2\text{Ge} + 4\,\text{Se} \rightarrow \text{Sr}_2\text{GeSe}_4 \qquad (2.3.1)$$

The original paper describes this reaction being done with an alumina crucible instead, but when an alumina crucible is used the Sr_2Ge would become fused to the walls of the alumina crucible making it impossible to remove so a glassy carbon crucible was substituted.[53] The tube was heated at 1173 K for 12 hours to give a brittle metallic grey ingot. The Sr_2Ge synthesized was extremely air-sensitive so it was ground and stored inside the glove box. The Sr_2Ge was loaded into a glassy silica crucible and sealed inside a large evacuated silica tube. Again, an alumina crucible was called for here but that was substituted. A large tube was used here since the next step called for placing the silica tube directly into a preheated 1173 K furnace for two hours. After two hours the sample was quenched in an ice bath. Using these reaction conditions, γ–Sr_2GeSe_4 could be made along with the side products SrSe, GeSe_2, and α-Sr_2GeSe_4. Unfortunately, annealing γ–Sr_2GeSe_4 causes it to be converted to the α-Sr_2GeSe_4 polymorph, meaning it is not possible to completely remove the SrSe and GeSe_2 from the sample. Although SrSe and GeSe_2 both crystallize in centrosymmetric crystal structures and therefore would not impact the SHG measurements, α-Sr_2GeSe_4 crystallizes in the $P2_1$ space group and thus would impact SHG measurements.

After extensive exploration into the synthesis of γ–Sr_2GeSe_4 it was found that the γ polymorph could be made in a single heating with only nominal amounts of SrSe and α-Sr_2GeSe_4 visible in the powder XRD and without the need of first preparing Sr_2Ge. Grinding the sample and annealing further was not attempted to avoid the conversion to the α polymorph.

19

2.4 $Sr_{1.3}Pb_{0.7}GeSe_4$ (x = 0.7)

Unlike γ–Sr_2GeSe_4, $Sr_{1.3}Pb_{0.7}GeSe_4$ retains the γ–Sr_2GeSe_4 structure type after annealing

meaning it can be made pure. Stoichiometric amounts of Sr_2Ge, Pb, Ge, and Se were added to a

glassy carbon crucible and sealed inside of an evacuated silica tube.

$$\left(1 - \frac{x}{2}\right) Sr_2Ge + x\, Pb + \left(\frac{x}{2}\right) Ge + 4\, Se \rightarrow Sr_{2-x}Pb_xGeSe_4 \qquad (2.4.1)$$
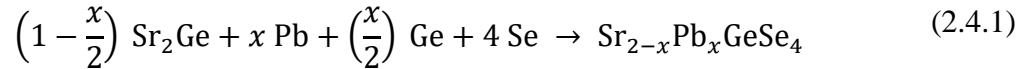
Equation (2.4.1) was used to determine the stoichiometric ratios for any solid solution between

Sr_2GeSe_4 to Pb_2GeSe_4. Pb and Ge do not form stable solid solutions such as "Pb_2Ge" so the raw

elements must be used.[66] Like the γ–Sr_2GeSe_4 samples the sealed tubes were placed into a

preheated manual furnace at 1173 K for two hours and then quenched in an ice bath. The

ampoules were opened and ground to make a homogenous powder before being resealed in

ampoules and annealed at 773 K for one week. The result was a homogenous dark brown

powder.

2.5 $Sr_{0.25}Pb_{1.75}GeSe_4$ and Pb_2GeSe_4 (x = 1.75 and 2)

$Sr_{0.25}Pb_{1.75}GeSe_4$ and Pb_2GeSe_4 can be prepared the using the same procedure. Sr_2Ge was

not necessary for making $Sr_{0.25}Pb_{1.75}GeSe_4$ so it was avoided to save time. The $PbSe - GeSe_2$

phase diagram has been reported.[62] Pb_2GeSe_4 exists at the 67% PbSe point in the phase diagram.

At 863 K Pb_2GeSe_4 melts incongruently into PbSe and a liquidus phase. PbSe also melts at 1123

K at the 67% point in the phase diagram. It was assumed that the 0.25 moles of Sr, that were

substituted into Pb_2GeSe_4 to make $Sr_{0.25}Pb_{1.75}GeSe_4$, would not alter these melting points greatly.

Stoichiometric amounts of Sr, Pb, Ge, and Se were loaded into carbon-coated silica tubes,

evacuated and flame sealed. Pb does not react with the silica container at high temperatures and

due to $Sr_{0.25}Pb_{1.75}GeSe_4$ containing only a small amount of Sr, glassy carbon crucibles were not

necessary. The silica tubes were still carbon-coated as a precaution. The sealed ampoules were loaded into a furnace which was ramped up to 1173 K at a rate of 100 K per hour. The ampoules were left at 1173 K for two hours to ensure the entire sample was melted and homogenous. After two hours the ampoules were quenched in an ice bath. At this point, the cubic $Sr_{0.25}Pb_{1.75}GeSe_4$ and Pb_2GeSe_4 phases are clearly identifiable in powder XRD diagrams, which also contain PbSe and $GeSe_2$, so the samples are homogenized, loaded back into silica tubes and annealed at 773 K for one week.

2.6 BaCuSiTe$_3$

BaCuSiTe$_3$ was prepared by adding Ba, Cu, Si, and Te in stoichiometric ratios into a glassy carbon crucible. This crucible was placed into a silica tube, evacuated, and flame sealed. The ampoule was then placed into a programmable furnace and heated to 973 K within 10 hours and remained at this temperature for two hours to ensure that all the elements had completely reacted. The furnace was then cooled down to room temperature over 24 hours. The sample was then homogenized and resealed in an ampoule and annealed at 673 K for one week. This produced a nearly black powder with several red crystals.

2.7 Flux Synthesis

Flux synthesis was explored to obtain high-quality crystal structures for $Sr_{0.25}Pb_{1.75}GeSe_4$ and α-Pb$_2$GeSe$_4$. Although α-Pb$_2$GeSe$_4$ is known to be isostructural to α-Pb$_2$GeS$_4$ only the refined lattice parameters of α-Pb$_2$GeSe$_4$ have been reported to be $a = 14.573$ Å.[63] Since both $Sr_{0.25}Pb_{1.75}GeSe_4$ and Pb_2GeSe_4 melt incongruently growing single crystals by slowly cooling the melt was not possible.

Flux synthesis is a high-temperature synthesis method where in addition to the elements being reacted a "flux" is also added. The flux melts and acts as a solvent for crystallization to take place in.[26] Metal fluxes have been successful in crystallizing the similar A_2TQ_4 such as Ba_2SnSe_4 and $BaCdSnSe_4$.[41] Due to the stability of the binaries formed with chalcogens such as Se a large excess of metal flux would consume all of the Se, leaving none to form the target compound. Therefore, in the cases of Ba_2SnSe_4 and $BaCdSnSe_4$, only a small amount of Zn and Cd were added to the reaction vessels. To work around Se forming stable binaries with metal fluxes, a self-fluxing approach can be used where a small excess of Se is added to the reaction to act as a flux.[67] Halide fluxes are also commonly used. $BaAg_2GeSe_4$ and $BaAg_2SnSe_4$ have been prepared using a $BaCl_2$ flux.[34] Halide fluxes can be useful if the target compound is water stable, in which case the flux can be washed away with deionized water.

2.8 Powder and Single Crystal X-ray Diffraction

X-ray diffraction (XRD) is a powerful tool for compositional analysis and determining the purity of a sample. XRD is used to identify the crystal structures of materials, and therefore the XRD pattern of a material is a unique "fingerprint." Powder XRD patterns were obtained using the INEL XRG 3000 diffractometer with a position-sensitive detector and Cu $K_{\alpha1}$ radiation with the $K_{\alpha2}$ wavelength filtered.

The X-rays in the diffractometer are created by accelerating electrons through a ~ 30 kV electric field and colliding them with a Cu block. These electrons knock out low energy electrons in the Cu metal from the $1s$ orbital leaving a vacancy. As electrons drop in energy to fill this hole they give off energy in the form of photons of characteristic wavelengths. The $K_{\alpha1}$ and $K_{\alpha2}$ of Cu are produced in a 2:1 ratio. The $K_{\alpha1}$ and $K_{\alpha2}$ radiation are passed through a monochromator and a

collimator before hitting the sample. The energy of the X-ray photon is equal to the difference in energy between the valence electron's original position and energy of the $1s$ orbital.

XRD obeys Bragg's Law, which allows for the lattice spacing to be calculated using the angle of refraction.

$$2dsin\theta = n\lambda \tag{2.8.1}$$

Where d is the diffraction plane spacing, n is a positive integer, λ is the wavelength of the X-ray, and θ is the angle between the incident beam and the diffraction plane. Intensities of the diffracted X-ray beam decrease at higher values of θ due to the diffuse nature of the electron clouds interacting with the X-rays at these angles. Longer experiment times may be needed to resolve peaks in this region.

In single-crystal experiments, the crystal is attached to a four-circle goniometer to precisely change the angle of the incident beam. The diffracted beams are detected to give a pattern of the corresponding lattice in reciprocal space. Using a program like SHELXTL,[68] the real lattice may be derived from the reciprocal lattice and precise coordinates of atoms can be obtained in this method. Single crystal diffraction can even be used to identify vacancies or substitutions using atomic scattering factors which are proportional to the number of electrons around the atom. This can be used for elements that are significantly different in atomic number, however, it falls short in separating elements of adjacent atomic numbers. This is a useful feature in refining the occupancies of the sites that have Sr/Pb mixing in $Sr_{2-x}Pb_xGeSe_4$.

The accuracy of a model is measured using the values residual factor and weighted residual factors R_1 and wR_2 respectively. These compare the observed structure factors F_{obs} with the calculated structure factor of the model F_{calc}.

$$R_1 = \frac{\sum |F_{obs}{}^2 - F_{calc}{}^2|}{\sum F_{obs}{}^2} \tag{2.8.2}$$

The weighted residual factor is scaled by the factor w which is related to the standard deviation in the model and observed data (σ).

$$w = \frac{1}{\sigma^2} \tag{2.8.3}$$

$$wR_2 = \frac{\sum w|F_{obs}{}^2 - F_{calc}{}^2|}{\sum wF_{obs}{}^2} \tag{2.8.4}$$

Analogous expressions for R_1 and wR_2 exist for powder XRD patterns. Rietveld refinements compare the simulated intensities (y_{calc}) of a crystallographic model with the observed intensities (y_{obs}) give R_p and wR_P.

$$R_p = \frac{\sum |y_{obs} - y_{calc}|}{\sum y_{obs}} \tag{2.8.5}$$

$$wR_p = \left[\frac{\sum w(y_{obs} - y_{calc})^2}{\sum wy_{obs}{}^2} \right]^{1/2} \tag{2.8.6}$$

For powder XRD the samples are ground finely in an agate mortar and pestle and placed in a shallow aluminum sample holder. The sample holder is mounted on a rotating platform. In powder XRD the assumption is made that in a homogenous powder all crystal faces are exposed equally. Rotating the dish averages out any variation in this assumption.

2.9 Band Gap Determination

To increase the precision of the theoretically calculated optical properties the calculated band gap is often corrected to the experimental value using a scissor operator. For solid samples such as the ones described here the spectrometer is set up to measure the diffuse reflectance of a

pelletized sample and the reflectance is then converted to absorbance which is used to determine the optical band gap graphically. For these compounds, the PerkinElmer Lambda 1050 UV/VIS/NIR Spectrometer was used since it allowed for measurements into the near IR region where the band gap for several of these selenogermanates resides. Using the Kubelka-Munk equation, (2.10.1), the reflectance can be converted to absorbance.

$$\frac{a}{S} = \frac{(1-R)^2}{2R} \qquad (2.10.1)$$

Where R is the percent reflectance written as a decimal, a is the absorbance, and S is a scattering factor which is approximately constant for material with particles sizes greater than ~ 5 μm. Once the a/S term is determined, it is plotted versus wavelength or the corresponding energies. The band gap can be determined, from this plot by drawing a line through the linear region of the plot where absorbance begins to increase before plateauing. The straight line drawn through this increasing portion of the plot is extrapolated to the baseline and this value on the x-axis is the energy corresponding to the optical band gap of the material. At this energy, photons begin having enough energy to excite electrons from the valence band maximum to the conduction band minimum. This is indicated by the sharp increase in absorbance beyond this point.

An alternative method to determine the band gap is to measure the change in electrical conductivity with respect to temperature. This is because the intrinsic charge carriers need to be thermally activated to cross from the valence band to the conduction band and start conducting electricity. Electrical conductivity is measured using the "four-point method" which involves attaching four wires to a bar cut from the hot-pressed pellet. The two centre wires measure voltage (V) whereas the two outer wires provide the known current (I). Using Ohm's law ($V = I \times R$) resistance may be calculated. Using the dimensions of the pellet, the resistivity (ρ) and

conductivity (σ) may be calculated from resistance. The instrument records conductivity versus temperature, which obeys the Arrhenius equation (2.10.2) in case of intrinsic semiconductors.

$$\sigma = \sigma_0 e^{-\frac{E_g}{2k_B T}} \tag{2.10.2}$$

Where E_g is the band gap, k_B is the Boltzmann constant, T is temperature and σ_0 is a pre-exponential factor. By plotting $\ln(\sigma)$ versus $1/T$, a straight line results with its slope equal to -$E_g/2k_B$. From this slope, it is trivial to obtain the band gap.

2.10 Hot-Pressing

After verifying the purity of the sample, the ground samples must be hot-pressed into dense pellets to be prepared for the NLO measurements. The hot-press used in these experiments was the Oxy-Gon hot-press machine with an upper limit of 30 tons. Powdered samples were loaded into graphite dies with a 12.7 mm diameter. The combination of high temperature and pressure consolidates the powders into dense pellets. To prevent the oxidation of the hot-press' heating elements and the samples, an atmosphere of 5% hydrogen and 95% argon flowed through the hot-pressing chamber. To prevent the decomposition of the samples moderate temperatures of 573 K was used for $BaCuSiTe_3$ and 623 K for $Sr_{2-x}Pb_xGeSe_4$ (x = 0, 0.7, 1.75, 2). 67 MPa of pressure was applied for five hours to consolidate the pellets. Despite attempts to optimize the hot pressing conditions the pellets of $Sr_{0.25}Pb_{1.75}GeSe_4$ and α-Pb_2GeSe_4 were extremely brittle, with α-Pb_2GeSe_4 beginning to crumble as soon as it was removed from the graphite die. Fortunately, improving the density of the samples had already been achieved and the samples were about to be broken up and sieved anyways for the NLO phase-matching measurements. After hot-pressing, the samples were set aside to be mailed to the University of Houston to have their NLO properties measured by Professor P. Shiv Halasyamani's group.

2.11 Nonlinear Optical Property Measurements

To perform SHG intensity measurements group reached out to the Halasyamani group at the University of Houston who has almost two decades of experience researching NLO materials. After mailing the hot-pressed pellets to the University of Houston the samples were ground and sieved into the particle sizes: < 20 μm, 20 μm – 45 μm, 45 μm – 63 μm, 63 μm – 75 μm, 75 μm – 90 μm, and 90 μm – 125 μm. The reason for hot-pressing and acquiring samples with high densities was to have uniform particles when the sample is broken up and sieved for the phase-matching measurements. The separated powders were loaded into silica tubes with an inner diameter of 4 mm and flame sealed. Inside a lightbox, the samples in the glass tubes are hit with a 1064 nm Nd:YAG laser. Due to the shape of the cylindrical silica tube, a focusing mirror is required to collect the SHG light and direct it into a detector. Before entering the detector, a short pass filter is used to filter out backscattered 1064 nm from the laser source and only enable the 532 nm light produced by SHG to enter the detector. As mentioned above, a PMT is used since it is the only detector sensitive enough to detect the SHG signal from powders. The PMT signal is read out on an oscilloscope in arbitrary units.[13] By measuring the SHG intensity with respect to particle size the phase-matching behaviour of the material at a given wavelength may be determined.[11] Ideally, a laser with a wavelength of 2 μm would be used to measure the properties of an IR NLO materials since a portion of the SHG light can be absorbed if it has greater energy than the band gap. This was the case with the compounds reported here since the 532 nm light produced by SHG could get absorbed by all of them.

The most important aspect of this measurement is to compare the SHG intensities of the new material with a standard to give meaning to PMT's arbitrary signal. Depending on whether the material phase matches or not a corresponding phase-matching or non-phase-matching

standard is compared. For phase-matching materials, $LiNbO_3$ can be used whereas for non-phase-matching materials α–SiO_2 can be used. Using either equation (1.4.6) or (1.4.7) the d_{eff} of the new material can be calculated.

2.12 Theoretical Nonlinear Optical Properties

The theoretical d_{ij} values calculated by the Elk code will be compared to the experimental d_{eff} by means of equation (1.3.1). This is a straightforward procedure for γ–Sr_2GeSe_4 since there is no mixing of Pb onto the Sr sites yet and there are no partially occupied sites. The DFT software attempts to solve a Schrödinger equation that is periodic over the volume of a unit cell. If there were random vacancies or substitutions in the unit cell, creating a periodic function would be impossible. This can be worked around by creating a so-called supercell with the desired stoichiometry where certain cites are fixed to contain a certain atom or be empty entirely. This can be at the cost of lowering the symmetry of the unit cell. This is the approach taken to calculate the theoretical d_{ij} values for $Sr_{1.3}Pb_{0.7}GeSe_4$. To create a supercell for $Sr_{1.3}Pb_{0.7}GeSe_4$ the approximation was made that a quarter of the Sr sites were filled with Pb giving the stoichiometry "$Sr_{1.5}Pb_{0.5}GeSe_4$". While γ–Sr_2GeSe_4 and $Sr_{1.3}Pb_{0.7}GeSe_4$ have the orthorhombic *Ama*2 symmetry, the "$Sr_{1.5}Pb_{0.5}GeSe_4$" model is monoclinic with *Pm* symmetry. This had the consequence of significantly increasing the number of unique d_{ij} values in the second-order NLO susceptibility tensor due to the decreased symmetry. Since the additional d_{ij} could still be reduced to a d_{eff} value through equation (1.3.1), the hope was that this approach would make it possible to determine the theoretical d_{ij} for crystal structures with partially occupied and mixed sites. To the best of our knowledge, this approach to calculate d_{ij} has not been attempted before.

The crystal structures of $Sr_{0.25}Pb_{1.75}GeSe_4$ and α-Pb_2GeSe_4 contain both vacancies and mixed sites. The unit cells of these compounds are extremely large and contain more than 100

atoms meaning computations of these compounds would be extremely time-consuming

especially if a supercell was made. Since these compounds are cubic, they do not display

birefringence and therefore would not be phase matchable. Realizing this we did not try to

calculate the NLO properties of these two compounds since their NLO properties would be poor.

Only the experimental measurements were performed for $Sr_{0.25}Pb_{1.75}GeSe_4$ and $\alpha\text{-}Pb_2GeSe_4$.

3 Results and Discussion

3.1 Synthesis and Crystal Structures

The weighing of all elements in the following section was done in an Ar filled glovebox to prevent the oxidation of air-sensitive elements such as Ba and Sr. Due to the reactivity of these alkaline earth metals glassy carbon crucibles were used in most cases to prevent the reaction with the silica tube. Powder XRD was performed on an INEL XRG 3000 diffractometer for purity analysis and to perform Rietveld refinements on $Ba_7Ge_2Se_{17}$. Crystal structures were determined by single-crystal XRD on a Bruker Kappa Apex II CCD at room temperature.

3.1.1 $Ba_7Ge_2Se_{17}$

$Ba_7Ge_2Se_{17}$ was prepared through high-temperature solid-state synthesis by adding stoichiometric amounts of Ba (99.7%), Ge (99.999%), and Se (99.99%) into a glassy carbon crucible in a silica tube and evacuating the tube to 2.5×10^{-3} mbar. The evacuated tube was flame sealed and placed into a programmable furnace to be heated to 923 K for 12 hours, slowly cooled to 573 K, and finally, the furnace was turned off. At this point, a black needle-shaped crystal was picked from the sample that was suitable for single-crystal XRD. The sample can be ground and resealed at this point to be annealed at 573 K to decrease the number of side products in the sample. Ba_2GeSe_4 and $BaSe_3$ would often form in the competing the side reaction:

$$7 \text{ Ba} + 2 \text{ Ge} + 17 \text{ Se} \rightarrow 2 \text{ Ba}_2\text{GeSe}_4 + 3 \text{ BaSe}_3 \qquad (3.1.1.1)$$
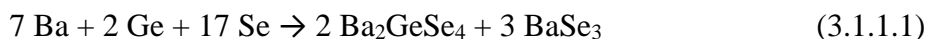
$Ba_7Ge_2Se_{17}$ adopts the orthorhombic *Pnma* space group with $a = 12.6508(5)$ Å, $b = 20.0395(9)$ Å, and $c = 12.2936(6)$ Å. $Ba_7Ge_2Se_{17}$ may be written as $(Ba^{2+})_7(GeSe_5^{4-})_2(Se_2^{2-})_2(Se_3^{2-})$ to clearly identify anionic groups in the structure. Initially, the crystal structure had several split Ge and Se positions. The refinement of $Ba_7Ge_2Se_{17}$ is further discussed below.

$Ba_7Ge_2Se_{17}$ has the narrowest optical band gap of the centrosymmetric compounds discussed here.
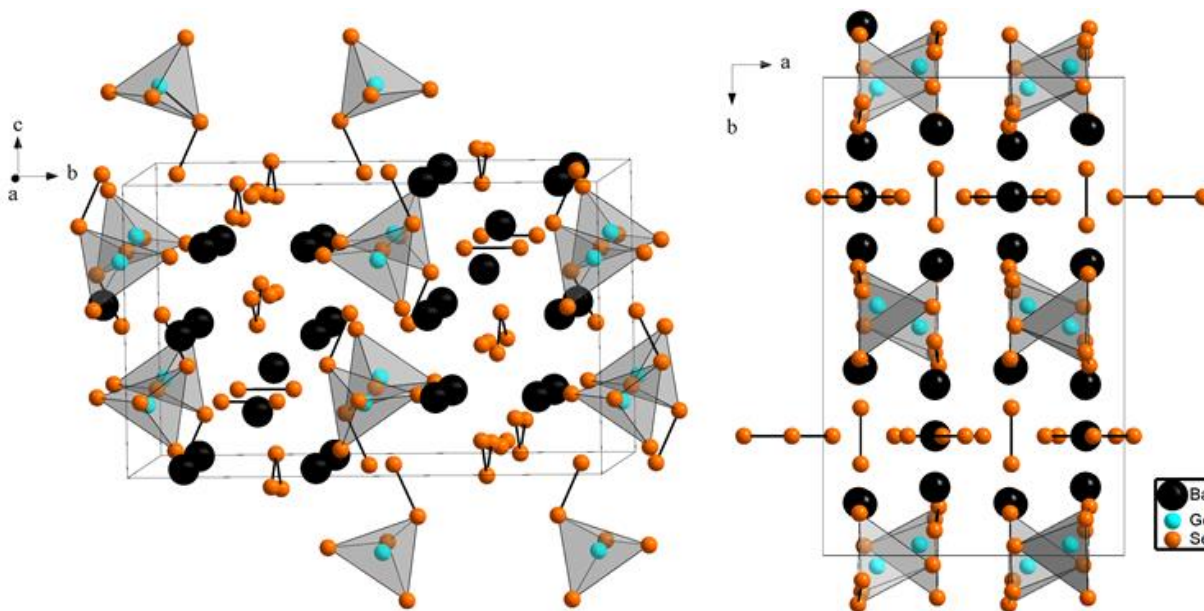
Figure 2. The unit cell of $Ba_7Ge_2Se_{17}$ (left). Alternating layers of polyselenides and selenogermanate tetrahedra as viewed from the *ab* plane (right).
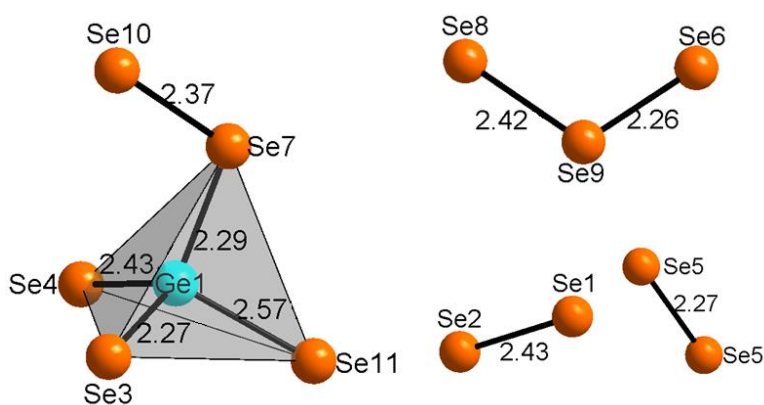
Figure 3. Geometries and bond distances in Ångstroms of the $[GeSe_5]^{4-}$, Se_2^{2-}, and Se_3^{2-} anions present in $Ba_7Ge_2Se_{17}$.
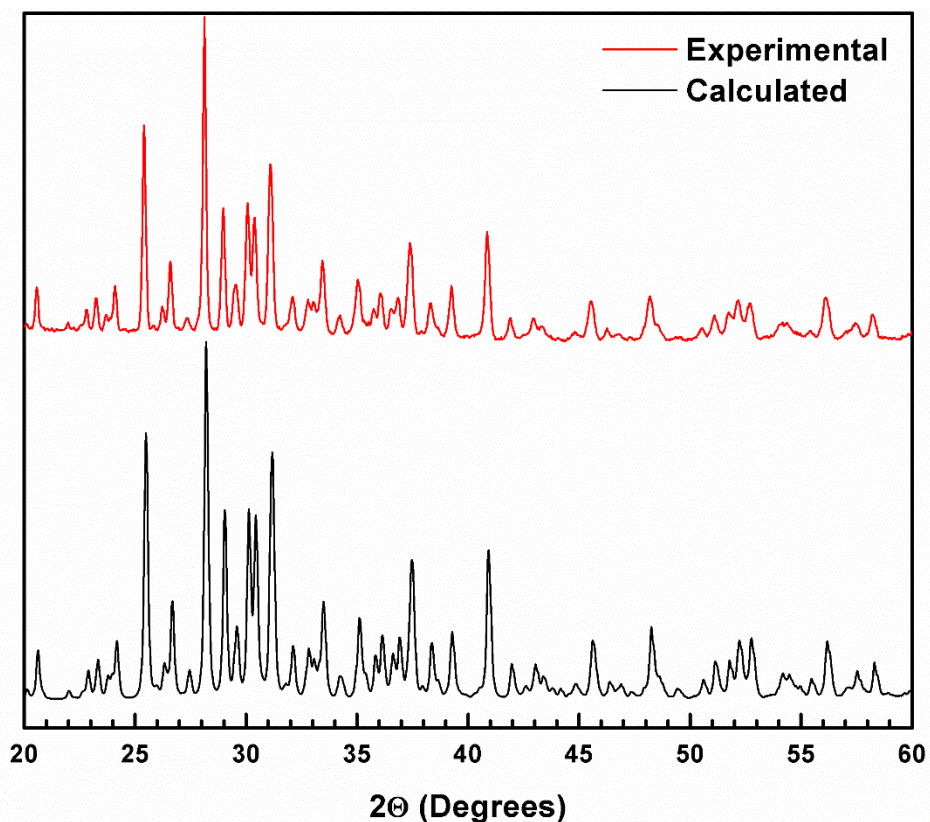
Figure 4. Powder XRD of $Ba_7Ge_2Se_{17}$ after annealing.

The single crystal data for $Ba_7Ge_2Se_{17}$ had several Ge and Se sites were split. Initial attempts to resolve this involved picking several more crystals to perform single-crystal XRD on, but this was unsuccessful as all the single-crystal refinements had the same split positions present. Because of the difficulty in resolving the split sites in using single-crystal XRD, Rietveld refinements using several models of $Ba_7Ge_2Se_{17}$ were performed. A Rietveld refinement is a technique that compares the simulated powder pattern of a crystallographic model with the experimental powder pattern. By making alterations to the model until it has a good fit with the experimental data, the crystallographic model can be refined. The split positions are highlighted in Figure 5. Upon close inspection, this was a result of two separate $[GeSe_5]^{4-}$ tetrahedra overlapping at 180^0 to each other. Rietveld refinements were performed using a model which had

split occupancies and another one where atoms associated only the Ge1B centered tetrahedra were deleted and atoms in the Ge1A centered tetrahedra had their occupancies fixed at 100%. The atoms around the Ge1A tetrahedra already had occupancies greater than 80%. In the refinement with splitting, the model was constrained to have the occupancies of corresponding atoms in each tetrahedra sum to 100%. After refining the model with split occupancies, the refinement assigned negative anisotropic values to the atoms associated only with the Ge1B centered tetrahedra which are physically impossible. Figure 6 shows the second model where atoms associated only with the Ge1B centered tetrahedra were deleted completely and there were no split positions. The χ^2 and R_f of this refinement were 10.8 and 0.069 respectively.

The anisotropy values associated with the atoms in the Ge1A centred tetrahedra ended up being significantly larger than the rest of the atoms indicating that there is not enough electron density at these positions. The negative anisotropic values in the Ge1B centered tetrahedra are an indication that there is not enough electron density assigned to those positions.
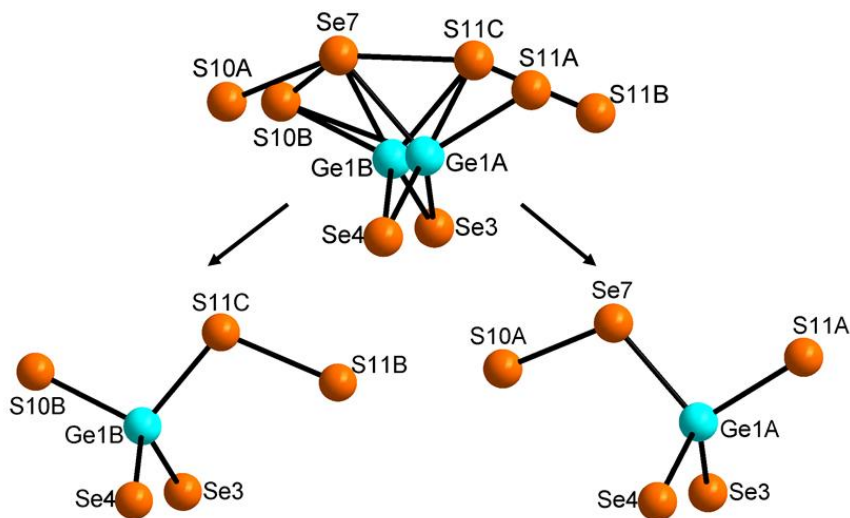
Figure 5. Split Ge and Se positions in the $[GeSe_5]^{4-}$ tetrahedra of $Ba_7Ge_2Se_{17}$.
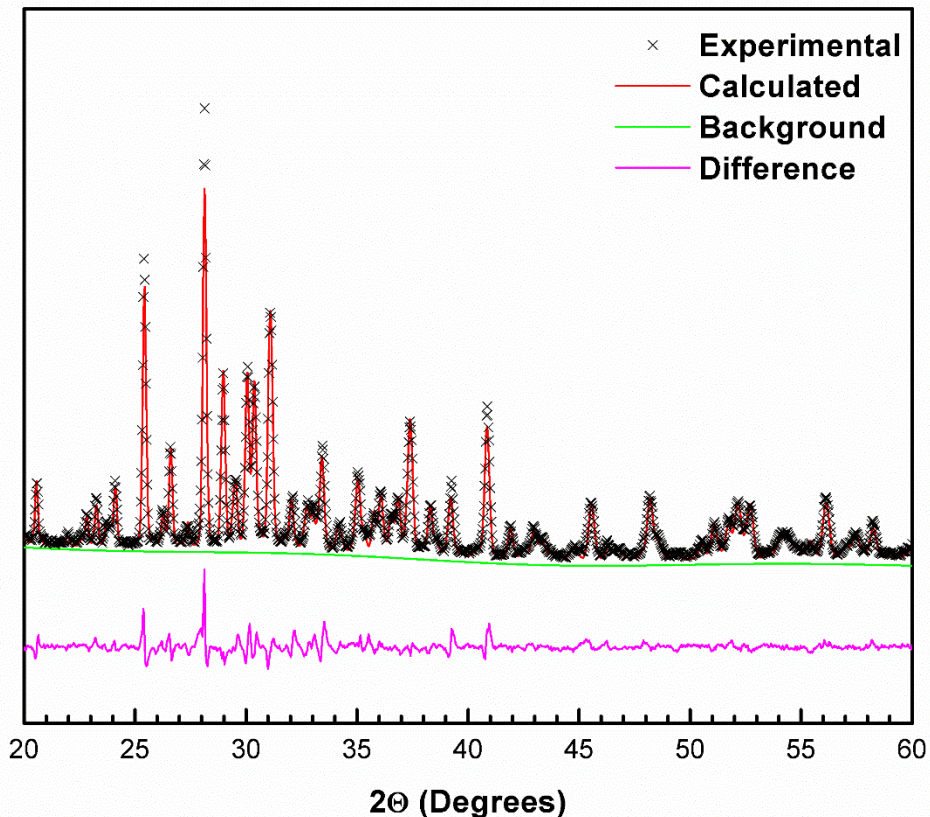
Figure 6. Rietveld refinement of $Ba_7Ge_2Se_{17}$.

Table 5. Crystallographic parameters of $Ba_7Ge_2Se_{17}$ before and after the Rietveld refinement.

Refined Formula	$Ba_7Ge_2Se_{17}$ Single Crystal	$Ba_7Ge_2Se_{17}$ Rietveld
Crystal System	Orthorhombic	Orthorhombic
Molecular Weight (g mol^{-1})	2448.81	2448.81
Space group	$Pnma$ (no. 51)	$Pnma$ (no. 51)
a (Å)	12.6518(1)	12.6506(5)
b (Å)	20.0692(6)	20.0396(9)
c (Å)	12.3067(9)	12.2936(6)
Unit cell volume (Å^3)	3124.82	3116.61
Formula units per unit cell, Z	4	4
Density (g mol^{-1})	5.205	5.206
Radiation, wavelength (Å)	Mo Kα 0.71073	Cu Kα 1.5406
Temperature (K)	296	296
F(000)	4136	4136
Absorption coefficient, μ (mm^{-1})	30.361	
R_1/R_p	0.049	0.032

wR$_2$/wR$_p$	0.081	0.045
Goodness of fit, GOF	1.288	
χ^2		10.77
R$_f$		0.069

Table 6. Atomic coordinates and displacement parameters of Ba$_7$Ge$_2$Se$_{17}$ after the Rietveld refinement.

Atom	Wyckoff Position	x	y	z	U$_{eq}$	Occupancy
Ba1	8d	0.1284(1)	0.14191(2)	0.7445(7)	0.0068(3)	1
Ba2	8d	0.3743(9)	0.1078(4)	0.0224(5)	0.019(4)	1
Ba3	8d	0.3810(9)	0.1092(5)	0.4772(6)	0.019(4)	1
Ba4	4c	0.1201(1)	0.25	0.3023(7)	0.035(4)	1
Ge1	8d	0.1749(6)	0.01929(2)	0.2549(4)	0.0401(3)	1
Se1	4c	0.2271(2)	0.25	0.5710(8)	0.003(4)	1
Se2	4c	0.0338(2)	0.25	0.5521(8)	0.010(4)	1
Se3	8d	0.1233(6)	0.58897(2)	0.2502(4)	0.0085(3)	1
Se4	8d	0.3684(6)	0.01873(2)	0.2522(4)	0.0145(3)	1
Se5	8d	0.3700(2)	0.19321(4)	0.2655(1)	0.029(5)	1
Se6	4c	0.2609(1)	0.25	0.9023(1)	0.033(5)	1
Se7	8d	0.1183(6)	0.10224(2)	0.1424(4)	0.0367(3)	1
Se8	4c	0.4663(1)	0.25	0.6172(1)	0.036(5)	1
Se9	4c	0.1136(1)	0.25	0.0086(1)	0.078(5)	1
Se10	8d	0.3719(6)	0.55221(2)	0.4684(4)	0.0181(3)	1
Se11	8d	0.1229(6)	0.07141(2)	0.4402(4)	0.0617(3)	1

Table 7. Selected interatomic distances (Å) in Ba$_7$Ge$_2$Se$_{17}$.

Ge1-Se3	2.266(7)	Se1-Se2	2.45575(10)
Ge1-Se4	2.44874(10)	Se5-Se5	2.276(14)
Ge1-Se7	2.27751(7)	Se8-Se9	2.422(17)
Ge1-Se11	2.59130(9)	Se6-Se9	2.27523(7)
Se7-Se10	2.3656(8)		

3.1.2 $Ba_6Ge_2Se_{12}$

$Ba_6Ge_2Se_{12}$ was prepared through high-temperature solid-state synthesis by adding stoichiometric amounts of Ba (99.7%), Ge (99.999%), and Se (99.99%) into a glassy carbon crucible in a silica tube and evacuating the tube to 2.5×10^{-3} mbar. The evacuated tubes were flame sealed. To grow crystals suitable for single-crystal XRD, $Ba_6Ge_2Se_{12}$ was heated to 923 K for 12 hours, slowly cooled to 573 K, and finally, the furnace was turned off. This resulted in several red platelets that were suitable for single-crystal XRD. The major side products of this reaction are Ba_2GeSe_4 and $BaSe_2$ which can be balanced in equation (3.1.2.1):

$$6\ Ba + 2\ Ge + 12\ Se \rightarrow 2\ Ba_2GeSe_4 + 2\ BaSe_2 \qquad (3.1.2.1)$$
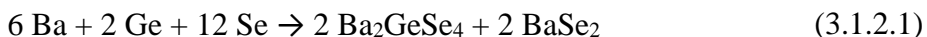
Annealing the sample at 773 K for one week, the peaks associated with Ba_2GeSe_4 and $BaSe_2$ disappeared, but peaks which could not be indexed remained. These are highlighted in Figure 8. These unknown peaks did not belong to any oxides.

$Ba_6Ge_2Se_{12}$ adopts the monoclinic $P2_1/c$ space group with the unit cell parameters $a = 10.0903(2)$ Å, $b = 9.3640(2)$ Å, $c = 25.7643(5)$ Å, and $\beta = 90.303(1)$ °. $Ba_6Ge_2Se_{12}$ is composed of $[GeSe_4]^{4-}$, Se_2^{2-} and a novel 1-D chain of Se^- ions. $Ba_6Ge_2Se_{12}$ may be written as $(Ba^{2+})_6(GeSe_4^{4-})_2(Se_2^{2-})(Se^-)_2$. The structure of $Ba_6Ge_2Se_{12}$ consists of zig-zagging rows of $[GeSe_4]^{4-}$ tetrahedra running antiparallel to each other in a bc plane while 1-D chains of Se^- run parallel to the a-axis. $Ba_6Ge_2Se_{12}$ is a brown powder. The 1-D chain is made up of selenium atoms denoted as Se11 and Se12. Each of these atoms was split into two sites denoted as A and B in Table 9. To satisfy the electron density in the A and B sites, the occupancies were refined to be 78% and 22% respectively.
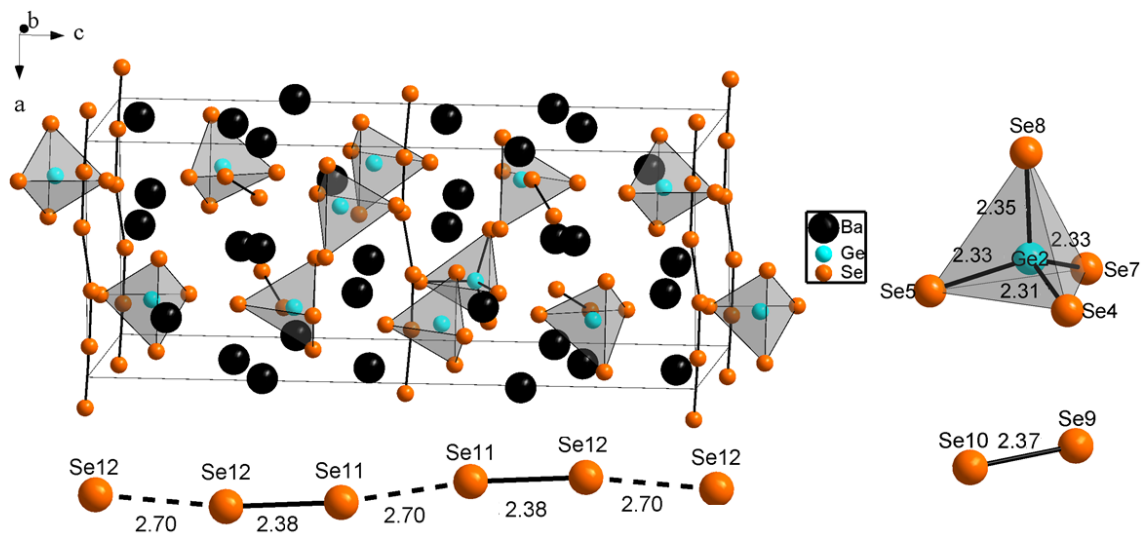
Figure 7. Geometries and bond distances in Ångstroms of the $[GeSe_4]^{4-}$, Se_2^{2-}, and Se^- chains present in $Ba_6Ge_2Se_{12}$.

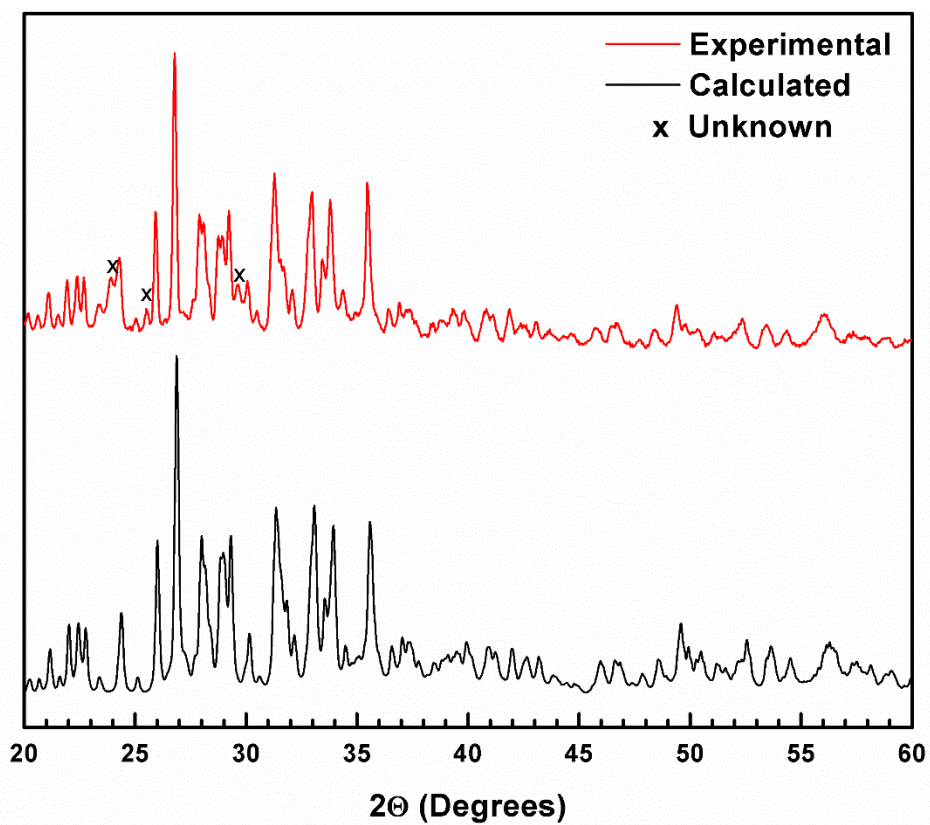Figure 8. Powder XRD of $Ba_6Ge_2Se_{12}$ after annealing.

Table 8. Crystallographic parameters of $Ba_6Ge_2Se_{12}$.

Refined Formula	$Ba_6Ge_2Se_{12}$
Crystal System	Monoclinic
Molecular Weight (g mol^{-1})	1916.74
Space group	$P2_1/c$ (no. 14)
a (Å)	10.0903(2)
b (Å)	9.3640(2)
c (Å)	25.7643(5)
β (º)	90.3030(10)
Unit cell volume (Å^3)	2434.32
Formula units per unit cell, Z	4
Density (g mol^{-1})	5.230
Radiation, wavelength (Å)	Mo Kα 0.71073
Temperature (K)	296
F(000)	3232
Absorption coefficient, μ (mm^{-1})	29.902
R_1	0.037
wR_2	0.056
Goodness of fit, GOF	1.05

Table 9. Atomic coordinates and displacement parameters of $Ba_6Ge_2Se_{12}$.

Atom	Wyckoff Position	x	y	z	U_{eq}	Occupancy
Ba1	4e	0.48140(4)	0.70645(5)	0.04817(2)	0.02302(9)	1
Ba2	4e	0.02453(4)	0.70621(5)	0.04805(2)	0.02148(9)	1
Ba3	4e	0.74806(4)	0.80652(4)	-0.09424(2)	0.02228(8)	1
Ba4	4e	0.75225(4)	1.06079(5)	0.12675(2)	0.02335(9)	1
Ba5	4e	0.54251(4)	0.59335(4)	0.22036(2)	0.01968(8)	1
Ba6	4e	0.00682(4)	0.50997(4)	0.21290(2)	0.01880(8)	1
Ge1	4e	0.25143(7)	0.83037(7)	0.17799(2)	0.01312(1)	1
Ge2	4e	0.75178(7)	0.46356(7)	0.08076(2)	0.01298(1)	1
Se1	4e	0.73405(7)	0.30194(7)	0.23181(2)	0.01911(1)	1
Se2	4e	0.25812(7)	0.61017(7)	0.13479(2)	0.01844(1)	1
Se3	4e	0.43944(6)	0.95382(8)	0.14898(3)	0.02043(1)	1
Se4	4e	0.55585(7)	0.34530(8)	0.09936(3)	0.02906(2)	1
Se5	4e	0.76377(7)	0.67263(7)	0.12993(2)	0.01765(1)	1
Se6	4e	0.05369(7)	0.94250(8)	0.15352(3)	0.02302(2)	1
Se7	4e	-0.05260(7)	0.33640(8)	0.09477(3)	0.02179(1)	1

Se8	4e	0.25264(7)	0.46981(7)	0.00739(2)	0.01957(1)	1
Se9	4e	0.82156(6)	0.71632(7)	0.28355(2)	0.01574(1)	1
Se10	4e	0.70160(7)	0.89454(7)	0.23806(3)	0.01951(1)	1
Se11A	4e	0.63186(2)	0.99159(1)	0.00803(4)	0.0615(5)	0.787(3)
Se11B	4e	0.2470(3)	1.1053(3)	-0.03082(14)	0.0233(9)	0.213(3)
Se12A	4e	0.86722(2)	0.98618(1)	0.00447(5)	0.0593(5)	0.781(3)
Se12B	4e	0.7482(4)	1.1085(4)	-0.0152(2)	0.0458(1)	0.219(3)

Table 10. Selected interatomic distances (Å) of $Ba_6Ge_2Se_{12}$

Ge1-Se3	2.3471(9)	Se9-Se10	2.3683(9)
Ge2-Se4	2.3183(1)		
Ge2-Se7	2.3317(9)	Se11-Se12	2.378(3)
Ge2-Se5	2.3346(9)	Se11-Se11	2.695(4)
Ge2-Se8	2.3556(8)	Se12-Se11	2.703(4)

3.1.3 $Ba_8Sn_4Se_{17}$

$Ba_8Sn_4Se_{17}$ was prepared through high-temperature solid-state synthesis by adding stoichiometric amounts of Ba (99.7%), Sn (99.99%), and Se (99.99%) into a glassy carbon crucible in a silica tube and evacuating the tube to 2.5×10^{-3} mbar before flame sealing the silica tube. The sample of $Ba_8Sn_4Se_{17}$ was heated along with samples of $Ba_7Ge_2Se_{17}$ and $Ba_6Ge_2Se_{12}$ so the same heating profile was used. After cooling to room temperature and analyzing the powder XRD pattern the orange powder already contained the target phase. The orange powder was placed in a new tube and annealed at 773 K for one month to eliminate the competing product of Ba_2SnSe_4. Due to the extremely large unit cell of $Ba_8Sn_4Se_{17}$, there are thousands of peaks in the simulated powder diagram. No major peaks from any side products stand out.

$Ba_8Sn_4Se_{17}$ may be written as $(Ba^{2+})_8(SnSe_4^{4-})_3(SnSe_5^{4-})$. This compound requires extensive annealing to form due to the competing reaction of Ba_2SnSe_4 ($Ba_{8/4}Sn_{4/4}Se_{16/4}$) which

forms initially due to the similar stoichiometries. After homogenizing and annealing for one month the slight excess of Se eventually diffuses throughout the sample and forms $Ba_8Sn_4Se_{17}$. $Ba_8Sn_4Se_{17}$ crystallizes in the monoclinic $C2/c$ space group with the extremely large unit cell parameters $a = 47.2887(2)$ Å, $b = 12.6224(5)$ Å, $c = 25.7173(1)$ Å, and $\beta = 104.729(1)$ º.
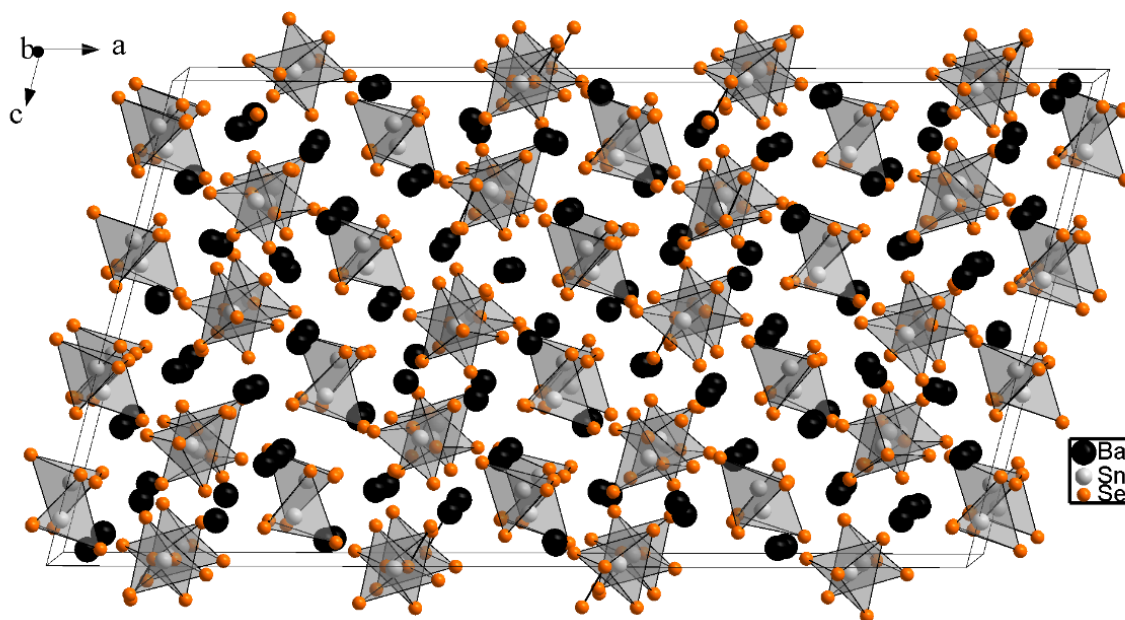
Figure 9. The complex crystal structure of $Ba_8Sn_4Se_{17}$ highlighting the $[SnSe_4]^{4-}$ and $[SnSe_5]^{4-}$ tetrahedra.
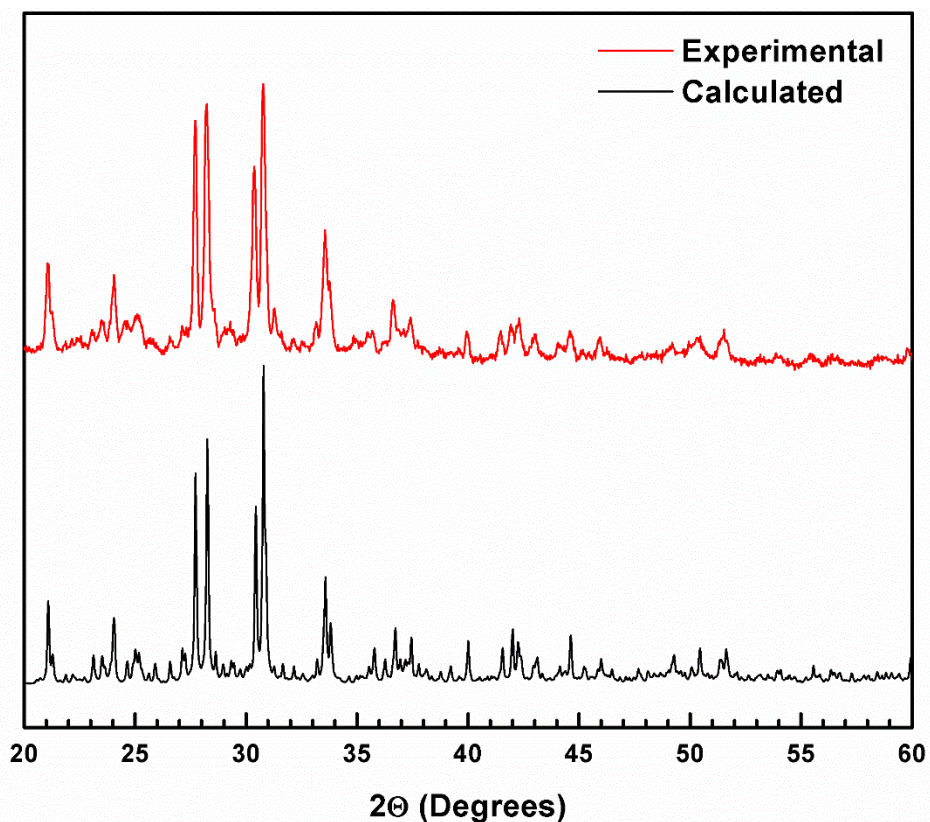
Figure 10. Powder XRD of $Ba_8Sn_4Se_{17}$ after annealing.

Table 11. Crystallographic parameters of $Ba_8Sn_4Se_{17}$.

Refined Formula	$Ba_8Sn_4Se_{17}$
Crystal System	Monoclinic
Molecular Weight (g mol^{-1})	2915.8
Space group	$C2/c$ (no. 15)
a (Å)	47.2887(2)
b (Å)	12.6224(5)
c (Å)	25.7173(1)
β (º)	104.7290(1)
Unit cell volume (Å^3)	14846.1
Formula units per unit cell, Z	16
Density (g mol^{-1})	5.218
Radiation, wavelength (Å)	Mo Kα 0.71073
Temperature (K)	273
F(000)	19616
Absorption coefficient, μ (mm^{-1})	27.645
R_1	0.100

wR$_2$	0.119
Goodness of fit, GOF	1.13

Table 12. Atomic coordinates and displacement parameters of Ba$_8$Sn$_4$Se$_{17}$.

Atom	Wyckoff Position	x	y	z	U$_{eq}$	Occupancy
Ba1	8f	0.0395(1)	0.2360(1)	0.2201(1)	0.020(1)	1
Ba2	8f	0.0841(1)	0.00001(7)	0.5984(1)	0.019(1)	1
Ba3	8f	0.1634(1)	0.2455(1)	0.1464(1)	0.018(1)	1
Ba4	8f	0.4193(1)	0.0170(1)	0.1546(1)	0.017(1)	1
Ba5	8f	0.2098(1)	0.0077(1)	0.2910(1)	0.016(1)	1
Ba6	8f	0.0845(1)	0.4780(1)	0.1099(1)	0.024(1)	1
Ba7	8f	0.4583(1)	0.2562(1)	0.0451(1)	0.017(1)	1
Ba8	8f	0.2132(1)	0.4548(1)	0.2868(1)	0.020(1)	1
Ba9	8f	0.0846(1)	0.0187(1)	0.3662(1)	0.020(1)	1
Ba10	8f	0.2098(1)	0.4708(1)	0.0300(1)	0.021(1)	1
Ba11	8f	0.1681(1)	0.2268(1)	0.4126(1)	0.019(1)	1
Ba12	8f	0.0357(1)	0.2959(1)	0.4751(1)	0.020(1)	1
Ba13	8f	0.3330(1)	0.2315(1)	0.3492(1)	0.020(1)	1
Ba14	8f	0.2109(1)	0.0126(1)	0.0390(1)	0.020(1)	1
Ba15	8f	0.3355(1)	0.2247(1)	0.1254(1)	0.024(1)	1
Ba16	8f	0.4593(1)	0.2821(1)	0.2849(1)	0.035(1)	1
Sn1	8f	0.2517(1)	0.2378(1)	0.4043(1)	0.015(1)	1
Sn2	8f	0.5042(1)	0.0154(1)	0.1563(1)	0.016(1)	1
Sn3	8f	0.1270(1)	0.2985(1)	0.2702(1)	0.015(1)	1
Sn4	8f	0.0023(1)	0.0249(1)	0.4060(1)	0.018(1)	1
Sn5	8f	0.3781(1)	0.0382(1)	0.5061(1)	0.014(1)	1
Sn6	8f	0.2515(1)	0.2311(1)	0.1561(1)	0.016(1)	1
Sn7	8f	0.3766(1)	0.4314(1)	0.2501(1)	0.019(1)	1
Sn8	8f	0.3714(1)	0.3283(1)	0.01564(1)	0.016(1)	1
Se1	8f	0.3512(1)	0.0008(1)	0.3018(1)	0.018(1)	1
Se2	8f	0.1409(1)	0.4965(1)	0.2868(1)	0.018(1)	1
Se3	8f	0.4027(1)	0.2367(1)	0.4238(1)	0.034(1)	1
Se4	8f	0.1105(1)	0.2631(1)	0.4928(1)	0.035(1)	1
Se5	8f	0.4304(1)	0.0214(1)	0.0278(1)	0.016(1)	1
Se6	8f	0.0285(1)	0.1817(1)	0.0813(1)	0.018(1)	1
Se7	8f	0.2232(1)	0.4010(1)	0.4174(1)	0.019(1)	1
Se8	8f	0.4755(1)	0.1763(1)	0.1729(1)	0.019(1)	1
Se9	8f	0.3485(1)	0.4831(1)	0.3181(1)	0.020(1)	1
Se10	8f	0.2238(1)	0.3990(1)	0.1648(1)	0.019(1)	1
Se11	8f	0.0535(1)	0.0264(1)	0.4662(1)	0.018(1)	1
Se12	8f	0.2209(1)	0.0729(1)	0.1684(1)	0.018(1)	1

Se13	8f	0.1784(1)	0.2340(1)	0.2856(1)	0.017(1)	1
Se14	8f	0.0984(1)	0.2615(1)	0.3383(1)	0.017(1)	1
Se15	8f	0.3044(1)	0.2463(1)	0.4578(1)	0.020(1)	1
Se16	8f	0.1019(1)	0.2237(1)	0.0526(1)	0.018(1)	1
Se17	8f	0.1799(1)	0.2402(1)	0.0111(1)	0.022(1)	1
Se18	8f	0.2568(1)	0.2285(1)	0.3103(1)	0.021(1)	1
Se19	8f	0.2252(1)	0.0717(1)	0.4230(1)	0.018(1)	1
Se20	8f	0.1496(1)	0.4866(1)	0.4237(1)	0.017(1)	1
Se21	8f	0.3020(1)	0.2300(1)	0.2185(1)	0.019(1)	1
Se22	8f	0.0989(1)	0.2563(1)	0.1778(1)	0.018(1)	1
Se23	8f	0.4443(1)	0.0072(1)	0.2856(1)	0.021(1)	1
Se24	8f	0.0724(1)	0.0067(1)	0.2308(1)	0.020(1)	1
Se25	8f	0.0246(1)	0.1467(1)	0.5868(1)	0.019(1)	1
Se26	8f	0.1533(1)	0.4917(1)	0.0841(1)	0.018(1)	1
Se27	8f	0.4022(1)	0.2684(1)	0.1066(1)	0.017(1)	1
Se28	8f	0.3482(1)	0.4771(1)	0.1558(1)	0.020(1)	1
Se29	8f	0.5106(1)	0.0302(1)	0.0628(1)	0.023(1)	1
Se30	8f	0.0246(1)	0.3490(1)	0.3377(1)	0.017(1)	1
Se31	8f	0.0112(1)	0.0285(2)	0.3136(1)	0.038(1)	1
Se32	8f	0.2612(1)	0.2256(1)	0.0648(1)	0.032(1)	1
Se33	8f	0.3864(1)	0.2378(1)	0.2603(1)	0.042(1)	1
Se34	8f	0.1373(1)	0.0254(1)	0.4866(1)	0.035(1)	1

Table 13. Selected interatomic distances (Å) for $Ba_8Sn_4Se_{17}$.

Sn1-Se18	2.4926(2)	Sn5-Se26	2.4873(2)
Sn1-Se15	2.5227(2)	Sn5-Se20	2.5072(2)
Sn1-Se7	2.5312(2)	Sn5-Se5	2.5075(2)
Sn1-Se19	2.5498(2)	Sn5-Se4	2.5643(2)
Sn2-Se29	2.5051(2)	Sn6-Se32	2.5048(2)
Sn2-Se23	2.5149(2)	Sn6-Se21	2.5154(2)
Sn2-Se30	2.5298(2)	Sn6-Se10	2.5311(2)
Sn2-Se8	2.5388(2)	Sn6-Se12	2.5328(2)
Sn3-Se22	2.4692(2)	Sn7-Se33	2.4891(2)
Sn3-Se13	2.4947(2)	Sn7-Se24	2.5230(2)
Sn3-Se14	2.5144(2)	Sn7-Se28	2.5240(2)
Sn3-Se2	2.5916(2)	Sn7-Se9	2.5375(2)
Sn4-Se31	2.5186(2)	Sn8-Se16	2.4974(2)
Sn4-Se11	2.5210(2)	Sn8-Se17	2.5005(2)
Sn4-Se6	2.5267(2)	Sn8-Se34	2.5207(2)

Sn4-Se25	2.5424(17)	Sn8-Se27	2.5353(16)
Se1-Se2	2.4006(18)		
Se4-Se3	2.381(3)		

3.1.4 γ-Sr$_2$GeSe$_4$

These NCS compounds may be written with the general formula Sr$_{2-x}$Pb$_x$GeSe$_4$. The crystal structures for the phases with x = 0 and 0.69 are known. γ–Sr$_2$GeSe$_4$ (x = 0) was first reported by Johrendt et al., however, this paper mainly discussed the crystal structures of γ–Sr$_2$GeSe$_4$ and Eu$_2$GeSe$_4$.[53] This left open the opportunity to study the optical properties of γ–Sr$_2$GeSe$_4$ and conveniently gave the instructions to synthesize γ–Sr$_2$GeSe$_4$. Unfortunately, γ–Sr$_2$GeSe$_4$ is difficult to make in high purity due to it melting incongruently and the fact that annealing the sample converts it from the red γ–Sr$_2$GeSe$_4$ to the yellow α–Sr$_2$GeSe$_4$. Since the tetrahedra in γ–Sr$_2$GeSe$_4$ are aligned cooperatively this should enhance the polarizability thus increasing the SHG response.

γ–Sr$_2$GeSe$_4$ was prepared using two methods. The first was following the method outlined by Johrendt et al. and the second was developed during this work.[53] The original method involved preparing the binary Sr$_2$Ge first and then mixing this with Se to prepare γ–Sr$_2$GeSe$_4$. Stoichiometric amounts of Sr (99%) and Ge (99.999%) were added to glassy carbon crucibles and heated to 1173 K for 12 hours to produce the dark grey Sr$_2$Ge product. This germanide was extremely air-sensitive and had to be ground and stored in the Ar filled glove box. The Sr$_2$Ge was added with elemental Se (99.99%) in a 1:4 stoichiometric ratio to a glassy carbon crucible. The crucible was placed at the bottom of a silica tube and evacuated to 2.5×10^{-3} mbar and flame sealed. This sealed tube was placed into a preheated manual furnace at 1173 K for two hours and quenched in an ice bath. This is the same approach that led to red crystals of γ–Sr$_2$GeSe$_4$

mentioned in the paper first describing γ–Sr_2GeSe_4, but this is not a good method to make γ–Sr_2GeSe_4 in bulk.

The original synthesis required the preparation of the air-sensitive binary Sr_2Ge and involved a hazardous step of putting an ampoule with unreacted Se into a preheated furnace well above the boiling point of Se (BP = 958 K). To improve on the methodology and prepare bulk γ–Sr_2GeSe_4 in relatively high purity for SHG measurements, the following procedure was developed. Stoichiometric amounts of Sr (99%), Ge (99.999%), and Se (99.99%) were added to a glassy carbon crucible and placed at the bottom of a silica tube to be evacuated to 2.5×10^{-3} mbar and flame sealed. This ampoule was slowly heated at a rate of 100 K per hour to 1073 K. After the elements had reacted the temperature was decreased to 923 K and held for 100 hours to allow the elements to diffuse through the sample. The sample was finally slow cooled to 473 K over 100 hours. This resulted in bulk γ–Sr_2GeSe_4 that was not full of the binaries SrSe and $GeSe_2$ or that contained significant amounts of the NCS α–Sr_2GeSe_4. The comparison between the two methods of preparing γ–Sr_2GeSe_4 are shown in Figure 11.
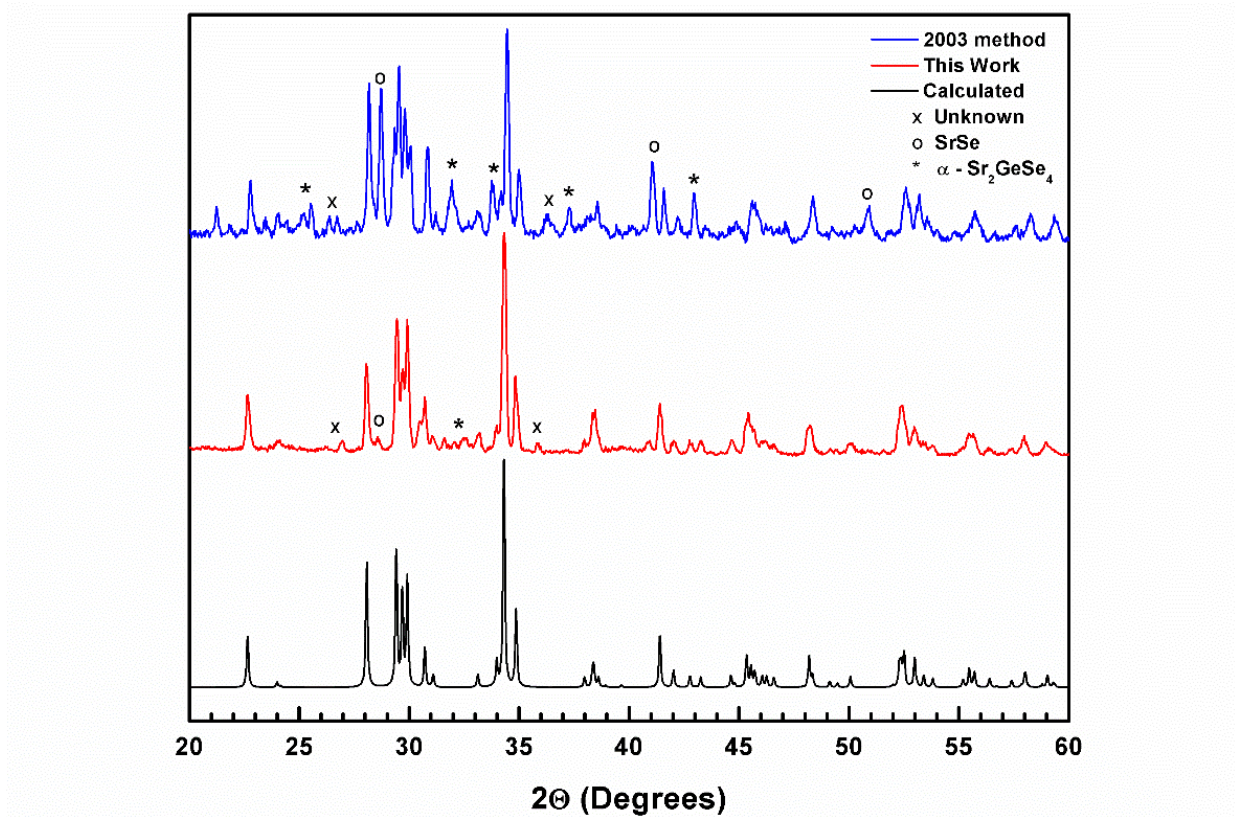
Figure 11. Comparison of the powder XRD patterns of γ–Sr_2GeSe_4 using different synthesis methods.

3.1.5 $Sr_{1.31}Pb_{0.69}GeSe_4$

$Sr_{1.31}Pb_{0.69}GeSe_4$ was the refined formula of the new compound that single-crystal XRD was performed on while looking for a single crystal of $Sr_{19-x}Pb_xGe_{11}Se_{44}$ by Dr. Abdeljalil Assoud.[60] The nominal formula was rounded to x = 0.7 for the characterization of physical properties. Preparing $Sr_{1.3}Pb_{0.7}GeSe_4$ (x = 0.7) is far easier than γ-Sr_2GeSe_4. The larger Pb^{2+} atoms stabilize the γ–Sr_2GeSe_4 structure type allowing this phase to be annealed and made pure. $Sr_{1.3}Pb_{0.7}GeSe_4$ was prepared by combining stoichiometric amounts of the starting elements Sr (99%), Pb (99.99%), Ge (99.999%), and Se (99.99%) into glassy carbon crucibles at the bottom of evacuated and sealed silica tubes. The sample of $Sr_{1.3}Pb_{0.7}GeSe_4$ was prepared alongside γ–

46

Sr_2GeSe_4 so it was placed in a preheated furnace at 1173 K for two hours and quenched in an ice bath. The sample was then homogenized, and the dark brown powder was resealed in a silica tube to be annealed at 773 K for one week. The slower approach developed in this work was not attempted to synthesize $Sr_{1.3}Pb_{0.7}GeSe_4$ since the initial procedure along with grinding and annealing was satisfactory. The powder XRD diagram of the annealed $Sr_{1.3}Pb_{0.7}GeSe_4$ sample and the calculated powder diagram from the crystal structure of $Sr_{1.31}Pb_{0.69}GeSe_4$ are compared in Figure 13.
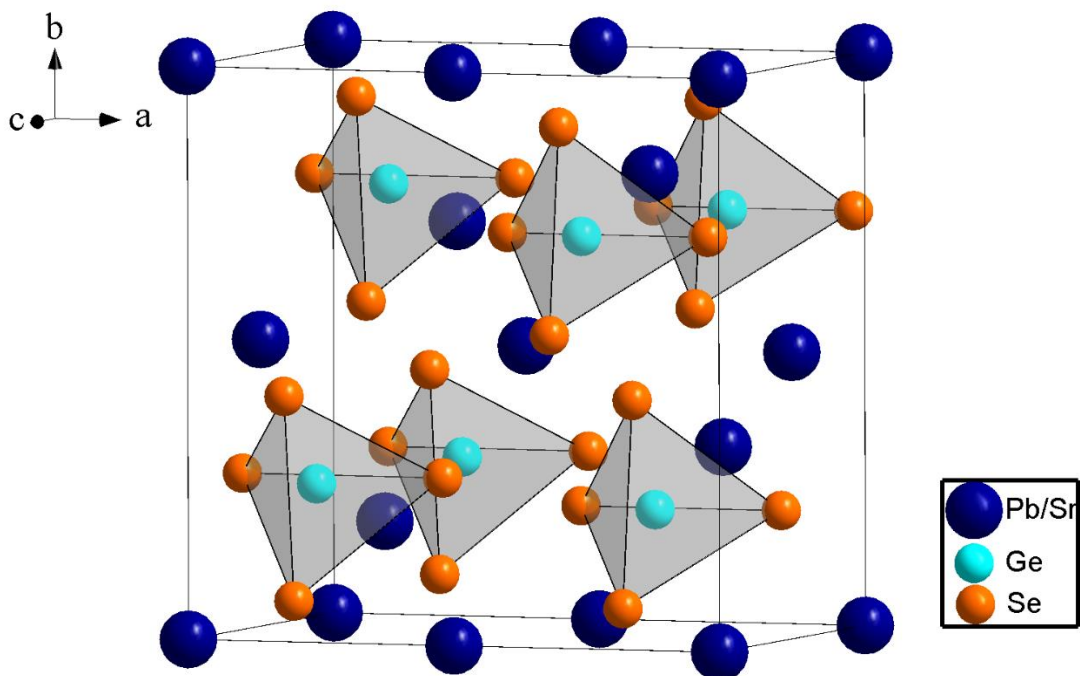
Figure 12. The structure of $Sr_{1.31}Pb_{0.69}GeSe_4$ highlighting the $[GeSe_4]^{4-}$ tetrahedra. All Sr/Pb sites have mixed occupancies.

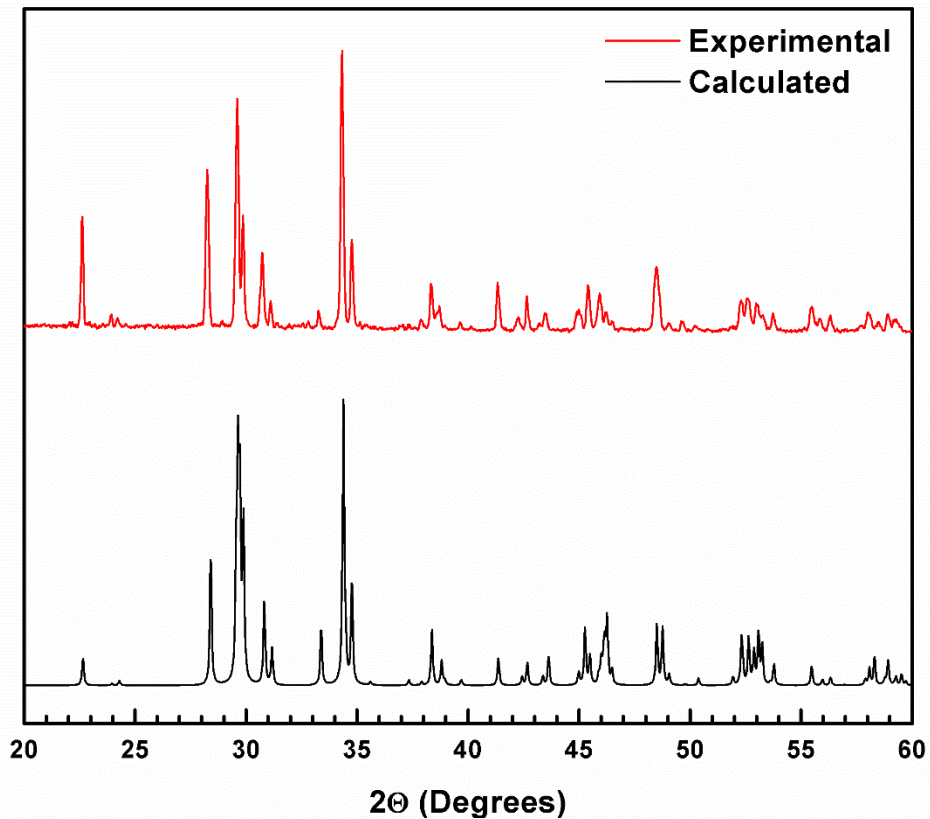Figure 13. Powder XRD patterns of annealed $Sr_{1.3}Pb_{0.7}GeSe_4$ and the calculated pattern of $Sr_{1.31}Pb_{0.69}GeSe_4$.

Table 14. Crystallographic parameters of $Sr_{1.31}Pb_{0.69}GeSe_4$.

Refined Formula	$Sr_{1.31}Pb_{0.69}GeSe_4$
Crystal System	Orthorhombic
Molecular Weight (g mol^{-1})	696.8
Space group	*Ama*2 (no. 40)
a (Å)	10.31220(1)
b (Å)	10.39320(1)
c (Å)	7.42140(1)
Unit cell volume (Å^3)	795.402
Formula units per unit cell, Z	4
Density (g mol^{-1})	5.394
Radiation, wavelength (Å)	Mo Kα 0.71073
Temperature (K)	296
F(000)	795
Absorption coefficient, μ (mm^{-1})	45.236

R$_1$	0.016
wR$_2$	0.034
Goodness of fit, GOF	1.05

Table 15. Atomic coordinates and displacement parameters of Sr$_{1.31}$Pb$_{0.69}$GeSe$_4$.

Atom	Wyckoff Position	x	y	z	U$_{eq}$	Occupancy
Sr1/Pb1	4b	0.25	0.19137(3)	0.56141(4)	0.03079(1)	0.325(3)/0.675(3)
Sr2/Pb2	4a	0	0	0.00047(8)	0.03079(1)	0.013(2)/0.987(2)
Ge1	4b	0.25	0.27870(5)	0.02988(7)	0.02147(2)	1
Se1	8c	0.56149(3)	0.21545(4)	0.35130(5)	0.02147(2)	1
Se2	4b	0.25	0.08106(5)	0.18616(7)	0.01834(1)	1
Se3	4b	0.25	0.44131(6)	0.25196(8)	0.01597(1)	1

Table 16. Selected interatomic distances (Å) of Sr$_{1.31}$Pb$_{0.69}$GeSe$_4$.

Ge1-Se1	2.3535(5)
Ge1-Se2	2.3589(8)
Ge1-Se3	2.3606(8)

3.1.6 Sr$_{0.21}$Pb$_{1.79}$GeSe$_4$ and Pb$_2$GeSe$_4$

When the phase width of Sr$_{2-x}$Pb$_x$GeSe$_4$ was being determined, attempts to recreate

Pb$_2$GeSe$_4$ did not go as expected. From powder X-ray diffraction (XRD) patterns it was observed

that Sr$_{0.25}$Pb$_{1.75}$GeSe$_4$ and Pb$_2$GeSe$_4$ (x = 1.75, 2) were not being made with the monoclinic

structure. The monoclinic β-Pb$_2$GeSe$_4$ is isostructural with the low-temperature structure of the

analogous sulphide, β-Pb$_2$GeS$_4$.[61] All attempts to make Sr$_{0.25}$Pb$_{1.75}$GeSe$_4$ and Pb$_2$GeSe$_4$ would

result in these two phases adopting the high-temperature α-Pb$_2$GeS$_4$ structure type.[63] Unlike the

low-temperature structure which has the $P2_1/c$ space group symmetry, the high-temperature

structure crystallizes in the cubic $I\bar{4}3d$ space group. Conveniently, this means these two phases

can be made NCS and can, therefore, exhibit SHG. $Sr_{0.25}Pb_{1.75}GeSe_4$ was first predicted by

Kanatzidis et al. to exist after reporting that the monovalent cations Na^+ and Ag^+ could be

substituted into the α-Pb_2GeS_4 and α-Pb_2GeSe_4 structures due to partially occupied Pb sites in the

structure.[69]

The α-Pb_2GeS_4 structure type is an extremely robust crystal structure and is capable of

several substitutions. Many compounds adopting this crystal structure have been reported and

some have had their NLO properties reported as well.[48,63,69–73] Although there is a large variety

of compounds which adopt this structure type their cubic crystal structure limits their NLO

performance. As a result, they are unable to phase-match. Despite this drawback, this enables a

much more interesting study of the NLO properties of $Sr_{2-x}Pb_xGeSe$ (x = 0, 0.7, 1.75, 2). The

effects of Pb^{2+} substitution can be determined in the two different crystal structures and then

comparisons may be drawn between the two crystal structures.
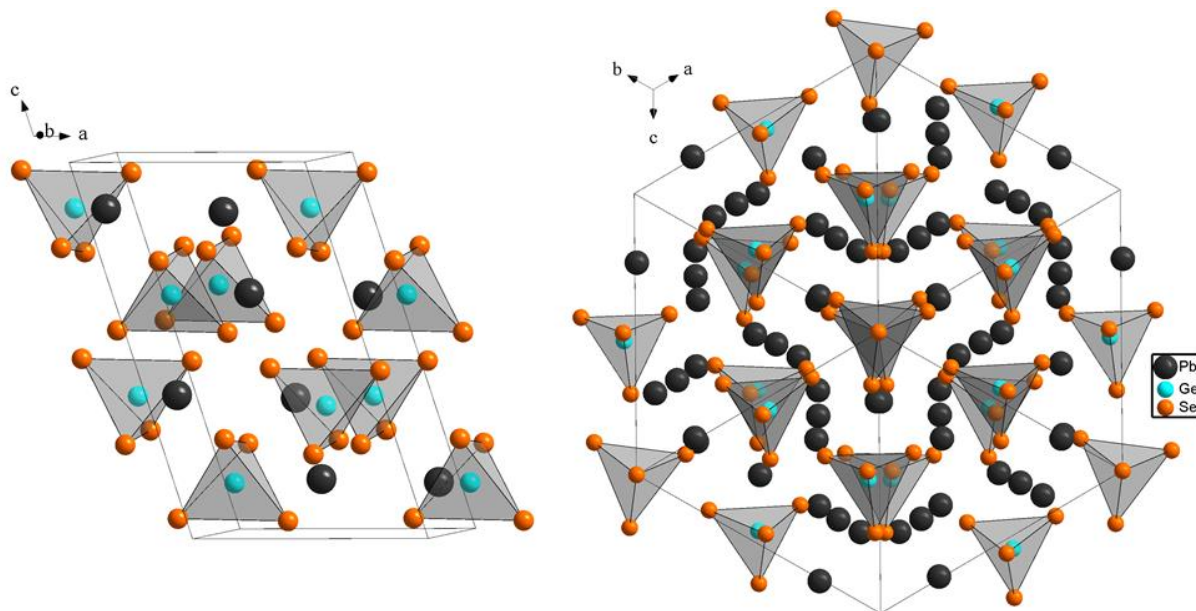
Figure 14. Crystal structures of the low-temperature Pb_2GeSe_4 structure (left) and the high-

temperature structure (right).

$Sr_{0.25}Pb_{1.75}GeSe_4$ and Pb_2GeSe_4 were made by combining stoichiometric amounts of Sr (99.99%), Pb (99.99%), Ge (99.999%), and Se (99.99%) into silica tubes. The tubes were evacuated to 2.5×10^{-3} mbar and flame sealed. The tubes were heated to 1173 K to achieve a melt and quenched in an ice bath. From powder XRD the target cubic phase was present after the quench but to remove the side products of PbSe and $GeSe_2$ the sample was homogenized and annealed at 773 K for one week. After annealing only nominal amounts of PbSe and $GeSe_2$ were visible in the powder XRD pattern.
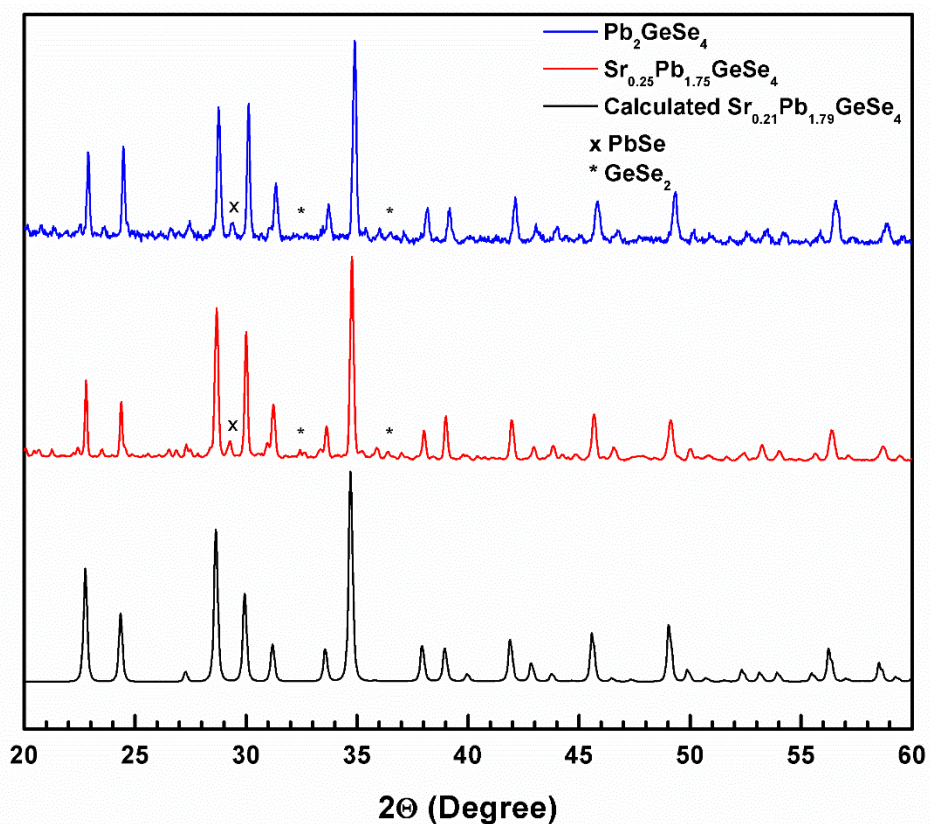
Figure 15. Powder XRD patterns of annealed $Sr_{0.25}Pb_{1.75}GeSe_4$, α–Pb_2GeSe_4, and the calculated pattern of the $Sr_{0.21}Pb_{1.79}GeSe_4$. Side products of PbSe and $GeSe_2$ are highlighted.

$Sr_{0.25}Pb_{1.75}GeSe_4$ and Pb_2GeSe_4 were the two compounds in which the crystal structures were not known yet. After annealing the sample of $Sr_{0.25}Pb_{1.75}GeSe_4$ at 773 K a black crystal was

picked that was suitable for single-crystal XRD. The formula of this crystal was refined to be $Sr_{0.21}Pb_{1.79}GeSe_4$ with $a = 14.6177(3)$ Å. Although the lattice parameters of α–Pb_2GeSe_4 have been reported before to be $a = 14.573$ Å, a high-quality crystal structure of the cubic α–Pb_2GeSe_4 was still missing.[63] To complement the monoclinic β–Pb_2GeSe_4 crystal structure crystals of α–Pb_2GeSe_4 were grown using a metal flux. Fluxes of Zn and Cd were attempted since they had been used with other selenogemanates.[41] A large excess of Zn and Cd was not used for this crystal growth. Pb, Ge, Se, and Zn/Cd were added to silica tubes in a 2:1:4:1 molar ratio. The small addition of Zn flux worked particularly well and gave large, nicely faceted black crystals as seen in Figure 16. Unfortunately, despite having a nice appearance these data collected from a crystal from this sample still could not be refined to give small R_1 and wR_2 values.

Figure 16. Light microscope image of α–Pb_2GeSe_4 crystals grown using a Zn flux.

Table 17. Crystallographic parameters of $Sr_{0.21}Pb_{1.79}GeSe_4$ and β–Pb_2GeSe_4

Refined Formula	$Sr_{0.21}Pb_{1.79}GeSe_4$	β–Pb_2GeSe_4
Crystal System	Cubic	Monoclinic
Molecular Weight (g mol^{-1})	777.25	802.81
Space group	$I\bar{4}3d$ (no. 220)	$P2_1/c$ (no. 14)
a (Å)	14.6177(3)	8.4447(3)
b (Å)	14.6177(3)	7.1314(3)
c (Å)	14.6177(3)	13.8079(4)
β (º)	90	107.867(2)
Unit cell volume (Å^3)	3123.5	791.44
Formula units per unit cell, Z	16	4
Density (g mol^{-1})	6.611	6.738
Radiation, wavelength (Å)	Mo Kα 0.71073	Mo Kα 0.71073
Temperature (K)	296	293
F(000)	5162	1328
Absorption coefficient, μ (mm^{-1})	62.23	64.5
R_1	0.035	0.042
wR_2	0.077	0.052
Goodness of fit, GOF	1.37	1.07

Table 18. Atomic coordinates and displacement parameters of $Sr_{0.21}Pb_{1.79}GeSe_4$.

Atom	Wyckoff Position	x	y	z	U_{eq}	Occupancy
Sr1/Pb1	24d	0.0084(1)	0	0.25	0.0431(3)	0.070(1)/0.930(1)
Sr2/Pb2	24d	0.3294(2)	0	0.25	0.0431(3)	0.073(7)/0.261(7)
Ge1	16c	0.2265(1)	0.2265(1)	0.2265(1)	0.0398(1)	1
Se1	16c	0.0703(1)	0.0703(1)	0.0703(1)	0.0398(1)	1
Se2	48e	0.1234(1)	0.3259(1)	0.1533(1)	0.0170(4)	1

Table 19. Selected interatomic distances (Å) of $Sr_{0.21}Pb_{1.79}GeSe_4$.

Ge1-Se1	2.374(3)
Ge1-Se2	2.3511(1)

Table 20. Atomic coordinates and displacement parameters of β–Pb$_2$GeSe$_4$.

Atom	Wyckoff Position	x	y	z	U_{eq}	Occupancy
Pb1	4e	0.05889(3)	0.34874(4)	0.37255(2)	0.02113(8)	1
Pb2	4e	0.55573(3)	0.36214(4)	0.36453(2)	0.02224(8)	1
Ge1	4e	0.19817(8)	0.26720(9)	0.14119(4)	0.01314(1)	1
Se1	4e	0.08542(8)	0.73930(1)	0.45250(4)	0.01826(1)	1
Se2	4e	0.25156(9)	0.54153(9)	0.23895(4)	0.01670(1)	1
Se3	4e	0.26794(9)	0.02556(9)	0.26381(4)	0.01624(2)	1
Se4	4e	0.37828(8)	0.23879(1)	0.04062(4)	0.01857(1)	1

Table 21. Selected interatomic distances (Å) of Sr$_{0.21}$Pb$_{1.79}$GeSe$_4$.

Ge1-Se1	2.3553(9)
Ge1-Se2	2.3408(9)
Ge1-Se3	2.3604(8)
Ge1-Se4	2.3619(9)

3.1.7 BaCuSiTe$_3$

BaCuSiTe$_3$ is a new NCS compound which contains the large anionic [Si$_2$Te$_6$]$^{6-}$ which should lead to large NLO susceptibilities. With all the NCS compounds both theoretical calculations and experimental measurements will be performed to determine their NLO properties.

BaCuSiTe$_3$ samples were prepared by adding stoichiometric amounts of Ba (99.7%), Cu (99.5%), Si (99.9%), and Te (99.99%) to a glassy carbon crucible and placing the crucible at the bottom of a silica tube. The tube was evacuated to 2.5×10^{-3} mbar and flame sealed. The sealed tubes were heated to 973 K within 10 hours, held at this temperature for 2 hours and slowly cooled back to room temperature over the course of 100 hours. This produced an almost black powder which contained several red crystals suitable for single-crystal XRD. The sealed sample

was opened and ground to be annealed at 773 K for one week. The powder XRD pattern appeared to contain an amorphous phase due to the broad background. This was attributed to the poor crystallinity which has been observed in other silicides.[74]
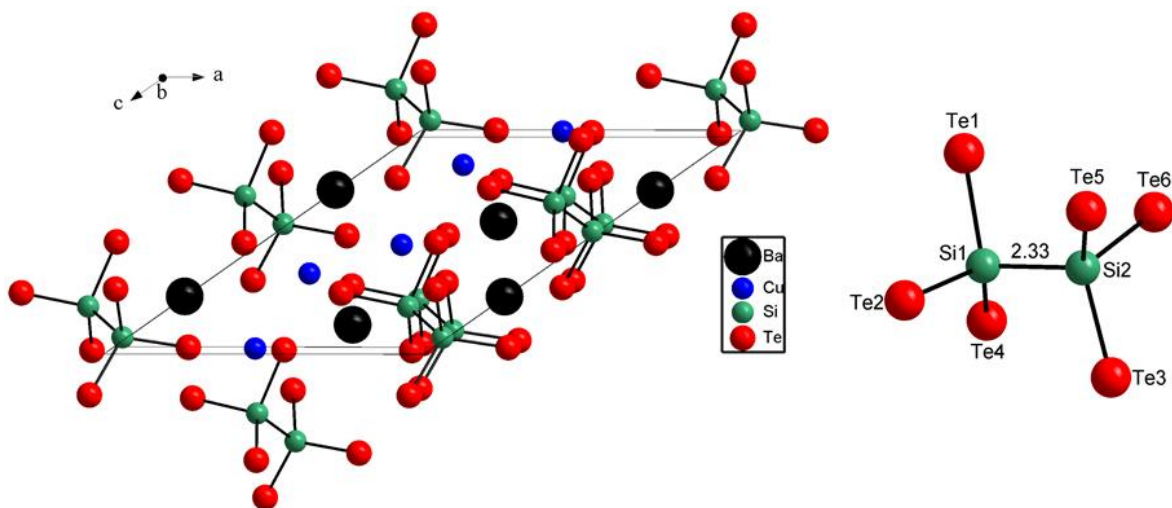

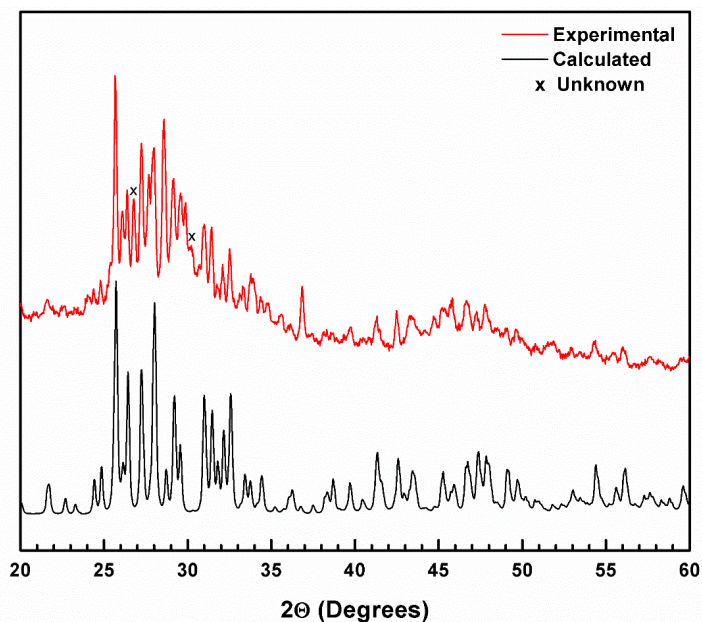Figure 17. Crystal structures of BaCuSiTe$_3$ (left) and the ethane-like $[Si_2Te_6]^{6-}$ in the staggered conformation(right)

Figure 18. Powder XRD patterns of annealed BaCuSiTe$_3$ with a broad background.

Table 22. Crystallographic parameters of BaCuSiTe₃.

Refined Formula	$BaCuSiTe_3$
Crystal System	Monoclinic
Molecular Weight (g mol^{-1})	611.77
Space group	Pc (no. 7)
a (Å)	7.5824(1)
b (Å)	8.8440(1)
c (Å)	13.1289(2)
β (º)	122.022(1)
Unit cell volume (Å^3)	746.45(2)
Formula units per unit cell, Z	4
Density (g mol^{-1})	5.444
Radiation, wavelength (Å)	Mo Kα 0.71073
Temperature (K)	293
F(000)	1020
Absorption coefficient, μ (mm^{-1})	19.62
R$_1$	0.015
wR$_2$	0.033
Goodness of fit, GOF	1.10

3.2 Band Gap Determination

To determine the band gaps of the compounds reported here diffuse reflectance

spectroscopy was used. The colours of these compounds range from orange to black, so their

band gaps are in the visible to the IR region. A PerkinElmer Lambda 1050 UV/VIS/NIR

Spectrometer was used since it has an InGaAs detector for measuring spectra in the IR region.

Spectra were collected over the entire range of the instrument, 300 nm – 2500 nm. At 860 nm the

detector of the spectrometer changes from InGaAs to a PMT. The ground samples were cold-

pressed into 12.7 mm diameter pellets with 30 kN of force. The percent reflectance spectra were

measured for all samples. The percent reflectance was converted to absorbance using the

Kubelka-Munk equation (2.10.1). It is necessary to determine the experimental band gaps of the

NCS compounds to correct the calculated bandgaps that are used in the calculation of the d-tensor elements.

3.2.1 Ba$_7$Ge$_2$Se$_{17}$, Ba$_6$Ge$_2$Se$_{12,}$ and Ba$_8$Sn$_4$Se$_{17}$

The Ba compounds Ba$_7$Ge$_2$Se$_{17}$, Ba$_6$Ge$_2$Se$_{12,}$ and Ba$_8$Sn$_4$Se$_{17}$ were black, brown, and orange respectively. Their respective band gaps as determined by spectroscopy are 1.51 eV, 1.75 eV, and 1.92 eV, respectively. This is in good agreement with their colours.
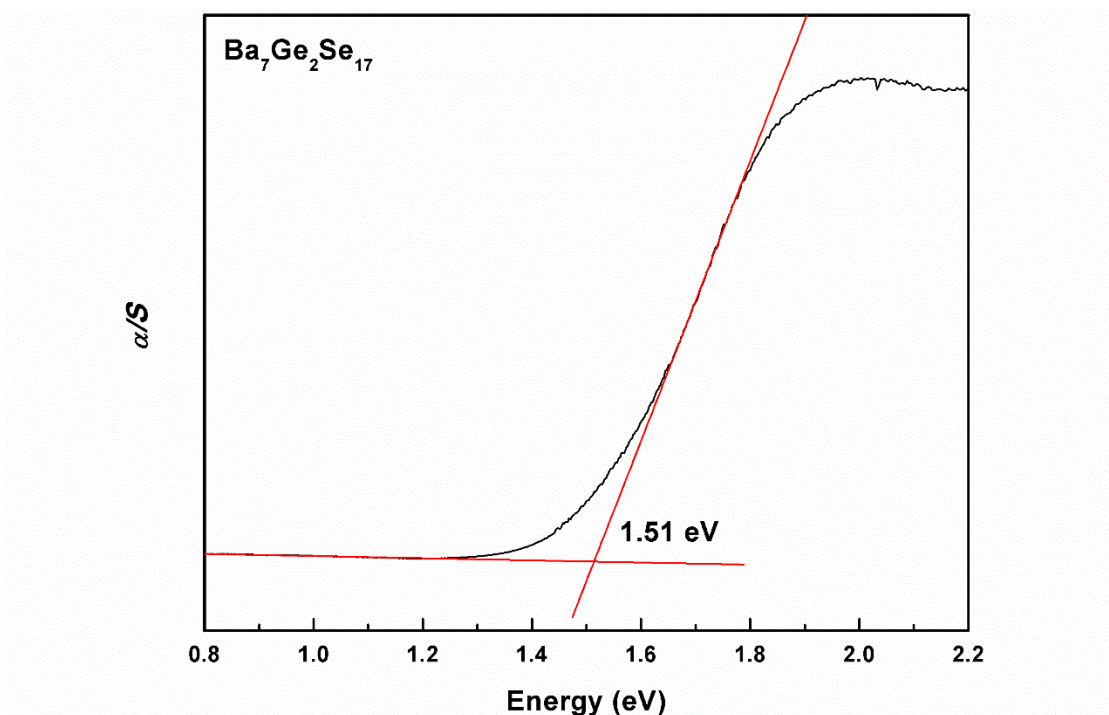

Figure 19. The absorption spectrum of Ba$_7$Ge$_2$Se$_{17}$.
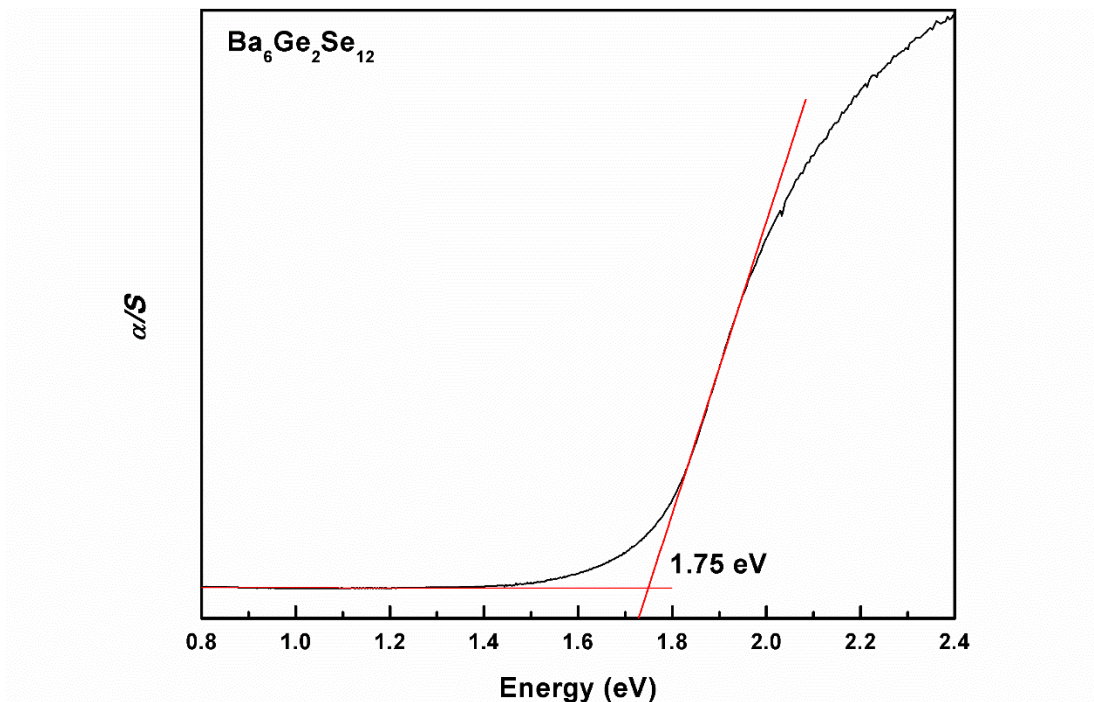
Figure 20. The absorption spectrum of $Ba_6Ge_2Se_{12}$.
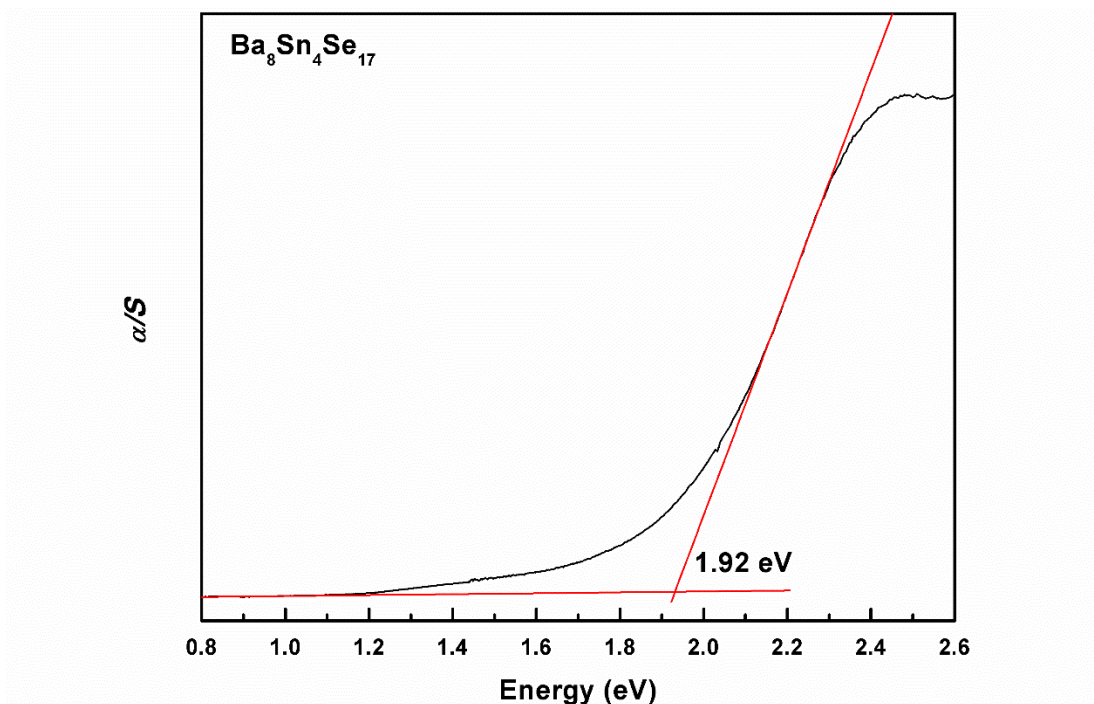
Figure 21. The absorption spectrum of $Ba_8Sn_4Se_{17}$.

3.2.2 $Sr_{2-x}Pb_xGeSe_4$ (x = 0, 0.7, 1.75, and 2)

The samples of γ–Sr_2GeSe_4, $Sr_{1.3}Pb_{0.7}GeSe_4$, $Sr_{0.25}Pb_{1.75}GeSe_4$, and α–Pb_2GeSe_4 were ground

into powders and cold-pressed into pellets. The diffuse reflectance spectra of these four

compounds were collected and converted to absorbance. The absorbance curve of γ–Sr_2GeSe_4

contained a noticeable artifact in the data where the detector changed from GaAs to the PMT.

The curve of γ–Sr_2GeSe_4 was also not as smooth as the other three compounds in the series due

to the small contributions from the side products present. The optical band gaps of γ–Sr_2GeSe_4,

$Sr_{1.3}Pb_{0.7}GeSe_4$, $Sr_{0.25}Pb_{1.75}GeSe_4$, and α–Pb_2GeSe_4 were determined to be 2.00 eV, 1.65 eV, 1.48

eV, and 1.42 eV respectively. The latter two phases have band gaps which are in good agreement

with the band gaps of the similar Na and Ag analogs, $Na_{0.5}Pb_{1.75}GeSe_4$ and $Ag_{0.5}Pb_{1.75}GeSe_4$.[69]

Since Pb is more electronegative than Sr the expected trend of decreasing the band gap by
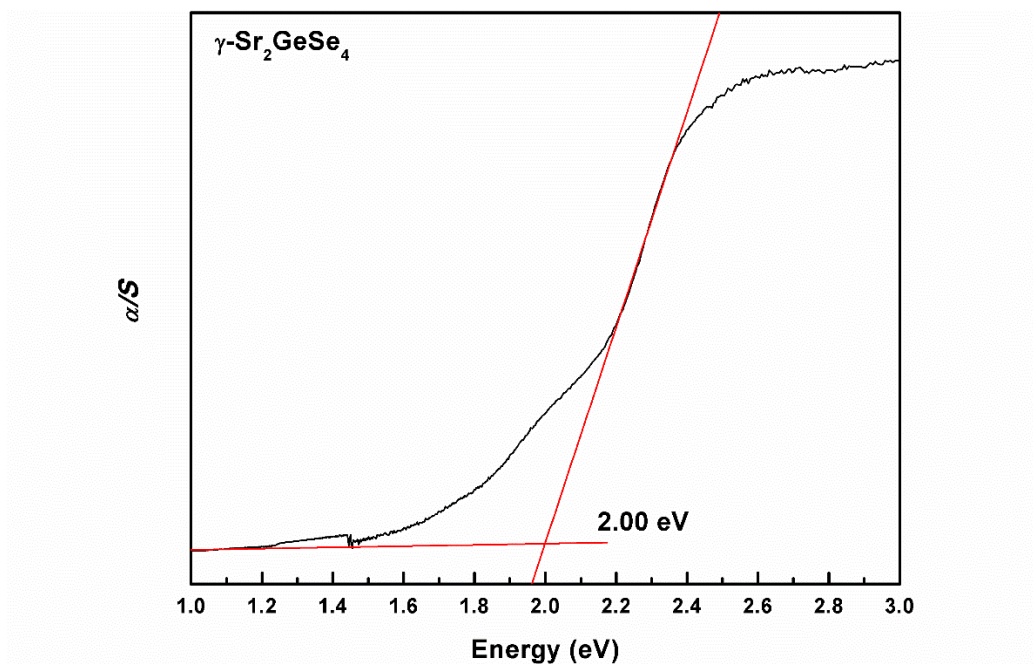
substituting more Pb into the compounds was observed.

Figure 22. The absorption spectrum of γ–Sr_2GeSe_4.

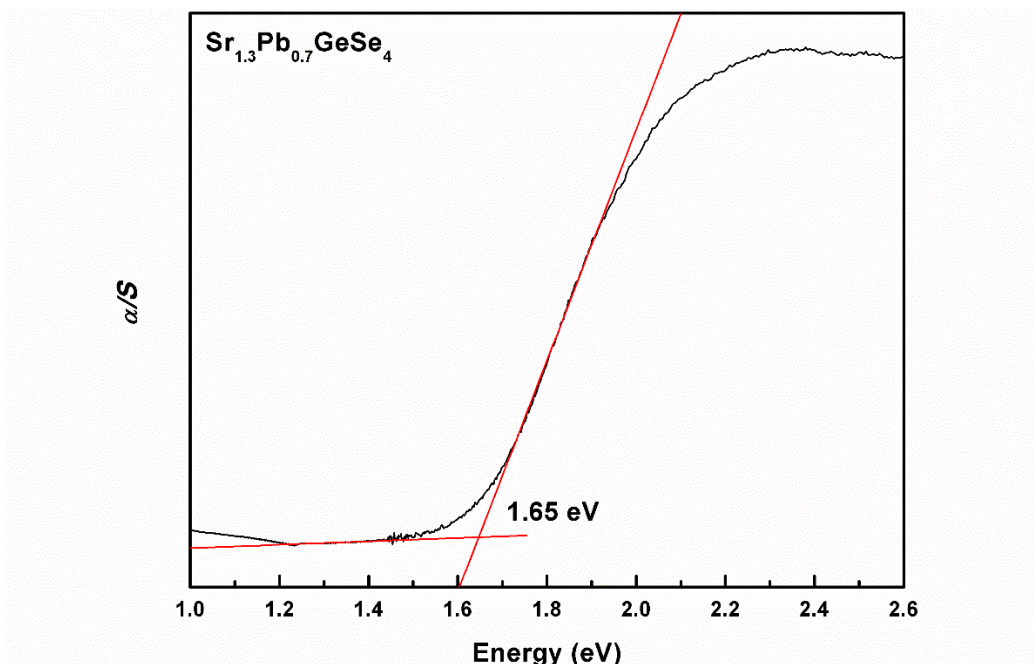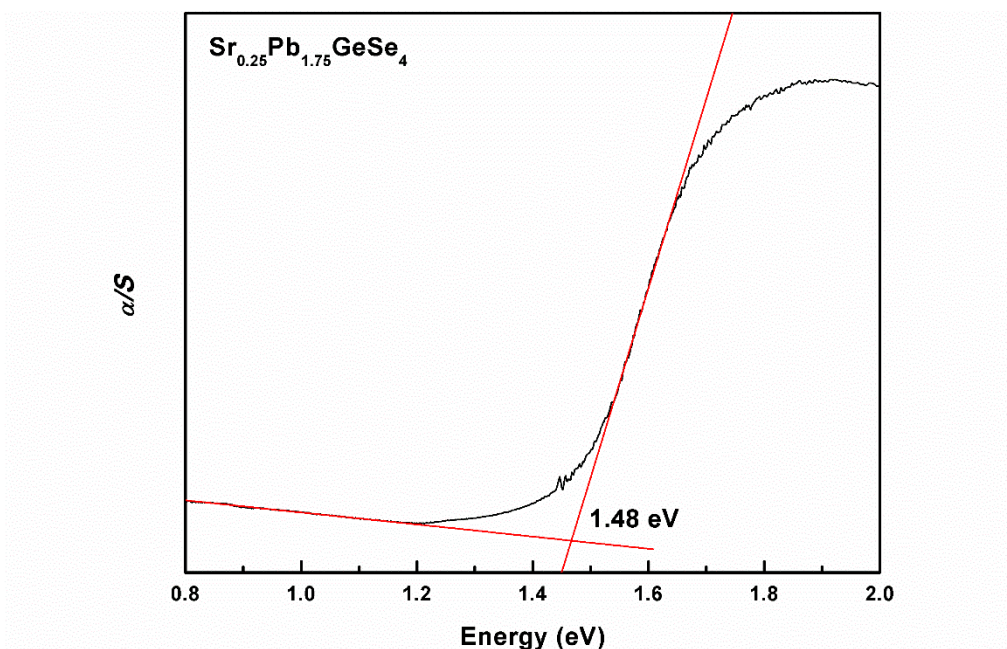Figure 23. The absorption spectrum of $Sr_{1.3}Pb_{0.7}GeSe_4$.

Figure 24. The absorption spectrum of $Sr_{0.25}Pb_{1.75}GeSe_4$.

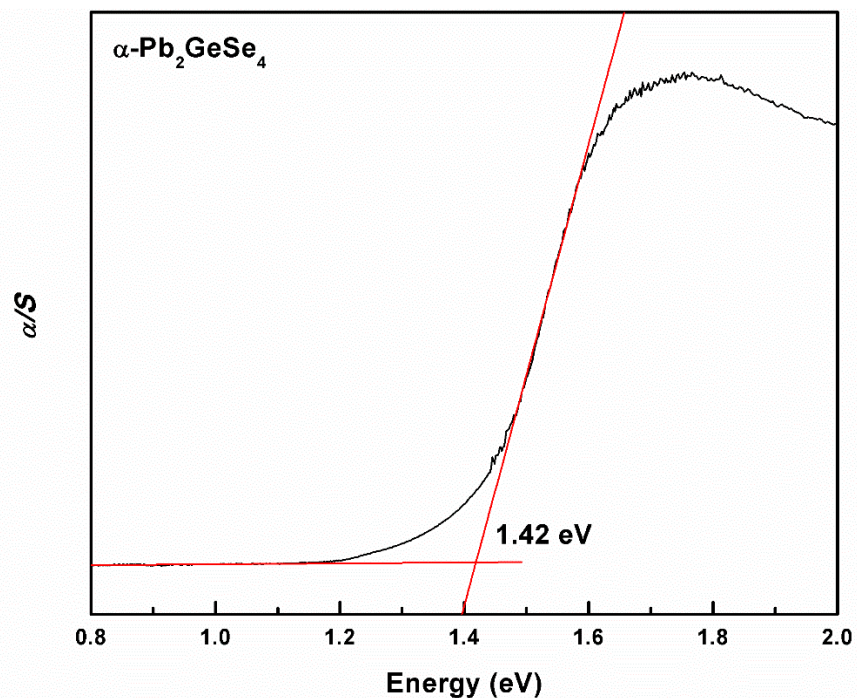Figure 25. The absorption spectrum of α–Pb$_2$GeSe$_4$.

3.2.3 BaCuSiTe$_3$

BaCuSiTe$_3$ was ground and cold-pressed to form a pellet for diffuse reflectance spectroscopy. Compared to the previous samples, this pellet had a relatively low-intensity reflectance. This led to the changes in the baseline near the detector switch to be more noticeable. This sloped baseline was replicated in two different samples of BaCuSiTe$_3$. The optical bandgap was determined to be 1.65 eV for BaCuSiTe$_3$.
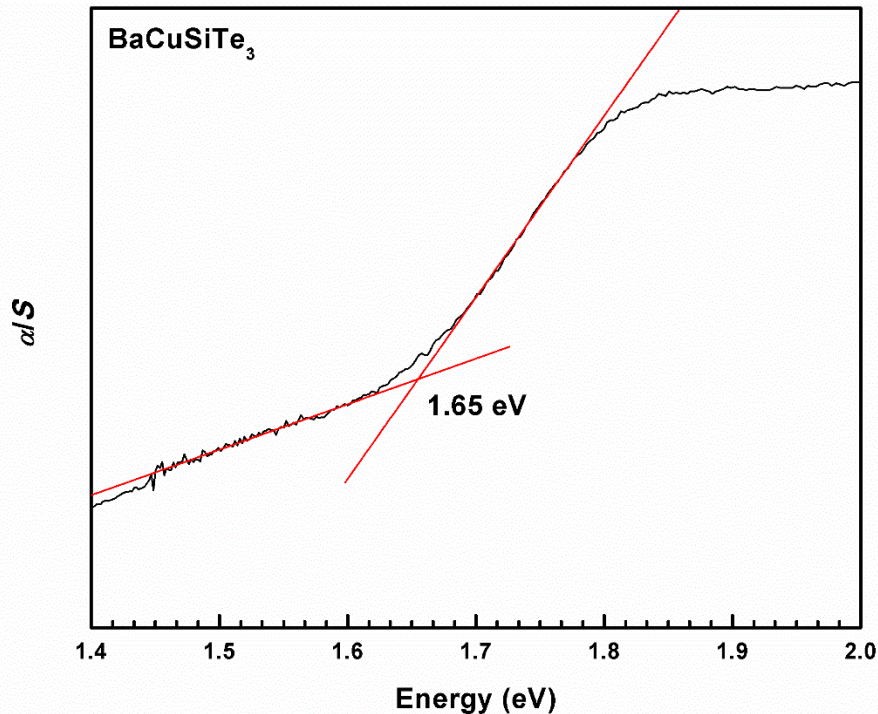
Figure 26. The absorption spectrum of BaCuSiTe₃.

3.3   Theoretical Calculations

DFT software was used to determine the electronic structures and theoretical optical properties of the compounds reported here. The two DFT programs used in this work were WIEN2K and the Elk code. Initial work was done using WIEN2K on the centrosymmetric Ba compounds, however, a limitation of this software was that it could only calculate linear optical properties, i.e. refractive indices. Due to this limitation, alternative open-source software was explored. Finally, the Elk code was chosen as an alternative since it offers the same exchange-correlation functions as WIEN2K. The installation comes with example input files for each type of calculation that can be done in the Elk code. This makes altering the existing input files for the user's personal needs simple even for users that are beginners to Linux operating systems. The nonlinopt subroutine in the Elk code calculates the d-tensor elements that the user specifies based

on the point group and Kleinman symmetry of the crystal structure. A scissor operator was applied in the input files after the self-consistent cycles met the convergence criteria to make the calculated band gap match the experimental value. To be able to compare these calculated d_{ij} values to the experimental d_{eff}, they were converted using equation (1.3.1).

3.3.1 $Ba_7Ge_2Se_7$ and $Ba_6Ge_2Se_{12}$

The centrosymmetric samples $Ba_7Ge_2Se_{17}$ and $Ba_6Ge_2Se_{12}$ were the first compounds that DFT calculations were done for. The electronic structure of $Ba_8Sn_4Se_{17}$ had already been performed by Dr. Abdeljalil Assoud. WIEN2K was the DFT software used for these two compounds. For $Ba_7Ge_2Se_{17}$ and $Ba_6Ge_2Se_{12}$ $5 \times 3 \times 5$ and $6 \times 6 \times 2$ k-point meshes were used respectively. PBE-GGA was used as the exchange-correlation function. The structures inputted used only the atomic coordinates with the greatest occupancies to prevent atoms being too close to their neighbours. The calculated density of states indicated that $Ba_7Ge_2Se_{17}$ had a calculated band gap of 0.72 eV and $Ba_6Ge_2Se_{12}$ had a calculated band gap of 1.24 eV. Both calculated values are much lower than the experimental values (E_g of $Ba_7Ge_2Se_{17}$ = 1.51 eV, E_g of $Ba_6Ge_2Se_{12}$ = 1.75 eV), which is a common observation for such calculations. WIEN2K by default has less smoothing than the Elk code leading to sharper peaks in the DOS than what will be seen in later sections.
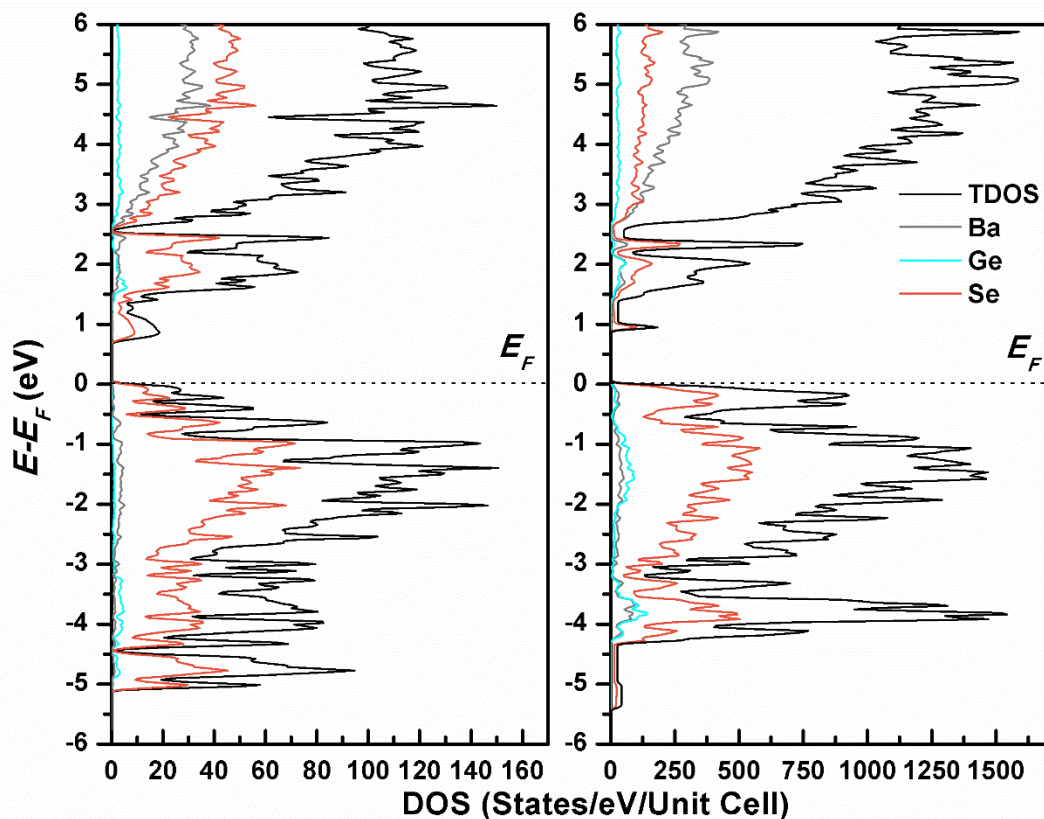
Figure 27. DOS of Ba$_7$Ge$_2$Se$_{17}$ (left) and Ba$_6$Ge$_2$Se$_{12}$ (right).

3.3.2 γ–Sr$_2$GeSe$_4$ and "Sr$_{1.5}$Pb$_{0.5}$GeSe$_4$"

To approximate the crystal structure of Sr$_{1.31}$Pb$_{0.69}$GeSe$_4$ for DFT calculations, which cannot have sites that are randomly mixed with Sr and Pb, it was assumed that a quarter of the mixed sites contained Pb and three quarters contained Sr. This led to a chemical formula of "Sr$_{1.5}$Pb$_{0.5}$GeSe$_4$" and decreased the symmetry from *Ama*2 to *Pm*. The "Sr$_{1.5}$Pb$_{0.5}$GeSe$_4$" model is depicted in Figure 28. The unit cell of "Sr$_{1.5}$Pb$_{0.5}$GeSe$_4$" has the cell parameters a = 6.3856 Å, b = 10.3121 Å, c = 6.3856 Å, and β = 105.9420º.
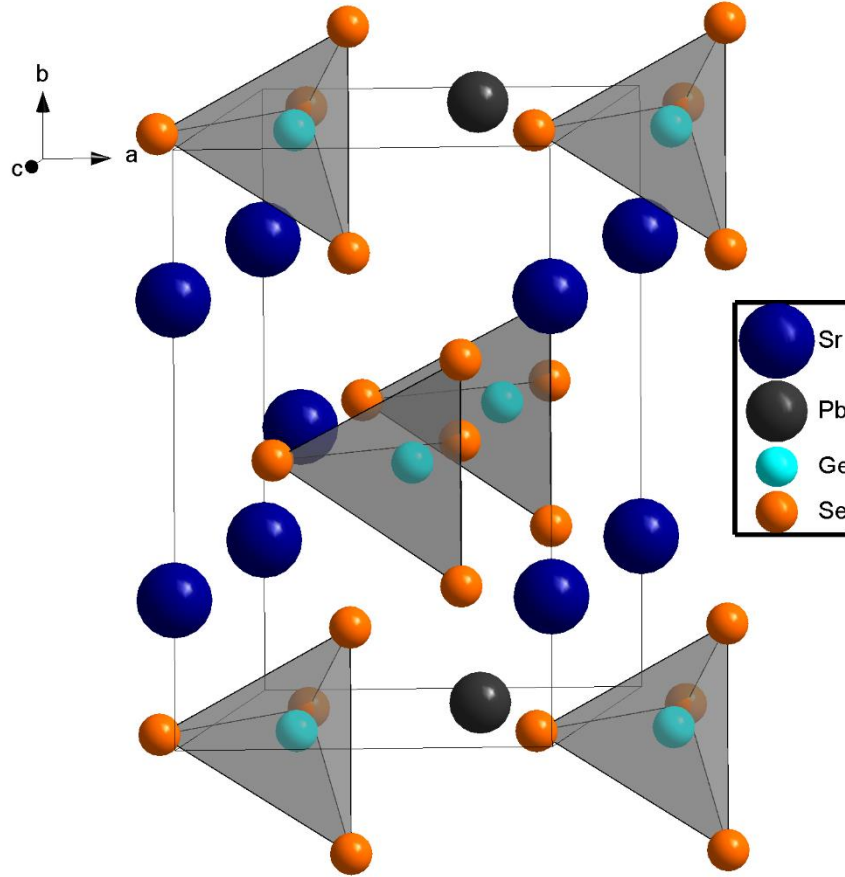
Figure 28. *Pm* model of "Sr$_{1.5}$Pb$_{0.5}$GeSe$_4$" that was used in DFT calculations.

The electronic structure and NLO properties of γ–Sr$_2$GeSe$_4$ and "Sr$_{1.5}$Pb$_{0.5}$GeSe$_4$" were determined using the open-source Elk Code. PBE-GGA was used for the exchange-correlation with a dense $12 \times 12 \times 12$ *k*-point mesh. The second-order NLO susceptibilities were calculated using the sum-over-states formalism. Linear optical properties were determined by the random phase approximation formalism. Since optical properties are determined using excitations from the valence bands to conduction bands to accurately represent the energy gap between bands a scissor operator was used to match the experimental band gap. γ–Sr$_2$GeSe$_4$ has *Ama*2 symmetry and belongs to the *mm*2 point group. Under Kleinman symmetry, the second-order susceptibility tensor for the *mm*2 point group has three non-zero tensor elements: d_{31}, d_{32}, and d_{33}.

$$\begin{bmatrix} 0 & 0 & 0 & 0 & d_{31} & 0 \\ 0 & 0 & 0 & d_{32} & 0 & 0 \\ d_{31} & d_{32} & d_{33} & 0 & 0 & 0 \end{bmatrix} \tag{3.3.2.1}$$

The d_{eff} was then calculated to get a weighted average of the tensor elements. For *mm2* symmetry the d_{eff} has the form[75]:

$$\langle (d_{eff})^2 \rangle = \frac{19}{105}(d_{333})^2 + \frac{13}{105}(d_{333}d_{311} + d_{333}d_{322}) \tag{3.3.2.2}$$

$$+ \frac{44}{105}[(d_{113})^2 + (d_{223})^2] + \frac{26}{105}(d_{113}d_{322})$$

"Sr$_{1.5}$Pb$_{0.5}$GeSe$_4$" has *Pm* symmetry and therefore, belongs to the *m* point group. Under Kleinman symmetry there are six unique non-zero *d*–tensor elements: d_{11}, d_{12}, d_{13}, d_{31}, d_{32}, and d_{33}.

$$\begin{bmatrix} d_{11} & d_{12} & d_{13} & 0 & d_{31} & 0 \\ 0 & 0 & 0 & d_{32} & 0 & d_{12} \\ d_{31} & d_{32} & d_{33} & 0 & d_{13} & 0 \end{bmatrix} \tag{3.3.2.3}$$

The expression for d_{eff} when the point group symmetry is *m* is given by:

$$\langle (d_{eff})^2 \rangle = \frac{19}{105}[(d_{111})^2 + (d_{333})^2] \tag{3.3.2.4}$$

$$+ \frac{13}{105}(d_{111}d_{122} + d_{111}d_{133} + d_{333}d_{311} + d_{333}d_{322})$$

$$+ \frac{44}{105}[(d_{113})^2 + (d_{223})^2] + \frac{13}{105}(d_{223}d_{311} + d_{113}d_{322})$$

All the outputs in Elk are given in atomic units. Therefore, energies were converted from Hartree into eV. The SI unit of second-order NLO susceptibility is m V^{-1}. The conversion from atomic units to m V^{-1} is done by first converting the atomic units to electrostatic units (ESU):

$$atomic\ units = \frac{ESU}{5.8300348177 \times 10^{-8}} \qquad (3.3.2.3)$$

From ESU the value can be converted to SI units by the following conversion:

$$SI = ESU\ \frac{4\pi}{30000} \qquad (3.3.2.4)$$

NLO susceptibility values end up being very small so the d–tensor elements are usually written with units of pm V^{-1}.

The calculated band gaps of γ–Sr_2GeSe_4 and "$Sr_{1.5}Pb_{0.5}GeSe_4$" were determined to be 1.92 eV and 1.59 eV, respectively. Due to the different symmetries of the models, the respective band structures followed different Brillouin zone paths. These values are in good agreement with the band gaps determined via diffuse reflectance spectroscopy (2.00 eV and 1.65 eV for γ–Sr_2GeSe_4 and $Sr_{1.3}Pb_{0.7}GeSe_4$ respectively) when considering that DFT software is known to underestimate band gaps. The band structure of γ–Sr_2GeSe_4 indicates that there are two isolated bands above the Fermi level. These bands arise from the 4s orbitals on Ge^{4+}. These bands have been observed in similar Sn compounds.[76] With the addition of Pb, these bands merge with the rest of the conduction band as seen in Figure 30.
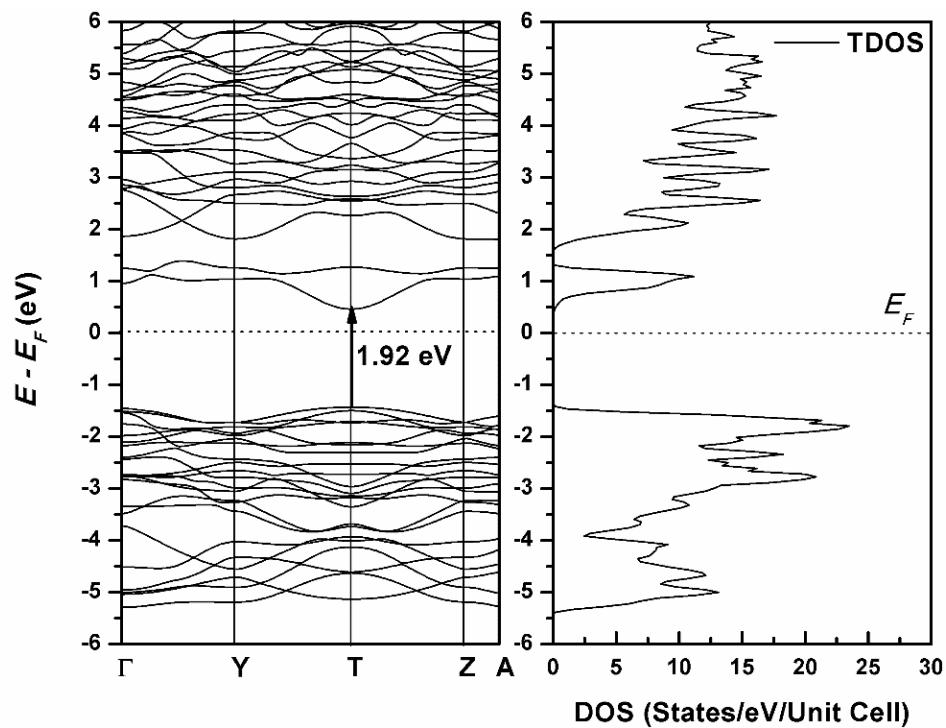
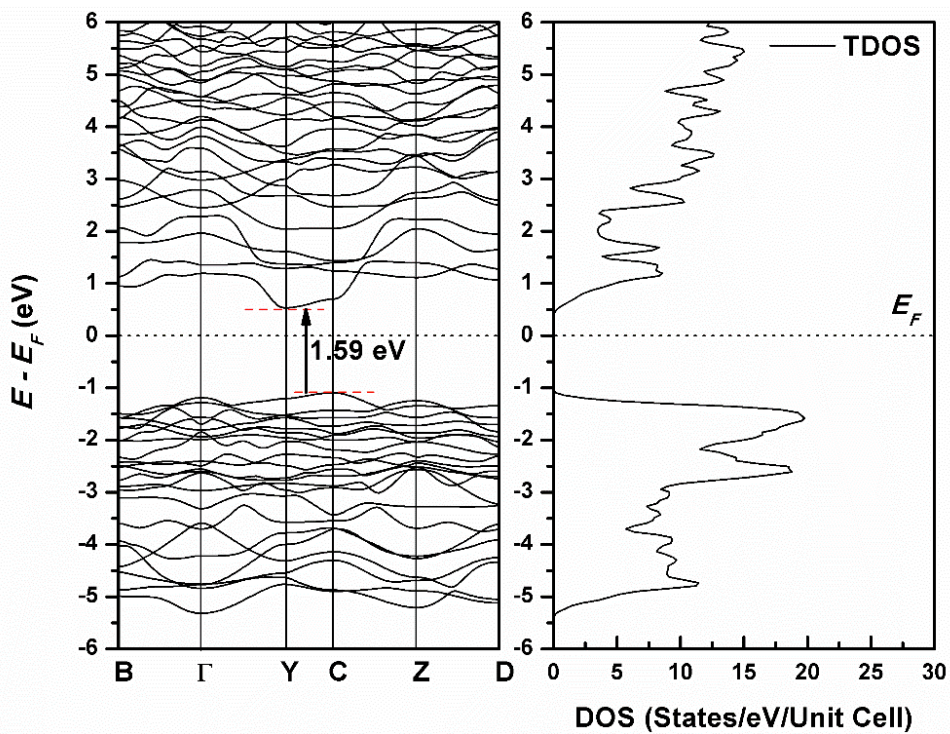Figure 29. Band structure (left) and DOS (right) of γ–Sr_2GeSe_4.

Figure 30. Band structure (left) of "$Sr_{1.5}Pb_{0.5}GeSe_4$". DOS (right) of "$Sr_{1.5}Pb_{0.5}GeSe_4$".

In the energy-dependent NLO susceptibility plots it is clearly visible that the interband component of NLO susceptibility begins to dominate the curves at half the band gap energy. Under the static limit ($\omega = 0$) the NLO susceptibilities of γ–Sr_2GeSe_4 were determined to be d_{31} = 7.1 pm V^{-1}, d_{32} = -14.3 pm V^{-1}, d_{33} = -11.8 pm V^{-1}, and d_{eff} = 10.8 pm V^{-1}. Since γ–Sr_2GeSe_4 is orthorhombic, it has biaxial birefringence. Therefore, the refractive indices were calculated for each crystallographic axis. This gave refractive indices of n_{xx} = 2.63, n_{yy} = 2.59, and n_{zz} = 2.68. From these values, the birefringence was found to be 0.08 at the static limit.

The NLO susceptibilities of "$Sr_{1.5}Pb_{0.5}GeSe_4$" were determined to be d_{11} = 20.4 pm V^{-1}, d_{12} = -9.4 pm V^{-1}, d_{13} = -2.0 pm V^{-1}, d_{31} = 7.8 pm V^{-1}, d_{32} = -5.0 pm V^{-1}, d_{33} = 5.6 pm V^{-1}, and d_{eff} = 8.8 pm V^{-1} at the static limit. Monoclinic crystal systems also have biaxial birefringence. The three refractive indices were determined to be n_{xx} = 2.83, n_{yy} = 2.74, and n_{zz} = 2.84. Therefore, the birefringence is 0.10. Both the d_{eff} and birefringence of the "$Sr_{1.5}Pb_{0.5}GeSe_4$" model are similar to the that of γ–Sr_2GeSe_4 indicating that even though decreasing the symmetry increased the number of unique d_{ij} values, the d_{eff} are still comparable between compounds.

The refractive indices behave as one would expect; with the refractive index increasing as the band gap of the compounds decreases. Surprisingly, the d_{eff} did not follow the expected trend since "$Sr_{1.5}Pb_{0.5}GeSe_4$", which has a smaller band gap than γ–Sr_2GeSe_4 had a smaller d_{eff} than γ–Sr_2GeSe_4 at the static limit. Both the d_{eff} of γ–Sr_2GeSe_4 and "$Sr_{1.5}Pb_{0.5}GeSe_4$" are slightly lower than NLO susceptibility of current benchmark NLO compound $AgGaS_2$ (d_{36} = 13 pm V^{-1}).
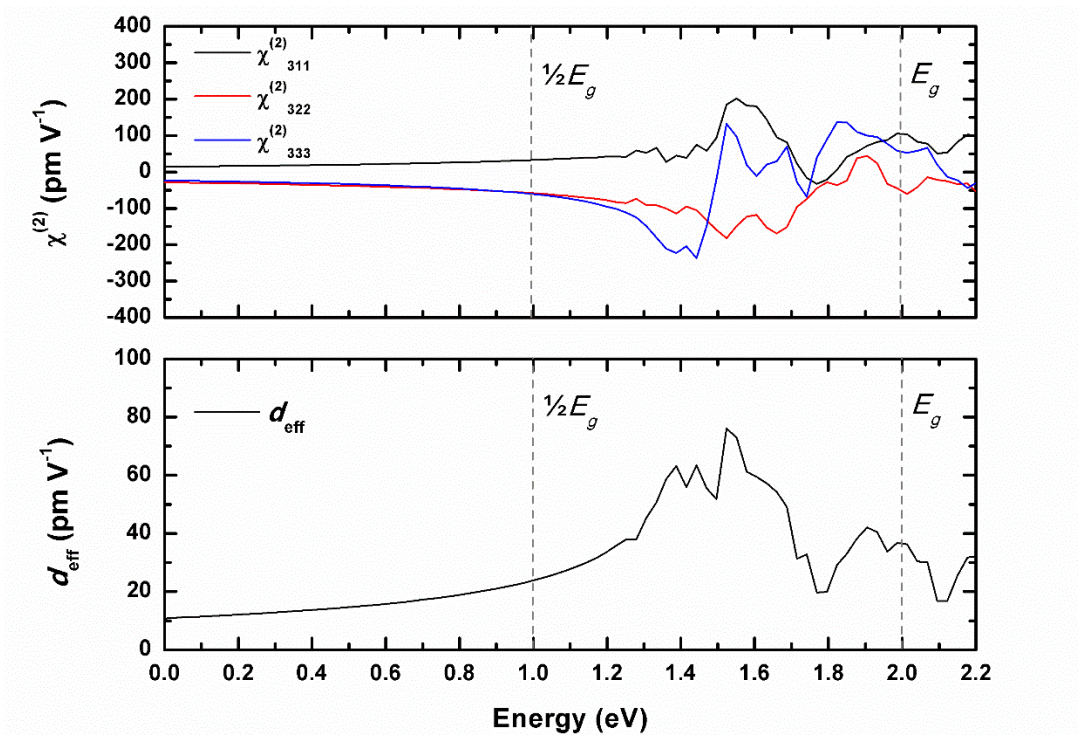
Figure 31. NLO susceptibilities of γ–Sr$_2$GeSe$_4$ (top). d_{eff} of γ–Sr$_2$GeSe$_4$ (bottom).
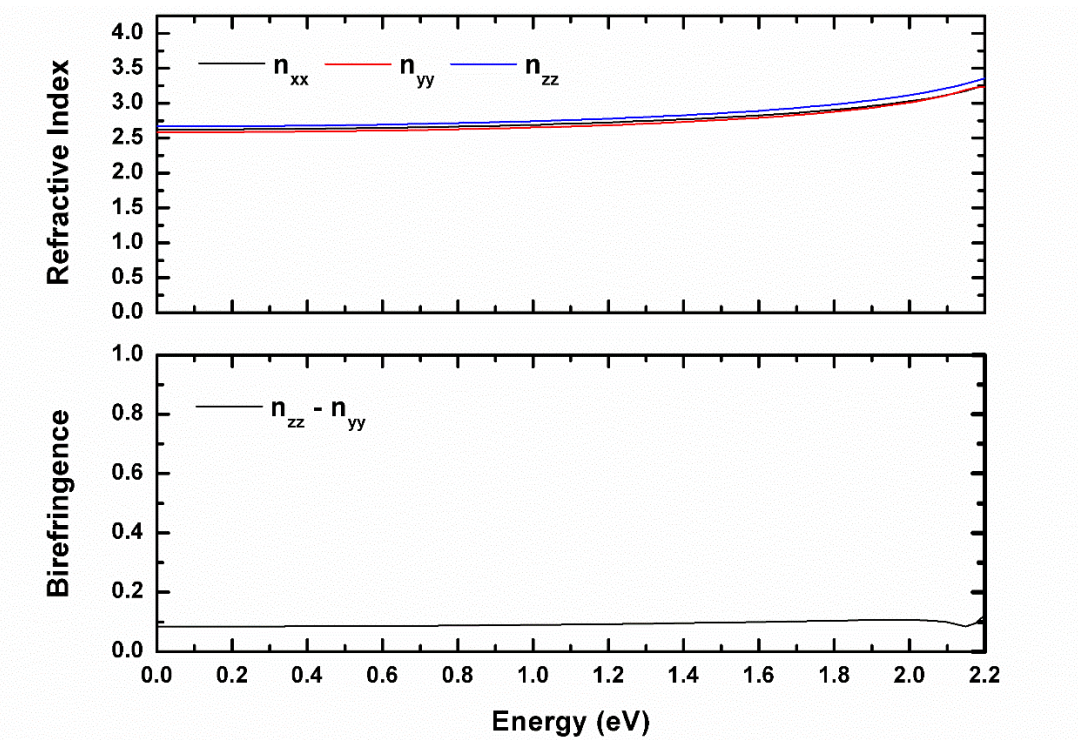
Figure 32. Refractive indices of γ–Sr$_2$GeSe$_4$ (top). Birefringence of γ–Sr$_2$GeSe$_4$ (bottom).
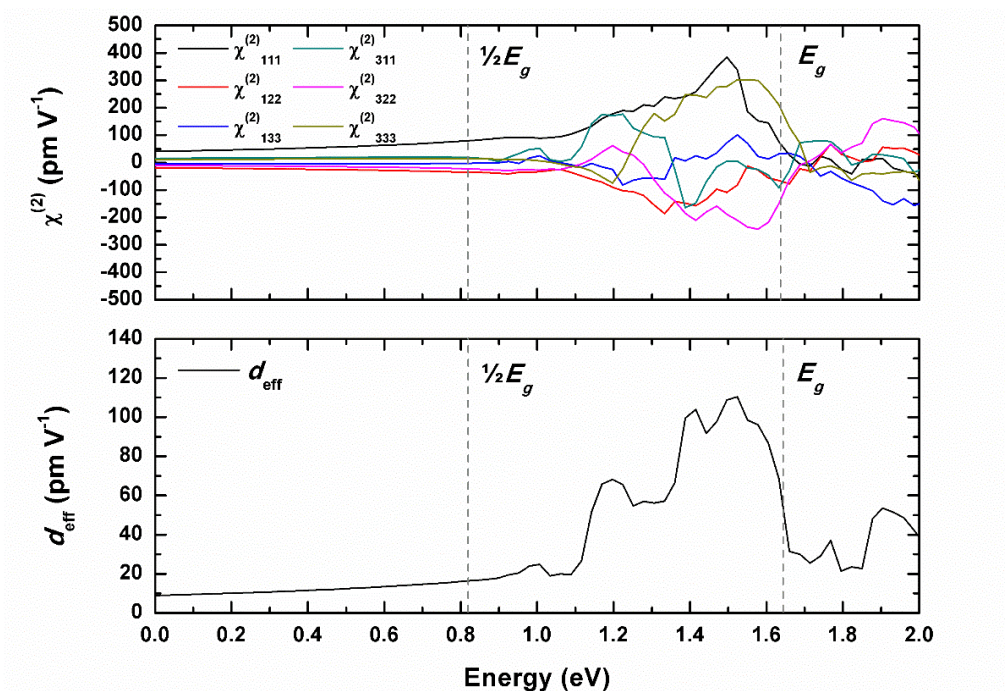
Figure 33. NLO susceptibilities of "$Sr_{1.5}Pb_{0.5}GeSe_4$" (top). d_{eff} of "$Sr_{1.5}Pb_{0.5}GeSe_4$" (bottom).
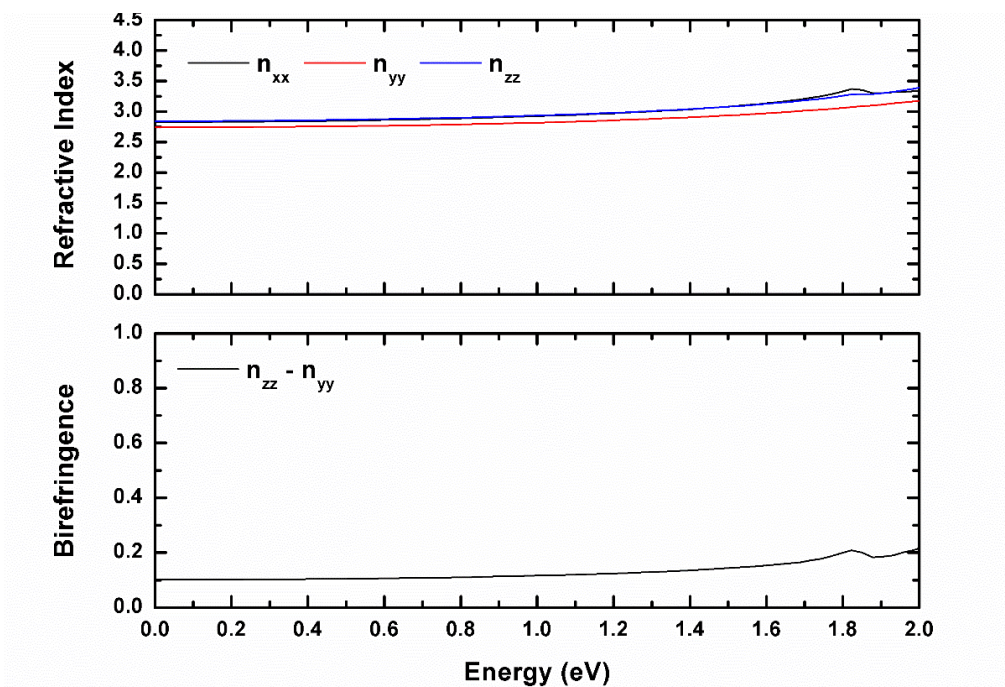
Figure 34. Refractive indices of "$Sr_{1.5}Pb_{0.5}GeSe_4$" (top). Birefringence of "$Sr_{1.5}Pb_{0.5}GeSe_4$" (bottom).

3.3.3 β–Pb₂GeSe₄

Using Elk the electronic structure of β–Pb₂GeSe₄ was calculated. PBE-GGA was used as the exchange-correlation function with a dense $8 \times 8 \times 8$ k-point mesh in the Brillouin zone. The band structure and DOS of β–Pb₂GeSe₄ indicated that this compound is a semi-metal without a band gap. The lowest conduction band crosses the Fermi level between the B and D points in the Brillouin zone and the highest valence band crosses the Fermi level between the Z and Γ points in the Brillouin zone. Using more accurate computation models to calculate the band gap of β–Pb₂GeSe₄ such as the modified Becke-Johnson (mBJ) would likely show that there is, in fact, a narrow band gap.[77]
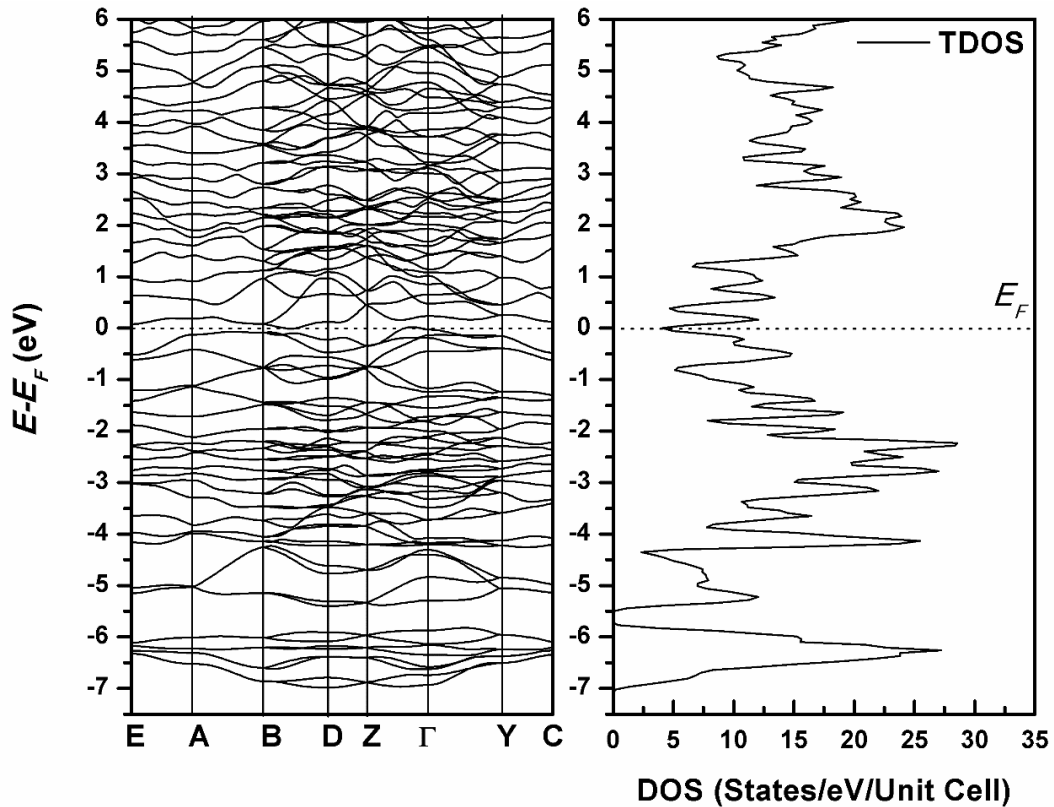

Figure 35. Band structure (left) and DOS of β–Pb₂GeSe₄ (right).

3.3.4 BaCuSiTe₃

The optical properties of $BaCuSiTe_3$ were determined using the Elk code with PBE-GGA as the exchange-correlation function. An $8 \times 8 \times 8$ k-point mesh was used to achieve convergence in the self-consistent cycle. A scissor operator was used to raise the calculated band gap to the experimental value after the electronic structure calculation. The sum-over-states formalism was used to determine the NLO properties whereas the random phase approximation was used for the linear optical properties. The electronic structure calculation showed that $BaCuSiTe_3$ had an indirect band gap of 1.49 eV.[64] Using a scissor operator the band gap was increased to match the experimental value of 1.65 eV.
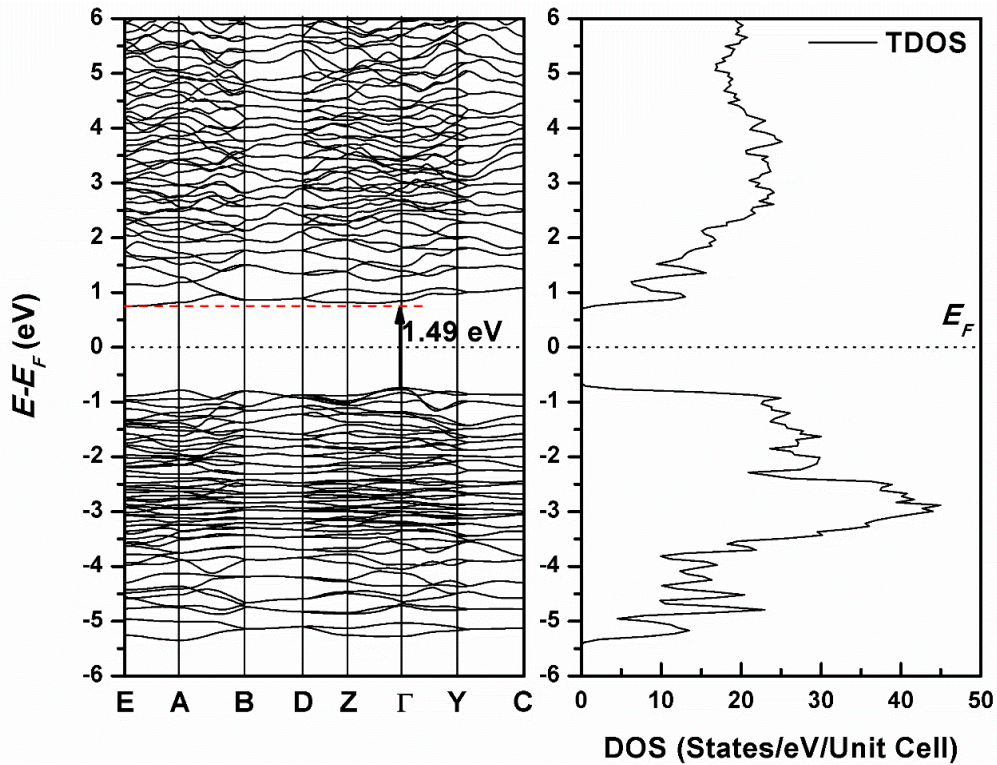

Figure 36. Band structure (left) and DOS of $BaCuSiTe_3$ (right).

$BaCuSiTe_3$ has Pc symmetry meaning it belongs to the m point group. Like in the case of "$Sr_{1.5}Pb_{0.5}GeSe_4$" there are six non-zero unique d–tensor elements: d_{11}, d_{12}, d_{13}, d_{31}, d_{32}, and d_{33}.

The expression for d_{eff} is therefore the same as well and given by equation (3.3.2.2). The NLO 7susceptibilities of BaCuSiTe₃ are: $d_{11} = -3.2$ pm V⁻¹, $d_{12} = 11.3$ pm V⁻¹, $d_{13} = -4.4$ pm V⁻¹, $d_{31} = -6.2$ pm V⁻¹, $d_{32} = -4.0$ pm V⁻¹, $d_{33} = -6.8$ pm V⁻¹, and $d_{eff} = 3.4$ pm V⁻¹ at the static limit. The three refractive indices of BaCuSiTe₃ are $n_{xx} = 2.98$, $n_{yy} = 2.99$, and $n_{zz} = 3.21$ making the birefringence 0.23. This modest d_{eff} of 3.4 pm V⁻¹ is approximately a quarter of the NLO susceptibility of the benchmark AgGaS₂ ($d_{36} = 13$ pm V⁻¹). The birefringence is also larger than ideal for phase-matching.
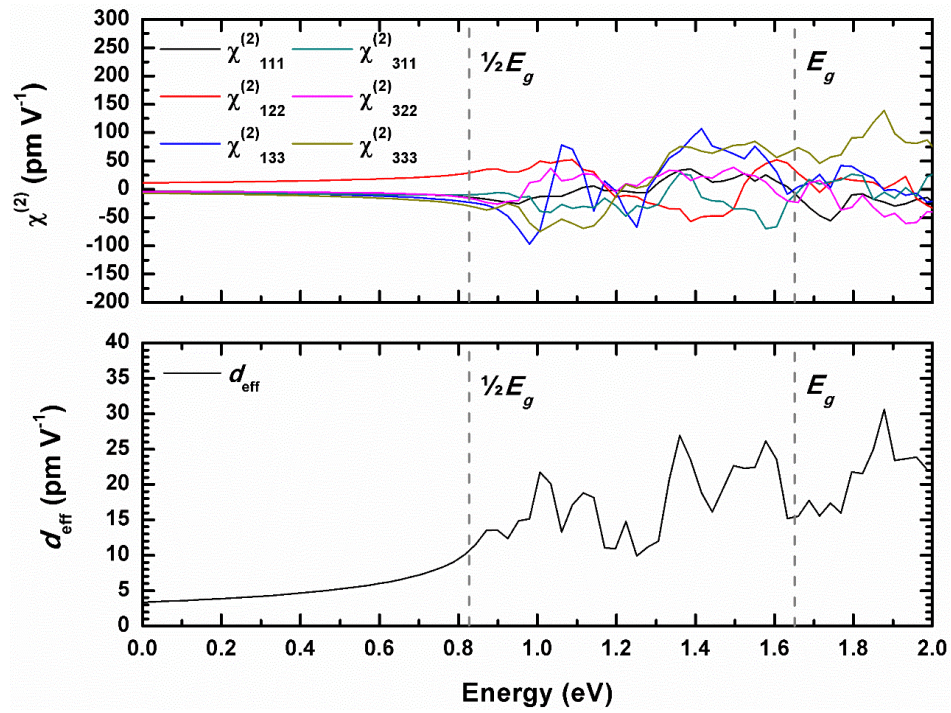

Figure 37. NLO susceptibilities of BaCuSiTe₃ (top). d_{eff} of BaCuSiTe₃ (bottom).
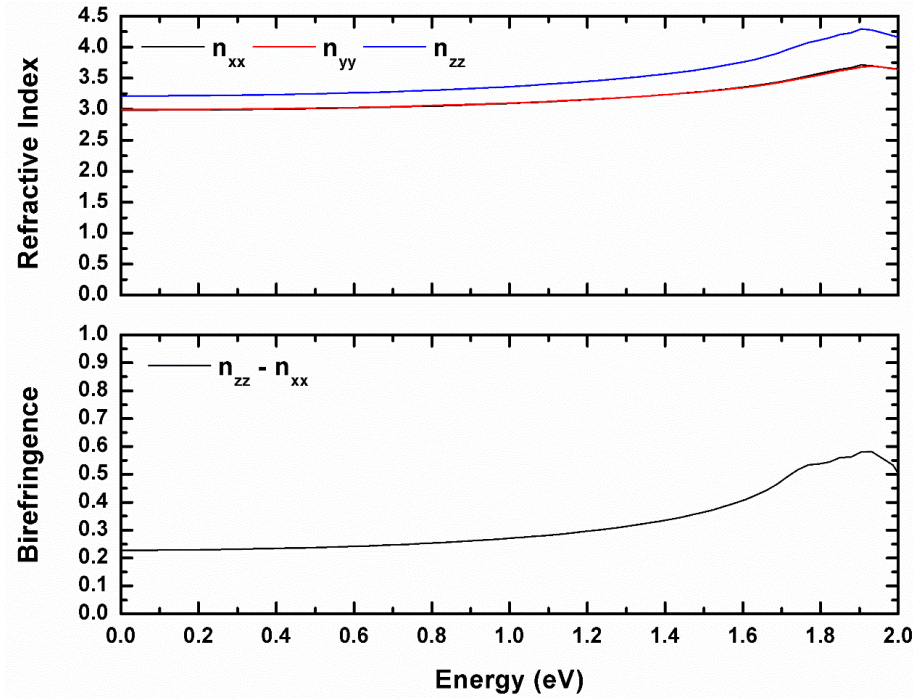
Figure 38. Refractive indices of BaCuSiTe$_3$ (top). Birefringence of BaCiSiTe$_3$ (bottom).

3.4 SHG Measurements

SHG Measurements were performed by the Halasyamani group at the University of Houston. Approximately 2 g samples of γ–Sr$_2$GeSe$_4$, Sr$_{1.3}$Pb$_{.7}$GeSe$_4$, Sr$_{0.25}$Pb$_{1.75}$GeSe$_4$, α–Pb$_2$GeSe$_4$, and BaCuSiTe$_3$ were hot-pressed to achieve high density and mailed to the Halasyamani group. There, the samples were ground and sieved into the particle sizes ranges: < 20 μm, 20 – 45 μm, 45 - 63 μm, 63 – 75 μm, 75 – 90 μm, 90 – 125 μm. The sieved powders were loaded into silica tubes with an inner diameter of 4 mm and flame sealed to contain them. These steps were also done to prepare the α–SiO$_2$ standard. The sealed samples were hit with a 1064 nm Nd:YAG laser to produce the SHG light. The scattered light was focused onto a PMT detector after passing through a short pass filter. This was to filter out scattered 1064 nm from the laser source so only 532 nm light was detected. The intensities of the PMT signal were

75

compared with the standard's signal intensity to determine d_{eff}. As seen in Figure 39 the laser

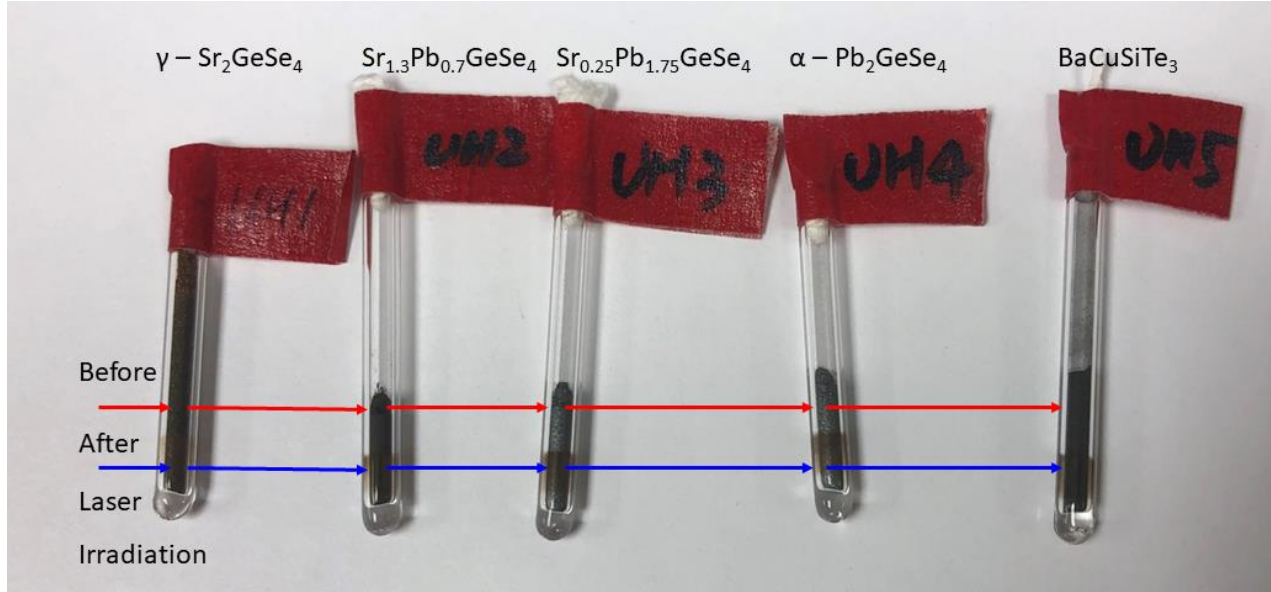caused the samples to noticeably degrade due to partially absorbing the laser light.

Figure 39. Comparison of the sealed samples before and after being exposed to the laser showing

significant laser damage.

3.4.1 $Sr_{2-x}Pb_xGeSe_4$ (x = 0, 0.7, 1.75, and 2)

None of the samples in the $Sr_{2-x}Pb_xGeSe_4$ series were type I phase matchable at 1064 nm.

In other words, their refractive indices were too different at 1064 nm and 532 nm to conserve

momentum. The expected trend of a non-type I phase matchable material is observed where a

maximum value is achieved before decaying and levelling off. To determine d_{eff} of these samples

$\alpha–SiO_2$ can be used as a standard since it also does not phase match at 1064 nm. This is not to

say that these compounds could not phase match at longer wavelengths in the IR region.

Clear separation in the data can be seen in Figure 40 with the orthorhombic samples $\gamma–$

Sr_2GeSe_4 and $Sr_{1.3}Pb_{0.7}GeSe_4$ have intensities an order of magnitude greater than the cubic

counterparts $Sr_{0.25}Pb_{1.75}GeSe_4$ and α–Pb_2GeSe_4. This is due to cubic compounds being unable to

phase match due to not being birefringent. Using equation (1.4.7), the d_{eff} of γ–Sr_2GeSe_4, and

$Sr_{1.3}Pb_{0.7}GeSe_4$ were determined to be 2.6 pm V^{-1} and 2.3 pm V^{-1} respectively for the largest

particle sizes. The experimental results from the orthorhombic compounds agree with the

theoretical calculation that adding Pb to the γ–Sr_2GeSe_4 has the unintuitive effect of decreasing

the NLO susceptibility despite Pb^{2+} being more polarizable than Sr^{2+}. $Sr_{0.25}Pb_{1.75}GeSe_4$ and α–

Pb_2GeSe_4 do follow the expected trend of increasing NLO susceptibility with increasing Pb

content. $Sr_{0.25}Pb_{1.75}GeSe_4$ and α–Pb_2GeSe_4 have d_{eff} of 0.68 pm V^{-1} and 0.79 pm V^{-1} respectively.

The experimental values of d_{eff} for the orthorhombic compounds are approximately a quarter of

the theoretical values. This has been attributed to band gaps of these compounds being narrow

enough to absorb a significant amount of 532 nm light produced by SHG.
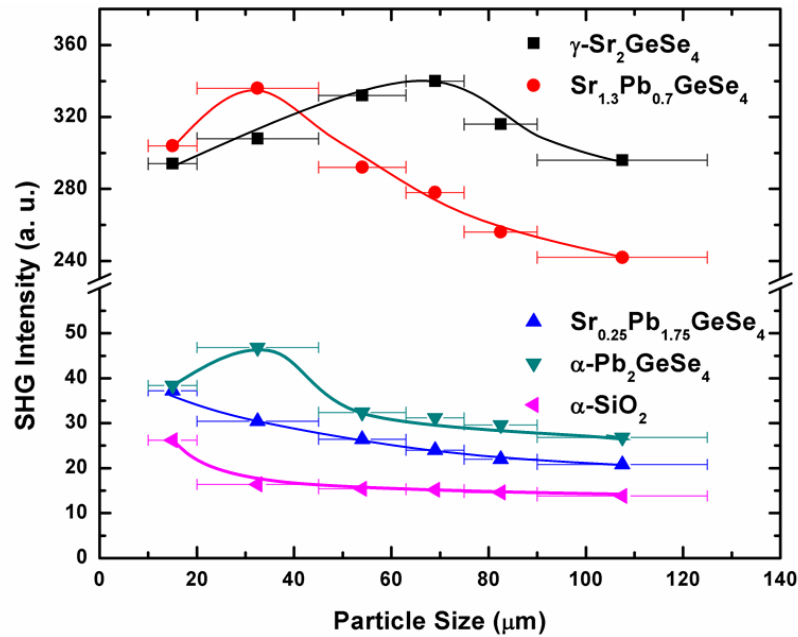

Figure 40. The SHG intensities of $Sr_{2-x}Pb_xGeSe_4$ (x = 0, 0.7, 1.75, and 2) relative to the α–SiO_2

standard. All these compounds show non-type I phase-matching behaviour. Curves are drawn to

guide the eye.

3.4.2 BaCuSiTe₃

To measure the SHG intensity and phase-matching properties of BaCuSiTe₃ a sample was hot-pressed into a pellet to achieve high density. The densified pellet was crushed and sieved into six size ranges listed above. α–SiO_2 was used as the standard for BaCuSiTe₃ since BaCuSiTe₃ does not phase match at 1064 nm. This was foreseen by due to the relatively large birefringence that was calculated by the theoretical optical calculations. The ground and sieved samples of BaCuSiTe₃ were loaded into silica tubes and sealed. Using equation (1.4.3) again and the intensity of the α–SiO_2 standard the experimental d_{eff} was calculated to be 0.52 pm V^{-1} for the largest sieved particles. This is lower than the already modest calculated d_{eff} of 3.4 pm V^{-1}. As with the $Sr_{2-x}Pb_xGeSe_4$ compounds the band gap of BaCuSiTe₃ is narrow enough that it absorbs the SHG 532 nm light.
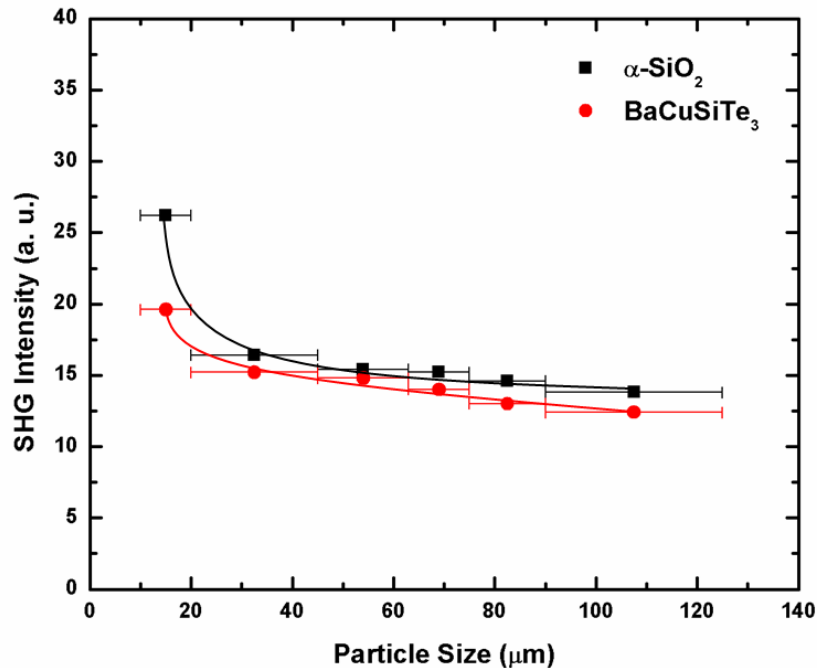

Figure 41. The SHG intensity of BaCuSiTe₃ relative to the standard α–SiO_2. The curves are drawn to guide the eye.

4 Conclusion

The optical properties of several new tetrel compounds have been determined along with their respective crystal structures. The centrosymmetric compounds $Ba_7Ge_2Se_{17}$, $Ba_6Ge_2Se_{12}$, $Ba_8Sn_4Se_{17}$ had their syntheses optimized and their experimental band gaps determined. The NLO properties of the NCS tetrel compounds were also determined.

The effect of substituting Pb into the γ–Sr_2GeSe_4 structure had surprising results. For the Pb rich cubic phases $Sr_{0.25}Pb_{1.75}GeSe_4$ and α–Pb_2GeSe_4 the expected trend was observed as d_{eff} increased with increasing Pb content. In the Sr rich orthorhombic phases, γ–Sr_2GeSe_4 and $Sr_{1.3}Pb_{0.7}GeSe_4$, adding Pb decreased the d_{eff}. This was predicted by using a theoretical supercell model. The theoretical values of d_{eff} did not align perfectly with the experimental values determined using the Kurtz-Perry technique, but the lower experimental values can be attributed to using a laser with a wavelength that is too high in energy for these materials. As a result, the powdered samples were damaged as well as partially absorbed the SHG light. Despite this, the theoretical NLO susceptibility calculation of the supercell model was able to correctly predict adding Pb would decrease the d_{eff} of the γ–Sr_2GeSe_4 structure is noteworthy. This is significant because it means that d_{eff} can be used to overcome the difference in d–tensor elements arising from the different symmetry of the supercell. To the best of our knowledge, this is the first time this approach has been used to predict the NLO properties of a compound with atomic positions that have mixed occupancies.

The theoretical calculation and experimental results for $BaCuSiTe_3$ both indicate a surprisingly modest NLO response despite possessing the large anionic $[Si_2Te_6]^{6-}$ group. This ethane-like group is in a staggered conformation that almost has inversion symmetry. Since these

$[Si_2Te_6]^{6-}$ groups are in this conformation they end up contributing very little to the NLO susceptibility.

Unfortunately, past reports have indicated that all the NCS compounds melt incongruently meaning that large crystals could not be grown using the Bridgeman-Stockbarger technique. Aside from the practical problems of using these compounds none displayed phase-matching capabilities or a high laser damage threshold. It is possible that these issues may problems be resolved if a longer wavelength laser was used, which we intend to pursue in the near future.

5 References

(1)   Winick, K. A. Rare-Earth-Doped Waveguide Lasers in Glass and LiNbO₃: A Review. *SPIE* **1998**, *3280*, 88–104.

(2)   Arriola, A.; Gross, S.; Ams, M.; Gretzinger, T.; Le Coq, D.; Wang, R. P.; Ebendorff-Heidepriem, H.; Sanghera, J.; Bayya, S.; Shaw, L. B.; et al. Mid-Infrared Astrophotonics: Study of Ultrafast Laser Induced Index Change in Compatible Materials. *Opt. Mater. Express* **2017**, *7*, 698–711.

(3)   Pestov, D.; Wang, X.; Ariunbold, G. O.; Murawski, R. K.; Sautenkov, V. A.; Dogariu, A.; Sokolov, A. V.; Scully, M. O. Single-Shot Detection of Bacterial Endospores via Coherent Raman Spectroscopy. *Proc. Natl. Acad. Sci.* **2008**, *105*, 422–427.

(4)   Wooten, E. L.; Kissa, K. M.; Yi-Yan, A.; Murphy, E. J.; Lafaw, D. A.; Hallemeier, P. F.; Maack, D.; Attanasio, D. V.; Fritz, D. J.; McBrien, G. J.; et al. Review of Lithium Niobate Modulators for Fiber-Optic Communications Systems. *IEEE J. Sel. Top. Quantum Electron.* **2000**, *6*, 69–82.

(5)   Zhao, Z.; Wu, B.; Wang, X.; Pan, Z.; Liu, Z.; Zhang, P.; Shen, X.; Nie, Q.; Dai, S.; Wang, R. Mid-Infrared Supercontinuum Covering 2.0–16 μm in a Low-Loss Telluride Single-Mode Fiber. *Laser Photonics Rev.* **2017**, *11*, 1–5.

(6)   Chung, I.; Kanatzidis, M. G. Metal Chalcogenides: A Rich Source of Nonlinear Optical Materials. *Chemistry of Materials*. **2014**, *26*, 849–869.

(7)   Lan, H.; Liang, F.; Lin, Z.; Yu, H.; Zhang, H.; Wang, J. Langasite Family Midinfrared Nonlinear Optical Oxide Materials: Structure, Property, and Applications. *Int. J. Opt.* **2017**, *2017*, 1–13.

(8)   Boyd, R. W. *Nonlinear Optics, Third Edition*; 2013.

(9)   Hutchings, D. C. *Applied Nonlinear Optics*; 2004.

(10)   Kleinman, D. A. Nonlinear Dielectric Polarization in Optical Media. *Phys. Rev.* **1962**, *126*, 1977–1979.

(11)   Kurtz, S. K.; Perry, T. T. A Powder Technique for the Evaluation of Nonlinear Optical Materials. *J. Appl. Phys.* **1968**, *39*, 3798–3813.

(12)   Liu, S.; Sinclair, M. B.; Saravi, S.; Keeler, G. A.; Yang, Y.; Reno, J.; Peake, G. M.; Setzpfandt, F.; Staude, I.; Pertsch, T.; et al. Resonantly Enhanced Second-Harmonic Generation Using III-V Semiconductor All-Dielectric Metasurfaces. *Nano Lett.* **2016**, *16*, 5426–5432.

(13)   Ok, K. M.; Chi, E. O.; Halasyamani, S. Bulk Characterization Methods for Non-Centrosymmetric Materials: Second-Harmonic Generation, Piezoelectricity, Pyroelectricity, and Ferroelectricity. *Chem. Soc. Rev.* **2006**, *35*, 710–717.

(14)   Abinit. http://www.abinit.org/ (accessed Sep 20, 2019).

(15)   The Elk Code. http://elk.sourceforge.net/ (accessed Sep 20, 2019).

(16)   The VASP site. http://www.vasp.at/ (accessed Sep 20, 2019).

(17)   Lejaeghere, K.; Bihlmayer, G.; Björkman, T.; Blaha, P.; Blügel, S.; Blum, V.; Caliste, D.; Castelli, I. E.; Clark, S. J.; Dal Corso, A.; et al. Reproducibility in Density Functional Theory Calculations of Solids. *Science (80-.).* **2016**, *351*, 1415.

(18)   CASTEP. http://www.castep.org/ (accessed Sep 20, 2019).

(19)   Aversa, C.; Sipe, E. Nonlinear Optical Susceptibilities of Semiconductors: Results with a Length-Gauge Analysis. *Phys. Rev. B* **1995**, *52*, 14636–14645.

(20)   Hughes, J. L. P.; Sipe, J. Calculation of Second-Order Optical Response in Semiconductors. *Phys. Rev. B* **1996**, *53*, 10751–10763.

(21) Sharma, S.; Ambrosch-Draxl, C. Second-Order Optical Response from First Principles. *Phys. Scr.* **2004**, *128*, 128–134.

(22) Veithen, M.; Gonze, X.; Ghosez, P. Nonlinear Optical Susceptibilities, Raman Efficiencies, and Electro-Optic Tensors from First-Principles Density Functional Perturbation Theory. *Phys. Rev. B - Condens. Matter Mater. Phys.* **2005**, *71*, 1–14.

(23) Luo, X.; Li, Z.; Guo, Y.; Yao, J.; Wu, Y. Recent Progress on New Infrared Nonlinear Optical Materials with Application Prospect. *J. Solid State Chem.* **2019**, *270*, 674–687.

(24) Bai, L.; Lin, Z.; Wang, Z.; Chen, C.; Lee, M. H. Mechanism of Linear and Nonlinear Optical Effects of Chalcopyrite $AgGaX_2$ (X=S, Se, and Te) Crystals. *J. Chem. Phys.* **2004**, *120*, 8772–8778.

(25) Chen, C. T. Development of New Nonlinear Optical Crystals in the Borate Series. *Opt. Laser Technol.* **1994**, *26*, 205.

(26) Kanatzidis, M. G.; Pöttgen, R.; Jeitschko, W. The Metal Flux: A Preparative Tool for the Exploration of Intermetallic Compounds. *Angew. Chemie - Int. Ed.* **2005**, *44*, 6996–7023.

(27) Pearson, R. G. The Second-Order Jahn-Teller Effect. *J. Mol. Struct. THEOCHEM* **1983**, *103*, 25–34.

(28) Lee, D. W.; Oh, S. J.; Halasyamani, P. S.; Ok, K. M. New Quaternary Tellurite and Selenite: Synthesis, Structure, and Characterization of Centrosymmetric $InVTe_2O_8$ and Noncentrosymmetric $InVSe_2O_7$. *Inorg. Chem.* **2011**, *50*, 4473–4480.

(29) Khyzhun, O. Y.; Bekenev, V. L.; Parasyuk, O. V.; Danylchuk, S. P.; Denysyuk, N. M.; Fedorchuk, A. O.; AlZayed, N.; Kityk, I. V. Single Crystal Growth and the Electronic Structure of Orthorhombic Tl_3PbBr_5: A Novel Material for Non-Linear Optics. *Opt. Mater. (Amst).* **2013**, *35*, 1081–1089.

(30) Aliev, A.; Kovrugin, V. M.; Colmont, M.; Terryn, C.; Huvé, M.; Siidra, O. I.; Krivovichev, S. V; Mentré, O. Revised Bismuth Chloroselenite System: Evidence of a Noncentrosymmmetric Structure with a Giant Unit Cell. *Cryst. Growth Des.* **2014**, *14*, 3026–3034.

(31) Cao, X.-L.; Hu, C.-L.; Kong, F.; Mao, J.-G. Explorations of New SHG Materials in the Alkali-Metal−Nb^{5+}−Selenite System. *Inorg. Chem* **2015**, *55*, 10978–10984.

(32) Ayeb, Y.; Benghia, A.; Kanoun, M. B.; Arar, R.; Lagoun, B.; Goumri-Said, S. Elucidating Linear and Nonlinear Optical Properties of Defect Chalcopyrite Compounds ZnX_2Te_4 (X=Al, Ga, In) from Electronic Transitions. *Solid State Sci.* **2019**, *87*, 39–48.

(33) Guo, Y.; Liang, F.; Yao, J.; Lin, Z.; Yin, W.; Wu, Y.; Chen, C. Nonbonding Electrons Driven Strong SHG Effect in Hg_2GeSe_4: Experimental and Theoretical Investigations. *Inorg. Chem.* **2018**, *57*, 6795–6798.

(34) Chen, H.; Liu, P. F.; Li, B. X.; Lin, H.; Wu, L. M.; Wu, X. T. Experimental and Theoretical Studies on the NLO Properties of Two Quaternary Non- Centrosymmetric Chalcogenides: $BaAg_2GeS_4$ and $BaAg_2SnS_4$. *Dalt. Trans.* **2018**, *47*, 429–437.

(35) Graf, C.; Assoud, A.; Mayasree, O.; Kleinke, H. Solid State Polyselenides and Polytellurides: A Large Variety of Se–Se and Te–Te Interactions. *Molecules* **2009**, *14*, 3115–3131.

(36) Wu, H.; Yu, H.; Yang, Z.; Hou, X.; Su, X.; Pan, S.; Poeppelmeier, K. R.; Rondinelli, J. M. Designing a Deep-Ultraviolet Nonlinear Optical Material with a Large Second Harmonic Generation Response. *J. Am. Chem. Soc.* **2013**, *135*, 4215–4218.

(37) He, J.; Zhao, L.-D.; Zheng, J.-C.; Doak, J. W.; Wu, H.; Wang, H.-Q.; Lee, Y.; Wolverton, C.; Kanatzidis, M. G.; Dravid, V. P. Role of Sodium Doping in Lead Chalcogenide Thermoelectrics. *J. Am. Chem. Soc.* **2013**, *135*, 4624–4627.

(38) Guo, S.-P.; Chi, Y.; Guo, G.-C. Recent Achievements on Middle and Far-Infrared Second-Order Nonlinear Optical Materials. *Coord. Chem. Rev.* **2017**, *335*, 44–57.

(39) Chen, M.-C.; Wu, L.-M.; Lin, H.; Zhou, L.-J.; Chen, L. Disconnection Enhances the Second Harmonic Generation Response: Synthesis and Characterization of $Ba_{23}Ga_8Sb_2S_{38}$. *J. Am. Chem. Soc.* **2012**, *134*, 6058–6060.

(40) Huang, Y.-Z.; Zhang, H.; Lin, C. S.; Cheng, W.-D.; Guo, Z.; Chai, G.-L. $PbGa_2GeS_6$: An Infrared Nonlinear Optical Material Synthesized by an Intermediate-Temperature Self-Fluxing Method. *Cryst. Growth Des.* **2018**, *18*, 1162–1167.

(41) Wu, K.; Su, X.; Yang, Z.; Pan, S. An Investigation of New Infrared Nonlinear Optical Material: $BaCdSnSe_4$, and Three New Related Centrosymmetric Compounds: Ba_2SnSe_4, Mg_2GeSe_4, and $Ba_2Ge_2S_6$. *Dalt. Trans.* **2015**, *44*, 19856–19864.

(42) Zhang, H.; Zhang, M.; Pan, S.; Dong, X.; Yang, Z.; Hou, X.; Wang, Z.; Chang, K. B.; Poeppelmeier, K. R. $Pb_{17}O_8Cl_{18}$: A Promising IR Nonlinear Optical Material with Large Laser Damage Threshold Synthesized in an Open System. *J. Am. Chem. Soc.* **2015**, *137*, 8360–8363.

(43) Chung, I.; Song, J. H.; Jang, J. I.; Freeman, A. J.; Kanatzidis, M. G. $Na_2Ge_2Se_5$: A Highly Nonlinear Optical Material. *J. Solid State Chem.* **2012**, *195*, 161–165.

(44) Brant, J. A.; Clark, D. J.; Kim, Y. S.; Jang, J. I.; Weiland, A.; Aitken, J. A. Outstanding Laser Damage Threshold in Li_2MnGeS_4 and Tunable Optical Nonlinearity in Diamond-Like Semiconductors. *Inorg. Chem.* **2015**, *54*, 2809–2819.

(45) Guo, Y.; Zhou, Y.; Lin, X.; Chen, W.; Ye, N. Growth and Characterizations of $BaGa_4S_7$ Crystal. *Opt. Mater. (Amst).* **2014**, *36*, 2007–2011.

(46) Badikov, V.; Badikov, D.; Shevyrdyaeva, G.; Tyazhev, A.; Marchev, G.; Panyutin, V.; Petrov, V.; Kwasniewski, A. Phase-Matching Properties of $BaGa_4S_7$ and $BaGa_4Se_7$: Wide-Bandgap Nonlinear Crystals for the Mid-Infrared. *Phys. Status Solidi* **2011**, *5*, 31–33.

(47) Mei, D.; Zhang, S.; Liang, F.; Zhao, S.; Jiang, J.; Zhong, J.; Lin, Z.; Wu, Y. $LiGaGe_2S_6$: A Chalcogenide with Good Infrared Nonlinear Optical Performance and Low Melting Point. *Inorg. Chem.* **2017**, *51*, 1035–1040.

(48) Lai, W. H.; Haynes, A. S.; Frazer, L.; Chang, Y. M.; Liu, T. K.; Lin, J. F.; Liang, I. C.; Sheu, H. S.; Ketterson, J. B.; Kanatzidis, M. G.; et al. Second Harmonic Generation Response Optimized at Various Optical Wavelength Ranges through a Series of Cubic Chalcogenides $Ba_6Ag_{2.67+4\delta}Sn_{4.33-\delta}S_{16-x}Se_x$. *Chem. Mater.* **2015**, *27*, 1316–1326.

(49) Liao, J. H.; Marking, G. M.; Hsu, K. F.; Matsushita, Y.; Ewbank, M. D.; Borwick, R.; Cunningham, P.; Rosker, M. J.; Kanatzidis, M. G. α- and β-$A_2Hg_3M_2S_8$ (A = K, Rb; M = Ge, Sn): Polar Quaternary Chalcogenides with Strong Nonlinear Optical Response. *J. Am. Chem. Soc.* **2003**, *125*, 9484–9493.

(50) Luo, Z.; Lin, C.; Cheng, W.; Zhang, H.; Zhang, W.; He, Z. Syntheses, Characterization, and Optical Properties of Ternary Ba–Sn–S System Compounds: Acentric $Ba_6Sn_5S_{15}$, Centric $BaSn_2S_5$, and Centric $Ba_6Sn_7S_{20}$. *Inorg. Chem.* **2013**, *52*, 273–279.

(51) Feng, K.; Jiang, X.; Kang, L.; Yin, W.; Hao, W.; Lin, Z.; Yao, J.; Wu, Y.; Chen, C. $Ba_6Sn_6Se_{13}$: A New Mixed Valence Selenostannate with NLO Property. *Dalt. Trans.* **2013**, *42*, 13635–13641.

(52) Luo, Z.-Z.; Lin, C.-S.; Cui, H.-H.; Zhang, W.-L.; Zhang, H.; Chen, H.; Zhang-Zhen, H.; Cheng, W.-D. $PbGa_2MSe_6$ (M = Si, Ge): Two Exceptional Infrared Nonlinear Optical Crystals. *Chem. Mater.* **2015**, *27*, 914–922.

(53) Pocha, R.; Tampier, M.; Hoffmann, R.; Mosel, B. D.; Pöttgen, R.; Johrendt, D. Crystal Structures and Properties of the Thiostannates Eu_2SnS_4 and Sr_2SnS_4 and the Selenogermanate γ-Sr_2GeSe_4. *Zeitschrift für Anorg. und Allg. Chemie* **2003**, *629*, 1379–1384.

(54) Denev, S. A.; Lummen, T. T. A.; Barnes, E.; Kumar, A.; Gopalan, V. Probing Ferroelectrics Using Optical Second Harmonic Generation. *J. Am. Ceram. Soc.* **2011**, *94*, 2699–2727.

(55) Assoud, A.; Soheilnia, N.; Kleinke, H. From Yellow to Black: New Semiconducting Ba Chalcogeno-Germanates. *Zeitschrift fur Naturforsch.* **2004**, *59*, 975–979.

(56) Kanatzidis, M. G. Discovery-Synthesis, Design, and Prediction of Chalcogenide Phases. *Inorg. Chem.* **2017**, *56*,

3158–3173.

(57) Johrendt, D.; Tampier, M. Strontium Selenogermanate(III) and Barium Selenogermanate(II,IV): Synthesis, Crystal Structures, and Chemical Bonding. *Chem. a Eur. J.* **2000**, *6*, 994–998.

(58) Yin, W.; Iyer, A. K.; Li, C.; Yao, J.; Mar, A. When One Becomes Two: $Ba_{12}In_4Se_{20}$, Not Quite Isostructural to $Ba_{12}In_4S_{19}$. *J. Solid State Chem.* **2017**, *253*, 29–34.

(59) Assoud, A.; Kleinke, H. *Internal Communication*; 2019.

(60) Assoud, A.; Kleinke, H. A New Polyselenide with a Novel Se_7^{8-} Unit: The Structure of $Sr_{19-x}Pb_xGe_{11}Se_{44}$ with x = 5.0 and 6.4. *Eur. J. Inorg. Chem.* **2017**, *2017*, 5515–5520.

(61) Vu, T. V.; Lavrentyev, A. A.; Gabrelian, B. V.; Ananchenko, L. N.; Parasyuk, O. V.; Karaim, O.; Khyzhun, O. Y. Electronic Band-Structure and Optical Constants of Pb_2GeS_4: *Ab Initio* Calculations and X-Ray Spectroscopy Experiments. *J. Mater. Sci.* **2018**, *29*, 16088–16100.

(62) Feltz, A.; Ludwig, W.; Senf, L.; Simon, C. Glass Formation and Properties of Chalcogenide Systems (XXII). *Krist. und Tech.* **1980**, *15*, 895–901.

(63) Poduska, K. M.; Cario, L.; DiSalvo, F. J.; Min, K.; Halasyamani, P. S. Structural Studies of a Cubic, High-Temperature (α) Polymorph of Pb_2GeS_4 and the Isostructural $Pb_{2-x}Sn_xGeS_{4-y}Se_y$ Solid Solution. *J. Alloys Compd.* **2002**, *335*, 105–110.

(64) Jafarzadeh, P.; Menezes, L. T.; Cui, M.; Assoud, A.; Zhang, W.; Halasyamani, P. S.; Kleinke, H. $BaCuSiTe_3$: A Noncentrosymmetric Semiconductor with $CuTe_4$ Tetrahedra and Ethane-like Si_2Te_6 Units. *Inorg. Chem.* **2019**, 58, 11656-11663.

(65) Tampier, M. Chalcogenogermanate Der Übergangselemente Mit Unedlen Metallen, University of Düsseldorf, 2002.

(66) Akhtar, D.; Goel, T. C.; Vankar, V. D.; Chopra, K. L. Formation of Metastable Solid Solutions in the Pb-Ge System. *J. Mater. Sci.* **1980**, *15*, 2720–2728.

(67) Lefèvre, R.; Berthebaud, D.; Perez, O.; Pelloquin, D.; Hébert, S.; Gascoin, F. Polar Transition-Metal Chalcogenide: Structure and Properties of the New Pseudo-Hollandite $Ba_{0.5}Cr_5Se_8$. *Chem. Mater.* **2015**, *27*, 7110–7118.

(68) SHELX. http://shelx.uni-ac.gwdg.de/ (accessed Sep 20, 2019).

(69) Iyer, R. G.; Aitken, J. A.; Kanatzidis, M. G. Noncentrosymmetric Cubic Thio- and Selenogermanates: $A_{0.5}M_{1.75}GeQ_4$ (A=Ag, Cu, Na; M=Pb, Eu; Q=S, Se). *Solid State Sci.* **2004**, *6*, 451–459.

(70) Choudhury, A.; Polyakova, L. A.; Strobel, S.; Dorhout, P. K. Two Non-Centrosymmetric Cubic Seleno-Germanates Related to CsCl-Type Structure: Synthesis, Structure, Magnetic and Optical Properties. *J. Solid State Chem.* **2007**, *180*, 1381–1389.

(71) Gulay, L. D.; Huch, M. R.; Wołcyrz, M.; Olekseyuk, I. D. Crystal Structure of New Selenosilicates $Pb_{1.75}M_{0.5}SiSe_4$ (M = Cu and Ag). *J. Alloys Compd.* **2005**, *402*, 115–117.

(72) Reshak, A. H.; Kogut, Y. M.; Fedorchuk, A. O.; Zamuruyeva, O. V.; Myronchuk, G. L.; Parasyuk, O. V.; Kamarudin, H.; Auluck, S.; Plucinski, K. J.; Bila, J. Electronic and Optical Features of the Mixed Crystals $Ag_{0.5}Pb_{1.75}Ge(S_{1-x}Se_x)_4$. *J. Mater. Chem. C* **2013**, *1*, 4667–4675.

(73) Duan, R.-H.; Liu, P.-F.; Lin, H.; Zheng, Y. J.; Yu, J.-S.; Wu, X.-T.; Huang-Fu, S.-X.; Chen, L. $Ba_6Li_2CdSn_4S_{16}$: Lithium Substitution Simultaneously Enhances Band Gap and SHG Intensity. *J. Mater. Chem. C* **2017**, *5*, 7067–7074.

(74) Cui, Y.; Mayasree, O.; Assoud, A.; Kleinke, H. Different Clusters within the $Ba_4M_{4-x}A_2Te_9$ (M = Cu, Ag, Au; A = Si, Ge) Series: Crystal Structures and Transport Properties. *J. Alloys Compd.* **2010**, *493*, 70–76.

(75)   Cheng, X.; Whangbo, M.-H.; Guo, G.-C.; Hong, M.; Deng, S. The Large Second-Harmonic Generation of LiCs$_2$PO$_4$ Is Caused by the Metal-Cation-Centered Groups. *Angew. Chemie Int. Ed.* **2018**, *57*, 3933–3937.

(76)   Assoud, A.; Soheilnia, N.; Kleinke, H. Band Gap Tuning in New Strontium Seleno-Stannates. *Chem. Mater.* **2004**, *16*, 2215–2221.

(77)   Khan, I.; Ahmad, I.; Aliabad, H. A. A. R.; Maqbool, M. DFT-MBJ Studies of the Band Structures of the II-VI Semiconductors. *Mater. Today Proc.* **2015**, *2*, 5122–5127.